Electrochemical Deposition of Magnetics Based Sensors

A Thesis
SUBMITTED TO THE FACULTY OF
UNIVERSITY OF MINNESOTA
BY

Matthew Hein

IN PARTIAL FULFILLMENT OF THE REQUIREMENTS
FOR THE DEGREE OF
DOCTOR OF PHILOSOPHY

Professor Bethanie J. Hills Stadler

December 2019

ACKNOWLEDGMENTS

Beyond my cute wife and family, a number of people have played a role in helping me along over the years in my pursuit of advancing my career and knowledge. I would primarily like to thank Prof. Beth Stadler for allowing me to be part of her group and advising during my time as a full-time student, and as a working engineer trying to finish my degree on the side. Dan Foster, David Wulfman, Peter Kuhn and Michael Felling also deserve a huge thanks for their part helping me out academically and professionally. I may not have gotten into magnetics without the help of Dr. Mark Tundra, and would like to thank him for allowing me to get the experience I did at Diagnostic Biosesnors LLC. Similarly, I would like to thank Prof. Shai Ashkenazi for allowing to work as part of his group during my undergraduate degree which helped me decide to go to grad school.

ABSTRACT

Within the context of this thesis, advancements in sensor technology are driven in three separate applications. In each application electrochemistry is used as one of the primary fabrication steps, and magnetic phenomena are sensed in order to convey information about the different systems.

The medical device industry is an area where various sensors are seeing increased use. Electromagnetic catheter tracking is an application that depends on high-quality magnetic sensors. The size of the sensor is a significant design constraint in catheters. Investigation of a microfabricated inductive sensor is pursued in chapter 4 of this thesis. High shape anisotropy inductive structures utilizing etched aluminum oxide as electroplating templates are investigated through first-order modeling and fabrication process development. Results show that the AAO is capable of producing high aspect ratio inductive structures though further development would be needed to achieve the consistency in etching required for large scale device fabrication.

Biomimetic devices are another area of scientific interest where magnetics can play a role. Electroplated magnetic nanowires can act like large arrays of cilia. In chapter 5, biomimetic nanowire arrays are fabricated into microfluidic channels, and their movement sensed via a magnetic sensor. The nanowires provide a magnetic field that bends as fluid flows through the channel which enables a simple flow measurement through microfluidic channels. Similarly, a low frequency (>10Hz) vibration sensor is demonstrated utilizing a nanowire array above a magnetic sensor. Vibration of the sensor imparts momentum on the nanowires, which bend and leads to a time-varying field.

In chapter 6, electrodeposition of Galfenol on a cylindrical surface is demonstrated for the first time. Galfenol has a large magnetostriction constant up to ~400 ppm. Utilizing a rotating cylinder electrode, the parameters to deposit $Fe_{1-x}Ga_x$ films in the x = 15 to 35 range were found. The film's magnetostriction was then demonstrated as part of a torque sensor where magnetic anisotropy was controlled through texturing of the cylinder surface. The effect of magnetic shape anisotropy can be seen to play a significant role in the sensor's

output by increasing the sensitivity of the sensor nearly 6x that of the non-textured film.

TABLE OF CONTENT

LIST OF FIGURES

LIST OF TABLES

1. INTRO

Electrochemistry and magnetics may appear to be two completely different subjects, though in this thesis, it will be seen how knowledge of both can lead to new and novel devices. The research in this thesis covers three main projects all of which utilize a combination of electrochemistry, magnetic materials, and magnetic sensing technology.

The first project involves the development of magnetic sensors for medical applications. In this research, an overview magnetic sensors used in medical devices is first given, followed by an in-depth look at sensors used in catheter applications. Research into the specifications of a catheter-based sensor is discussed, followed by research into two different magnetic sensor designs that utilize electrochemistry in their fabrication.

The second project involves the electrochemical fabrication of magnetic nanowires for use as a flow sensor and a vibration sensor. The concept behind the project is that the magnetic nanowire can act like biomimetic hairs that bend in a fluid flow or sway with low-frequency vibration. For both projects, off the shelf giant magnetostrictive sensors are customized to enable a unique sensor configuration.

The final project involves the first known work where Galfenol, a magnetostrictive material, is deposited onto a cylindrical surface for a torque sensor. The development of a custom fixture used for deposition and the associated electrodeposition parameters, which lead to the optimal film composition is discussed. Texturing of the substrate to induce magnetic anisotropy is investigated, and its effect on a prototype torque sensor is shown.

Throughout the research, electrochemistry and magnetics are fundamental. As such, some background on both topics is given to help set the stage for the research that follows. It is hoped that the background info will help the reader better understand the research that follows and explain some fundamentals of electrochemistry, magnetism, and sensors that someone not familiar with a given area may find useful.

2. ELECTROCHEMISTRY AND MAGNETICS BACKGROUND

2.1. Electrochemistry Background

2.1.1. Electrochemistry Introduction

To put it simply, electrochemistry is the study of how electricity can be used to drive chemical reactions that may otherwise not occur or how chemical reactions can drive electrical charges. It is interesting to study electrochemistry as an electrical engineer given how different it is to the standard EE curriculum, yet many principles from electrical engineering come into play. EE principles such as how a potentiostat works, how the electrolyte can be thought of as an electrical circuit with capacitors and resistor, or just the fact that electrochemistry has been used extensively in the manufacture of circuit boards and other component makes electrochemistry very interesting from an EE perspective. While the field of electrochemistry can be broad, this thesis will focus primarily on electrodeposition and touch on anodization since these are the methods used in the research to be presented.

Without realizing it, most people in the world utilize electrochemistry daily, if not a constant basis. One of the most significant applications of electrochemistry is in energy storage, which basically means the batteries we use to power an ever-increasing number of items. Even if you happened to be plugged into a wall, the circuit boards in your phones and computers might have been electroplated, or parts of your hard drive and other components likely have a plating process somewhere in its production. Similarly, the dull finish on many laptops or other electronics may be an anodized layer of titanium or aluminum. Even the car or bus you may use from time to time certainly have a love-hate relationship with electrochemistry. The reaction that causes rust on a car if fundamentally electrochemical. Luckily though, car manufacturers have found that they can electrochemically plate a layer known as the E-coat directly to the metal, which helps them resist corrosion for years. Under the hood, you will also find that the battery is an electrochemical cell that generated the energy needed to start the car while the car's charging system reverses that process as you drive so that you can have power for your next start.

As noted above, there are a number of applications of electrochemistry and several

reasons to choose it for a manufacturing process. For parts with a complex shape, or that are very large, it can be hard to coat them using spray methods since there are hard to reach areas and overspray may cause excessive waste or environmental issues. Electrodeposition can often occur by just dipping the part in a bath for a given period of time, along with an applied potential. The electrodeposit will build-up everywhere there is a conductive surface. There are some harsh chemicals that may get used in these processes as well, which can have an environmental impact, though since they are kept in a solution, it can be easier to control than the plume created during spraying processes. On the other end of the scale for microdevices, electrodeposition is very useful as well. With microdevices, the manufacturer typically involves some sort of thin film deposition process where thin layers are added and then etched into shapes. The problem with some of these processes is that for thicker layers they can be quite slow. For example, if 10μm of copper was to be deposited using a sputtering process it may take hours to complete due to the slow rates of deposition in addition to the need for high vacuum conditions to be established first. Using a simple Copper sulfate bath this could happen in ten minutes. This is very useful for high aspect ratio structures such as through-silicon vias (TSV's), nanowire fabrication, and redistribution layers on integrated circuits. Of course, there is a major catch to using the electroplating; a conductive surface is needed to start the deposition. At times this may mean a vacuum process needs to be used to get the base layer from which the deposit can grow. Other non-vacuum processes have been developed to get this seed layer, such as electroless deposition, though that will not be covered here. One additional requirement that electrodeposition is a wet process. This can add complexity to the process in some cases though as the technology has progresses this concern is typically addressable. Several other pros and cons exist depending on the application which is why having a deeper knowledge of the basics and processes in electrochemistry could be valuable to any number of research or industrial professionals.

2.1.2. Fundamentals

For most electrochemical processes, the experimental setup can be generalized to look like that of Figure 2-1. The combination of the container and the electrodes is typically called the "cell" or "electrochemical cell." The cell shown in Figure 2-1 consists of a

container to hold the electrolyte, electrolyte which is typically a metal ion salt bath, an anode, a cathode, a reference electrode, and then an energy source, often a potentiostat. In the pictured cell, electrodeposition of Cu from a Cu rod is diagramed. A potentiostat applies voltage between the positive anode and the negative cathode. The electrolyte is a Copper Sulphate (Cu_2SO_4) solution, an ionic compound. In solution, the Cu^{2+} and the SO_4^{2-} disassociate and can act as charge carriers that complete the electrical circuit. From this basic cell that makes up an electrochemistry experiment and from this example several properties of electrodeposition can be discussed.

The first and possibly most basic starting point in electrochemistry is the half-cell reaction. The half-cell reaction is what takes place on one of the two electrodes in solution. This is the fundamental way that reactions are analyzed in electrochemistry. For the Cu cell, there are two reactions, the electrodeposition on the cathode (-) and electron transfer/dissolution at the anode (+). The equation of each half-reaction is given in equation Eqn. 2-1 and 2-2.

$$Cu_{2+} + 2e \rightarrow Cu(s) \quad (2\text{-}1)$$

$$Cu(s) \rightarrow Cu_{2+} + 2e \quad (2\text{-}2)$$

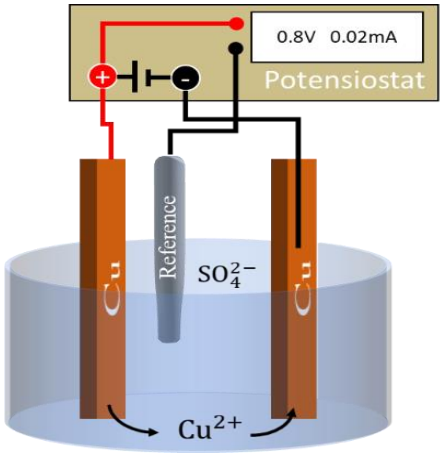

Figure 2-1. Basic electrochemical cell with Cu deposition from a sacrificial Cu Anode in a sulfuric acid solution

To understand electrochemistry, it is useful to first consider the half-cell reactions of the cathode and anode. On the cathode, there is the half-cell reaction shown in Eqn. 2-1 and for the anode, there is Eqn. 2-2. By using a table of standard reduction potentials, it can be found that in standard state conditions the potential of each half-reaction is 0.34V

[1]. Using Eqn. 2-3, the potential for the cell, E_{cell}, can be found to be 0V. It is worth noting that in Eqn. 2-3, the plus sign is sometimes shown as a minus sign. The thing to remember about this is that when using standard reduction potentials, the anode reaction is oxidation, the negative of the reduction potential.

$$E_{cell} = E_{red} + E_{ox} \quad (2\text{-}3)$$

$$\Delta G = -nFE_{cell} \quad (2\text{-}4)$$

From E_{cell}, it can be determined if the reaction will be spontaneous or require an external energy source. Using the Gibbs free energy, Eqn. 2-4, if ΔG is negative, the reaction is spontaneous. Looking at the equation, it becomes evident that the sign of ΔG is directly related to E_{cell}. Thus, by looking at E_{cell} if it is positive the reaction is spontaneous. For the cell of figure 2-1, E_{cell} is 0V, so it is just sitting at equilibrium, and no reaction is expected. If the Cu anode was switched to Zn, E_{cell} now becomes 1.10V, and without applying any voltage, the Zn electrode would start to erode while Cu would deposit on the Cu electrode. Finally, if a Pt anode were used, E_{cell} = -0.85V and a potential greater than 0.85V would need to be applied to drive deposition. This voltage is called the overpotential and can be controlled to drive a given deposition rate.

On the anode side, the opposite process is taking place, Eqn. 2-2. Cu from the anode is getting oxidized and released into the solution, often called a sacrificial electrode. This process is useful for controlling the solution concentration as equal amounts of Cu are released into solution as are deposited on the cathode. Often this process of consuming the anode is used on purpose to etch the surface for texturing in a process called electroforming or to smooth the surface of metals in a process called electropolishing.

Anodization is another process that can occur at the anode. In some sense, this process is more like electrodeposition than electroforming or polishing in that you are creating a film on the electrode being anodized. Unlike electrodeposition, this film grows into the anode as opposed to on the surface. The anodization process changes the chemical structure of the material being anodized. Aluminum (Al) is a common material to anodize, and the basic reaction is given in Eqn. 2-5. The Al combines with Oxygen (O) to create Al_2O_3, and if this reaction were to be carried out for long enough, the complete anode

would oxidize until no metal is left. This process will be discussed more in chapter 7 as part of the fabrication process for a nanowire flow sensor.

$$2Al + 3H2O \rightarrow Al2O3 + 6H+ + 6e \quad (2\text{-}5)$$

2.1.3. Fluid dynamics in electrochemistry

For electrochemical experiments, fluid dynamics can be just as important as the electrodynamics; both are intimately tied together in electrochemistry. From the half-cell reaction of Eqn. 2-1, for deposition to occur, Cu^{2+} ions must be present at the cathode surface. There are two primary ways in which the ions are transported through a solution to an electrode surface, diffusion, and convection. From the dynamics of diffusion and convection several figures of merit such as diffusion layer thickness (δ), mass transport constant (k_d), the Peclet number (Pe), and Reynolds number (Re) are used to describe the systems.

One indirect measurement of ion transport is the measurement of current, I. In an electrochemical system, the current through the circuit is directly related to the reactions occurring at the electrode surface. If an electrolytic cell can be set up such that the ions react as soon as they arrive at the electrode, the reaction is said to be diffusion-limited. Often this condition can be achieved by using a dilute solution. For instance, if a 0.1M solution of copper sulfate is used for deposition, the half-cell reaction of Eqn. 2-1 applies. When the copper deposits, it requires two electrons. If one mole of Cu_{2+} atoms were depositing each second, 2A of current would be flowing, as shown by Eqn. 2-6, where I is the current, n is the number of electrons per reaction, F faradays constant and k a reaction rate in moles/time. This assumes that all reaction is due to the half-reaction of Eqn. 2-1. If a side reaction occurred, such as the evolution of H_2 from H_2O, which has a standard reduction potential of -0.83V, then k and I would be a combination of the various side reaction. With careful experimental consideration, the current can be used to help understand fluid dynamics.

$$I = nFk \quad (2\text{-}6)$$

In the most basic cells, the primary transport mechanism is diffusion. The equations describing this type of transport comes from solving Fick's first and second laws (Eqn. 2-

7, 2-8) with the addition of $nFAD$ where A is area, and D is the diffusivity constant to put it in electrical terms, Eqn. 2-9. Using the first boundary condition, the concentration, c, at the surface is equal to bulk initially. Once the deposition starts, the surface concentration is zero since ions arriving at the surface are immediately deposited (condition for diffusion-limited deposition). In the bulk, the concentration remains constant for all time. Solving this leads to the well-known Cottrell equation for diffusion limited current, Eqn. 2-10.

$$J = -D\frac{\partial c}{\partial x} \tag{2-7}$$

$$\frac{\partial c}{\partial t} = -D\frac{\partial^2 c}{\partial x^2} \tag{2-8}$$

$$I = -nFAD\frac{\partial c}{\partial x}\ ; reduction \tag{2-9}$$

$$I(t) = -\frac{nFAD^{\frac{1}{2}}c_{\infty}}{(\pi t)^{\frac{1}{2}}} \tag{2-10}$$

From the Cottrell equation, it can be seen that the current decrease inversely proportional to $t^{1/2,}$ which leads to the important concept of the diffusion layer. The Cottrell equation and the associated diffusion layer shapes can be seen graphically in Figure 2-2.

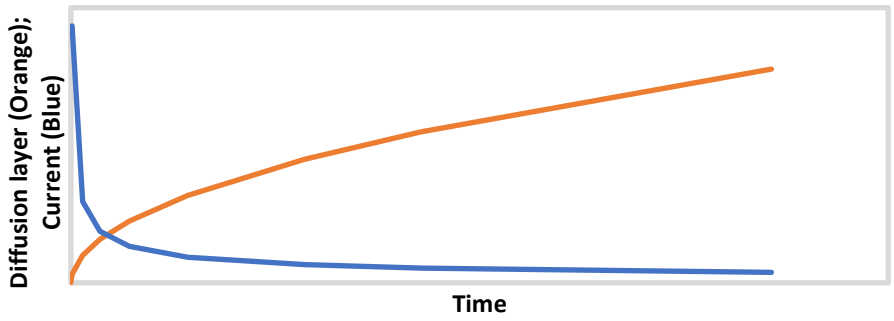

Figure 2-2. Diffusion layer thickness and current of diffusion limited reaction. Based on Cotrell equations Eqns. 2-10 & 2-11.

The diffusion layer thickness, δ, symbolizes the linear distance from the electrode where the ion concentration is different from bulk within some tolerance, i.e., 90% of bulk. Controlling the thickness of this layer is one way to control deposition rates. In a solution of multiple components, it is also a way to control the deposition rate of various

components in solution. Using the Cottrell equation, δ can be defined as in Eqn. 2-11 for cell without convective transport.

$$\delta = (\pi D t)^{\frac{1}{2}} \tag{2-11}$$

The mass transport coefficient, k_m, is a constant that can be used to compare transport under different conditions. For cell without convection, this can be given by Eqn. 2-12. The $t^{1/2}$ dependence once again appears and makes sense. As will be seen below, once convection is added in the equation changes though is still dependent on diffusivity along with other constants and will often be written in terms that include the boundary layer thickness.

$$k_{m,diff\ limited} = (D/\pi t)^{\frac{1}{2}} \tag{2-12}$$

Pe, Eqn. 2-13 is a comparison of convective transport to diffusive transport. In the equation, νl is the convective contribution where ν is the kinematic viscosity and l a characteristic length of the system. This is of importance when trying to determine whether a convective term is needed in the derivation of the transport characteristics.

$$Pe = \frac{\nu l}{D} \tag{2-13}$$

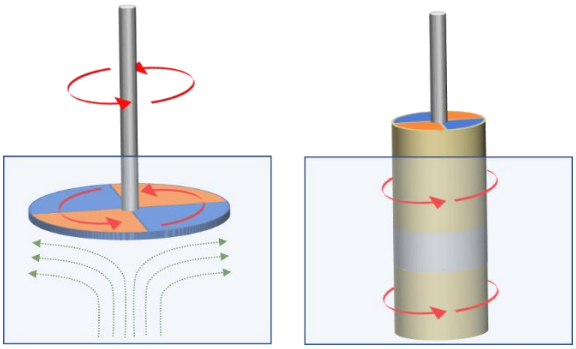

Figure 2-3. a) Illustration of a rotating disk electrode. b) Illustration of rotating cylinder electrode.

With the inclusion of convection, the Reynolds, Re, becomes very important. The Reynolds number is often one of the first numbers one will consider when discussing a fluidic system. For a Re greater than R_{crit}, the convective flow within the system is turbulent, as opposed to laminar. For different geometries, the value at which this transition occurs is different. For electrochemistry with convection, this is very important as it can

have a significant effect on k_m.

In electrochemistry, different cell types are used for different purposes. Rotating electrode cells, such as the rotating disk electrode (RDE) and rotating cylinder electrode(RCE) are examples of two such electrodes. An illustration of the RDE and the RCE are shown in Figure 2-3. As the name suggests, the RDE is essentially a disc-shaped electrode where the bottom surface of the disc is used as an electrode surface while the rest is insulated. The RCE uses a cylindrically shaped electrode where typically only a ring section of the cylinder is used as the electrode surface. Beyond the geometric differences in the two electrodes, what primarily separates them is the fluid dynamics of the two systems. As discussed below, the RDE has laminar flow across its surface, whereas the RCE tends to have a turbulent flow at all but extremely low rotation rate. As such, the RDE sees more use in electrochemical studies where "very controlled" dynamics are required. The RCE, on the other hand, sees the most use when turbulent flows such as in corrosion studies are needed.

Of the two electrodes, the RDE is the most commonly used in research. The primary advantage of the RDE is the ability to precisely control the diffusion layer thickness through control of the rotation rate. The hydrodynamics of the RDE were mathematically described by Levich[2]. At the surface of the electrode, it is assumed that the fluid is stagnant from the perspective of the electrode. As the distance from the electrode surface increases, there is a distance at which the solution velocity has reached 95% of the bulk solution velocity. This distance is referred to as the hydrodynamic boundary layer and is given by Eqn. 2-14. Within the hydrodynamic boundary layer, since fluid velocity approaches zero at the surface, the mechanism of transport to the electrode surface is still diffusion, and the diffusive boundary layer for this is given by Eqn. 2-15. It is worth noting that for the rotating system, the diffusion layer's thickness is not determined by time since the concentration of reactant is essentially the bulk solution due to the mixing generated by the electrode rotation. The lack of a time dependence can thus be seen in the limiting current, Eqn. 2-16, and mass transfer rate, Eqn. 2-17. At the same time, it can be seen that it depends on viscosity, ν, and rotation rate, ω. Given the rotation dependence, this is where the experimentalist typically has the most control and ability to analyze their reactions.

$$\delta_{H,RDE} = 3.6\left(\frac{\nu}{\omega}\right)^{\frac{1}{6}} \quad (2\text{-}14)$$

$$\delta_{diff,RDE} = 1.61 D^{\frac{1}{3}} \nu^{\frac{1}{6}} \omega^{-\frac{1}{2}} \quad (2\text{-}15)$$

$$I_{lim,RDE} = 0.620 nFAC D^{\frac{2}{3}} \nu^{-\frac{1}{6}} \omega^{\frac{1}{2}} \quad (2\text{-}16)$$

$$k_{m,RDE} = 0.620 D^{\frac{2}{3}} \nu^{-\frac{1}{6}} \omega^{\frac{1}{2}} \quad (2\text{-}17)$$

2.1.3.1. Electrochemistry Conclusion

The details given above are only a small snippet of the fascinating and complex study and use of electrochemistry. A more in-depth look at electrodeposition on RCE's is given in chapter 6 and examples of electrodeposition and anodization in chapters 4 and 5. The subject of electrochemistry can be pursued from any number of angles such as fluid dynamics, chemistry, electrodynamics, and so on which makes it an interesting multidisciplinary problem at times. Industrially, there is still somewhat of a "black art" to the use of electrochemistry at times which likely owes to the complexity of the reactions. While there is still so much to be understood about electrochemistry, the advances of the last 100 years cannot be understated, as can be seen through its extensive use.

2.2. Magnetic Basics

2.2.1. Introduction to magnetics

While many people many relegate magnetism to the likes of magic, those with a physics understanding realize that it is magical in a way but still explainable through the laws of physics to some level. While the absolute origins of magnetism may not be fully understood by most, the fundamentals of it are and should be all that's needed for most to make practical use of magnetism.

Probably the simplest way to unfold the mysteries of magnetism is to start from the proverbial ten-thousand-foot view, Figure 2-4. At this distance, the earth can be seen as a giant magnet. The standard convention is to denote the geographical north pole, as the

magnetic south pole, and the geographic south as the magnetic north. While this convention may be a little confusing, it can be understood by considering how a compass works. A compass needle has a north and south pole. Since magnet poles of opposite polarity attract, the north pole of the magnet orients along the geographic north pole, which is the magnetic south pole. A similar convention worth noting is that the north pole of earth or any magnet will get denoted as (+) and the point at which the magnetic field lines start, and the south pole, (-) and the point where magnetic field lines end.

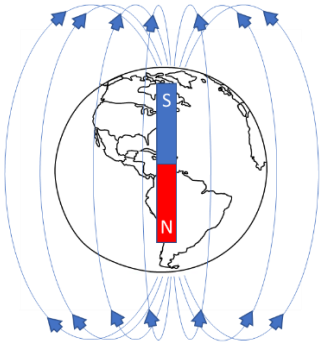

Figure 2-4. Earth's magnetic field.

Two basic types of magnetic field sources exist, the field from a permanent magnet such as earth or a refrigerator magnet and the field due to current flowing through a wire. Depending on the application, the use of one type or the other may be appropriate. In applications where a static field is required, permanent magnets can be a great choice since no external energy source is required. For applications that need to have a field that varies with time or that can be easily adjusted, electromagnets are often the best choice. The interesting fact about both types is that to some extent, they are due to the same thing, electrons moving through space.

2.2.2. Electromagnetism

2.2.2.1. Field of a straight wire

The simplest way to understand electromagnetism is to start from one of the simplest electromagnets to construct, the straight wire. If we assume that the wire has no

permanent magnetism (such as a copper wire) and that it exists in a magnetic field-free space of infinite size, then inside that space, there is no magnetic field. If a current source was attached to the wire and a current forced through the wire, a magnetic field would be generated, which is proportional to the current flowing through the wire. Figure 2-5 demonstrates such a wire. From the illustration, it can be seen the magnetic field propagated circularly from the wire/electron. It should be noted that the direction of the magnetic field is given using the right-hand rule where the thumb point in the direction of the current and the fingers curl in the direction of the magnetic field. The magnitude of this effect is given by Eqn. 3-1. As can be seen from the equation the magnetic field is directly proportional to the current and indirectly proportional to the distance from the wire.

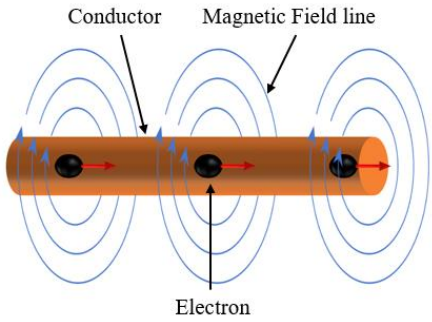

Figure 2-5. Magnetic field of a straight wire.

$$B = \frac{\mu_0 I}{4\pi r}, Where\ \mu_0 = 4\pi \times 10^{-7}\ \left[T \cdot \frac{m}{A}\right], I\ [A], r\ [m] \qquad (2\text{-}18)$$

2.2.2.2. Field of a current loop

The next extension of the straight wire is the current-carrying loop. Physically this is just a wire that has been bent into a loop. If a current loop were broken into small sections, *dx*, and then the magnetic field from each infinitesimally small section summed, the result would be the field of the current-carrying loop. Fortunately, for the on-axis field of this geometry, the integral is quite simple. It is referred to as the Biot-Savart Law and is given in Eqn. 2-19. For Eqn. 2-19 the geometry and variables are defined as in Figure 2-6. While the simplified Biot-Savart law only gives the on-axis field, off-axis solutions can be found[3].

$$B_z = \frac{\mu_0}{4\pi} \frac{2\pi R^2 I}{(z^2 + R^2)^{\frac{3}{2}}} \; ; \; R[m], z\,[m], I\,[A], \qquad (2\text{-}19)$$

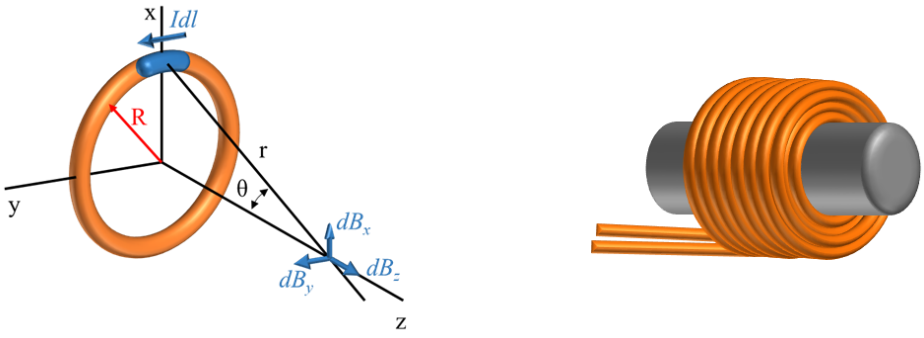

Figure 2-6. Left, Biot-Savart solved for a loop. Right, Multi-layered cored coil.

While the use of a single loop is not unheard of, it is quite common to increase the magnitude of the field by increasing the number of loops (typically called turns). Since the magnetic field of each turn adds vectorially, this can significantly increase the field for a given current. Typically, turns are added both radially and longitudinally (normal to the area enclosed by loop), Figure 2-6, to achieve the magnetic field needed with minimal current. In the center of the coil, it may be empty, or there may be a material, called the core. If there is a core, the material may amplify the value of the field, if and provide a convenient structure to wind the wire on. Eqn. 2-20 gives an approximation of the field from a solenoid coil with an air core[4]. In the equation, B_z is the axial field within a coil in gauss, *n* is the number of turns, *I* is the current, *L* the length of the coil, *D* the diameter and *x* the distance from the center point of the coil along its axis where the field is to be

calculated. More on coils and their use as sensors will be discussed in section 3.5.

$$B_z = \frac{4\pi nI}{10L}\left[\frac{L+2x}{2\sqrt{D^2+(L+2x)^2}} + \frac{L-2x}{2\sqrt{D^2+(L+2x)^2}}\right] \quad (2\text{-}20)$$

The two examples given above are only the are just the basics geometries often used to describe how fields are generated. Depending on the field requirements, numerous different styles of magnets may be used. Table 2-1 lists a couple of different coil types used to generate magnetic fields and their typical use.

Table 2-1. Examples of electromagnetic coils

Coil Type	Brief description	Typical uses
Straight wire	A straight wire, or sheet of material that produced a linearly varying field with distance	In various sensor configurations as a bias source or a stray field source in circuits.
Infinite plane	Similar to a straight wire, though modeled as a sheet current.	Typically, just used as a mathematical model
Rotating Magnet (not electromagnetic)	A permanent magnet fixed such that it can be rotated about its axis.	Used in applications where a time varying field of constant magnitude can be used.
Solenoid coil	The most common coil used. Composed of multiple turns of wire along a given axis. Figure 2-6.	Transformers, Inductors, MRI bore (superconducting), Electromagnetic navigation, countless others.
Helmholtz coil	Two coils spaced one radius apart and wired to generate an additive field in the center	Generate homogeneous field for magnetic testing along coil axis. Typically, only suitable for fields up to a couple hundred Gauss.
Maxwell coil	Similar to Helmholtz coil, though uses three coils at slightly different spacing.	Scientific testing mainly. Allows for a larger more homogenous field than a Helmholtz coil
Anti-Helmholtz	Helmholtz coils wired in reverse to generate gradient field	Gradiometric testing
Bitter coil	Solenoid coil made using copper	Used to generate extremely high

	plates with holes for cooling path during high current testing.	fields in excess of 3T and beyond. Can be used in physics and magnetizing permanent magnets.
Butterfly	Figure 8 shaped coil	Used to generate high gradient magnetic fields such as used in Deep brain stimulation.

2.2.2.3. Voltage induced by a coil

While all the coils discussed so far have been used to generate a field, coils can also be used to sense a magnetic field. The voltage sensing capability of a coil makes it one of the most sensitive magnetic sensors available and will discuss in more detail in chapter 5.

2.2.3. Permanent Magnets

2.2.3.1. Basics Permanent Magnets

When most people think about magnetics, permanent magnets are usually the first thing they think of. These are the magnets that are used in a variety of applications, such as on refrigerators, anything that is magnetically held to a surface, open/close sensors, and more. What differentiates these magnets from other magnet types is that they are always magnetic and can be very strong for their size. This contrasts with electromagnets that require a current source of some sort, or a class of magnetic materials called soft magnets, which require an external field to become strongly magnetized.

Often a permanent magnet will be shown where one side may be labeled as north (or +), and one end labeled south (or -). This is one of the most basic principles of magnets where anytime there is a north pole, there is inevitably a south pole. As an example, if a magnet is broken in half the result would be two magnets, each having a north and a south pole. The magnet could keep getting broken into smaller and smaller parts and will always end up with a north and a south pole.

2.2.3.2. Typical materials

Several different materials exist from which a permanent magnet material can be

made. The typical refrigerator magnet is made of a ferric oxide combined with a polymer binder in sheets that are magnetized and cut to size. For higher-strength magnets, Alnico (composed of AL-Ni-Co) material may be used. For some of the strongest magnets, often called super magnets, these are made of either NdFeB or SmCo, where NdFeB is the more common. With all these magnets types, other impurity's may be added, processing conditions tuned, and even shaped to attain the fields desired. A comprehensive discussion of permanent magnets is beyond the scope here, so the reader is suggested to look at other sources such [4] for more information.

2.2.4. Explanation of fundamental units

In the field of magnetics, units are possibly one of the most confusing things to understand. It is the goal of this section to explain magnetics by going through the units and trying to add clarity. Both CGS and SI units of magnetism are practically used, so an explanation of how they relate will be a key focus. The IEEE magnetics society has a great table of conversion factors between SI and CGS units and is recommended for anyone looking for a reputable source of magnetic conversion factors[5].

Possibly the units most used in magnetics are the Tesla (T), Gauss (G), Amps per meter (A/m), and Oersted (Oe). This is a spot of confusion for many people. Tesla and Gauss are units of magnetic inductions, also called magnetic flux density. Amps per meter and Oersted are units of magnetic field strength. What seems to confuse people is the way the terms are used. Often when reading a datasheet or discussing magnetics, the magnetic field will be discussed in terms of Tesla or Gauss. In practice, to measure a magnetic field, one may buy a magnetometer, sometimes called a Gauss meter, or Tesla meter, not an Oersted meter or amp meter. A simple explanation is that T, G, A/m, and Oe are equivalent (with a conversion factor) when measured in air or vacuum. Since most measurements are taken in air, the mixing of these terms is understandable, though it should be done with caution.

For a more thorough understanding, it helps to take a closer look at the difference between magnetic induction and magnetic field. A good way to look at this is starting with the equations that define magnetic induction. Table 2-2 below shows the equation in both SI and CGS. Looking at the equation in CGS and SI, it can be seen that magnetic induction

is the combined effect of the magnetic field (H) and Magnetization (M). Looking at the equation in CGS, both H and M must have units equivalent to B. Similarly, in SI, H and M must have equivalent units, though both must be multiplied by μ_0 to get to units of B. The difference between B and H in both units is M. Thus, for B to be equivalent to H, M must be zero. As it turns out, the magnetization of air is extremely small and typically can be considered zero. Looking at the fundamental units of H [Oe] and M [G] in CGS shows that they are equivalent (other than 4π for CGS) with CGS base units of $cm^{(-1/2)} \cdot g^{(1/2)} \cdot s^{-1}$. SI is a little simpler in that both H and M have units of A/m; thus, when multiplied by μ_0 with units of $T \cdot m \cdot A^{-1}$, you get to T.

Table 2-2. Magnetic units conversion

	CGS	Conversion	SI	Eqn
Magnetic induction	$B\ [G] = H + 4\pi M$	1 x 10^{-5}	$B\ [T] = \mu_0\ (H + M)$	(2-21)

2.2.5. Magnetic material properties

2.2.5.1. Explanation of VSM

The concept of B, H, M, and other magnetic quantities can be further understood by dissecting how a tool called the Vibrating Sample Magnetometer (VSM) works. In general, the purpose of a VSM is to measure the DC magnetic properties of materials. Figure 2-7 shows an example of a VSM.

The VSM consist of three main components. First is the electromagnet, which is responsible for generating the DC field that is applied to the samples. Second, are the pickup coils which measure the magnetic induction from the sample. Finally, is the vibration motor. The vibration motor is used because the pickup coils can only measure AC magnetic field (see section 3.3). By vibrating the sample up and down within the DC field, each coil sees an AC magnetic field and thus generates a voltage proportional to the magnetic flux through it.

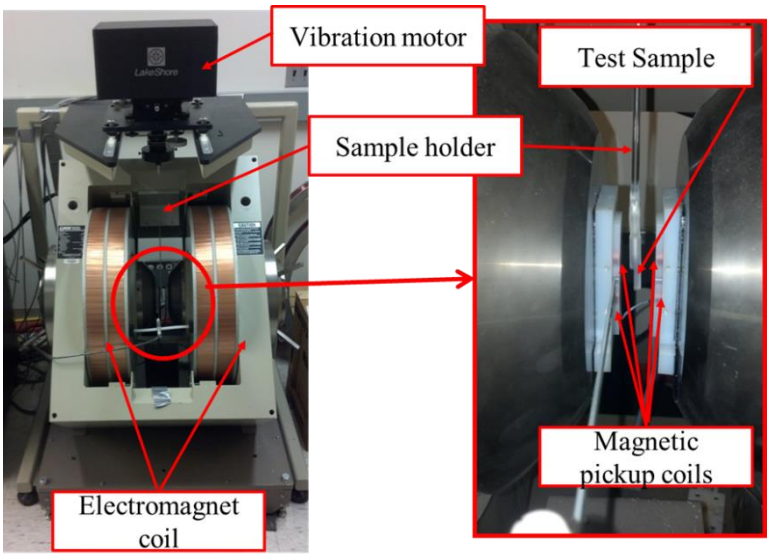

Figure 2-7. Example of vibrating sample magnetometer (VSM).

An example of the typical VSM curve is shown in Figure 2-8. The typical curve will start at either zero magnetic field (H_0) or a field that magnetically saturates the sample (H_s). In reality, all loops start at H_0, though the initial ramp is often ignored. The sample will then be magnetized from its positive saturation point to its negative saturation point and then back to its positive saturation point, forming what is called a B-H loop, or M-H loop(if the applied H-field is subtracted) or a hysteresis loop. Stepping through this loop several magnetic material properties can be explained.

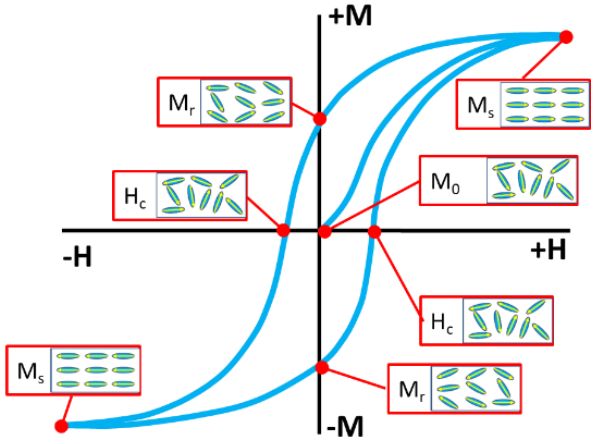

Figure 2-8. Example of a VSM curve.

2.2.5.2. Properties from the VSM curve

The first step in the VSM loop is before the sample enters the field. A magnetic field between the poles is generated to offset earths DC field. This means $M_{gap} \approx 0$ since no magnetic material is in the gap, and thus $B \approx \mu_0 H$ (SI). Since the applied H-field is offsetting Earth's magnetic field B = 0. Because this field is DC and stationary, it induces no voltage in the pickup coils. For this example, it can be assumed that the sample has either never been magnetized or was demagnetized and exist in a zero magnetic field environment. In this case, the magnetic materials magnetic domains are all randomly oriented, resulting in no net magnetization of the sample (M = 0, H = 0,). See M_0 Figure 2-8.

Saturation

The next step in the VSM loop would be the initial rise in magnetic field strength to the saturation point, H_{Sat}. At H_{sat}, it can be seen that all the domains are aligned in the positive direction, and the magnetization of the sample is said to be saturated, M_{sat}. It is at this point that the material cannot be magnetized any further. Looking at the curve, it can be seen it has flattened out since as H increases M does not. If instead of an M-H curve this was a B-H curve, a positive slope would still exist, though the increase would only be due to added H as opposed to any additional M.

Remanence

The next point seen on the loop is the remanence point, B_r or M_r. Remanence is the magnetization left in the sample after having been saturated, and then the H-field brought back to the zero point. In most ferromagnetic materials, there will be a significant difference between the magnetization before and after magnetization. From Figure 2-8, it can be seen that at remanence where H = 0, many of the domains remain aligned in the positive direction. It is this property of ferromagnetic materials that makes permanent magnets possible.

Coercivity

As the field continues beyond the zero point and starts increasing in the negative direction, the next significant point encountered is the coercivity of the material, H_c. At this point, enough field in the direction opposite the original magnetization direction has been applied to bring the magnetization of the sample back to zero. It is worth pointing out here

that B is not zero at this point due to the field applied to the sample; only M is zero. This point can be significant as it defines where the magnetization switches directions. In some cases, this can be a very dramatic change. In the case of hard drive media, it is past this point that the hard drive must magnetize the bits to flip the magnetization and thus write the bit as either a 1 or 0. Similarly, for permanent magnets, the region between H=0 and H_c is called the second quadrant B-H loop and is used as the primary measure of the quality of permanent magnets.

Negative Saturation

The final point as the field continues in the negative direction is the negative saturation point, H_{-Sat}. This is essentially the same as the H_{sat} point, except now the materials moment is pointing in the opposite direction. The value of M should be equal and opposite that of the positive saturation point since all domains are fully saturated in the opposing direction.

After the negative saturation point, the field is again brought back up to positive saturation. The material should come back to the exact same magnetization as before, M_{Sat}. As the field increases from $-H_{Sat}$ to $H_{Sat,}$ the material once again goes through a remanence point and a coercivity point before hitting H_{Sat}. At his point, a full hysteresis loop is complete. Often several loops may be performed to allow averaging of the loops or to apply some "wear" to the magnet to confirm no change in properties.

Hysteresis

With a full loop, completed other measurements can be made. One of the most important measurements at this point is the samples hysteresis, H_{hyst} , or M_{hyst}. This is taken either as the difference in H-field or magnetization between the decreasing and increasing halves of the loop. Depending on the application, it may be desired to make the hysteresis large, such as for a permanent magnet or magnetic memory. In sensor applications, it is often desirable to have this as small as possible.

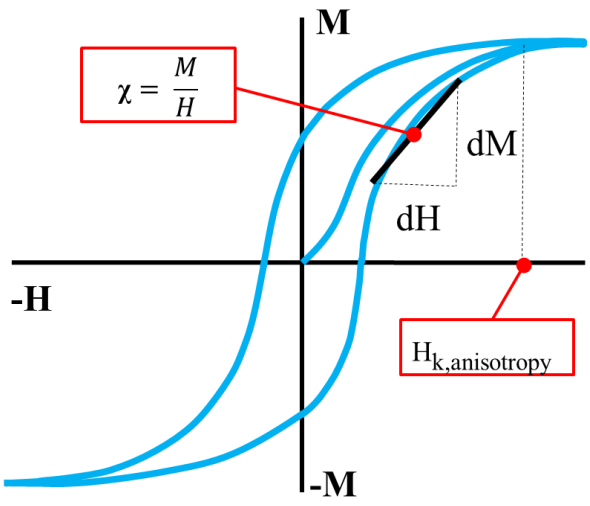

Figure 2-9. M-H loop showing susceptibility.

Permeability / Susceptibility

A second fundamental measurement is the permeability, μ, or susceptibility, χ. χ is shown in

Figure 2-9, and the equation defining both χ and μ are given in Figure 2-9. The susceptibility is simply the change in magnetization with respect to the change in magnetic field. If this curve were a B-H loop a similar measurement, permeability would be the change in magnetic induction with respect to the magnetic field. The measure that gets used typically depends on the type of magnetic work that is being done. From the perspective of this author, it seems that those working with/studying material fundamentals tend to be interested most in susceptibility, whereas for the person designing devices such as sensors, rectifiers, or other transducers, permeability tends to be the quantity of choice.

$$\mu = \frac{\Delta B}{\Delta H}[unitles] \quad \chi = \frac{\Delta M}{\Delta H}\ [unitless] \tag{2-21}$$

2.2.5.3. Ferromagnetism

One general misconception about magnetic materials is that some materials are magnetic, and others are not. In truth, all materials have magnetic properties, though their magnetic properties are non-obvious. What most people think of as magnetic materials are ferromagnetic (FM) materials such as permanent magnets or mu-metal. Four other classes

of magnetic materials exist; paramagnetic, diamagnetic, antiferromagnetic and ferrimagnetic. In fact, all materials exhibit either paramagnetic or diamagnetic characteristics, though this effect can be very small and overshadowed by ferro and ferri-magnetism. Each type of magnetism is a study unto itself at times, and since ferromagnetism is the primary type of magnetism used in this research, the other types will only be briefly mentioned.

A typical way to differentiate the types of magnetism a material has is from its permeability, susceptibility, or whole hysteresis curve. Ferromagnetic materials can have very large permeabilities and nonlinear hysteresis loops. Paramagnetic and diamagnetic materials will tend to be linear though paramagnetic materials will have permeabilities slightly greater than 1, and diamagnetic materials may have a positive permeability, though their susceptibility is negative. Antiferromagnetic materials have a small positive susceptibility similar to paramagnets, but when measuring susceptibility vs. temperature, a transition point is found where the material goes from antiferromagnetic to paramagnetic at the Kneel temperature. Ferrimagnetic materials will have hysteresis and permeability properties similar to an FM material, though the material composition is oxide in nature, and the materials are often referred to as "ferrite." Further details of the magnetization can be described via a hysteresis loop though the details are beyond the scope here.

Ferromagnetic materials are the most widely known and what is typically recognized as a magnetic material. Iron (Fe), Nickle (Ni) and Cobalt (Co) and now Ruthenium[6] are the only elements known to have ferromagnetic properties at room temperature. These elements are often alloyed together with each other or with other "non-magnetic" elements to tune the properties of the material for a given application. One good example of a popular alloy is stainless steel. Stainless steel is used in numerous applications with refrigerators and other kitchen appliances being among the most obvious. There are many variations of stainless steel, but they generally consist of Fe, Cr, Ni, and carbon. Depending on how it is alloyed and manufactured, the material may be magnetic (400-series) or "non-magnetic" (300-series, actually weakly ferromagnetic). Strangely, it is in part the addition of the Ni to the alloy which makes it non-magnetic. Another class of ferromagnetic alloys exists that has no magnetic elements, but when alloyed exhibits ferromagnetic behavior. These are known as Heusler alloys, and some typical examples

are Cu_2MnAl, Cu_2MnSn Ni_2MnAl, and Co_2MnSi.

The origins of ferromagnetism lie in the quantum nature of electron spins and their orbital interactions. Like paramagnetic materials, polarized electrons are part of the magnetizing process. What makes the ferromagnetic materials different is that they can spontaneously magnetize under a no-field condition.

In order to have a magnetic moment, there first must be unpaired electron spins. For example, Helium only has 2 electrons. Since the spin of the first electron is opposite that of the second, the moment of each electron cancels, leading to no net magnetic moment. If, on the other hand, they happened to align in the same direction (impossible due to Pauli exclusion principle) you would have a moment.

Hunds rule for electron pairing can be used to help understand the ferromagnetic materials, Figure 2-10. Using Hund's rule, it can be seen that there is an even number of electrons in the 3d orbitals for Fe, Co, and Ni, though they do not all have paired spins. For the next element in the table, Cu, the 4s orbital gives up an electron to the 3d orbital from the 4s orbital which is energetically favorable and leads to Cu not having a 3d spin to contribute to its magnetism. Similarly, it can be asked why Mn, the element right next to Fe is not ferromagnetic. It can be found that Mn is paramagnetic due to the unpaired electrons, but unlike the ferromagnetic materials, it does not have strong exchange interactions. It is this exchange interaction which promotes long-range order and spontaneous magnetization in ferromagnetic materials.

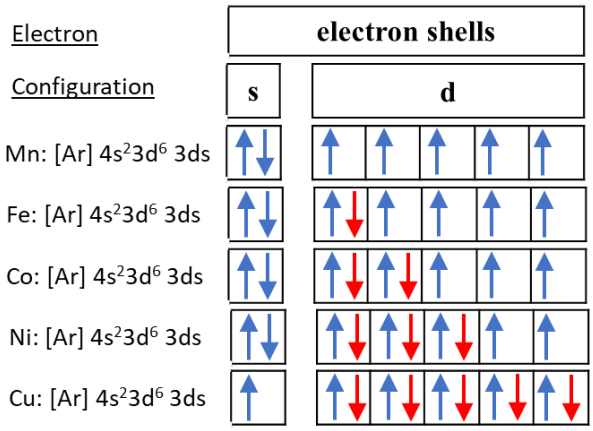

Figure 2-10. Hund's rule, showing select transition metals including the ferromagnetic Fe, Co, Ni.

2.2.5.4. Anisotropy (magnetocrystaline, shape, stress, exchange)

Anisotropy energy is another very interesting and often overlooked property of magnetic materials. A layperson often does not recognize the many factors that affect a magnetic samples properties. If two magnetic samples of the same mass and composition are measured, it may be found that the measurements are significantly different. Often the reason for this has to do with the anisotropy energy of the magnet. Four main types of anisotropy characterize magnetic materials: magnetocrystaline anisotropy, shape anisotropy, stress anisotropy, and exchange anisotropy. Magnetocrystaline (or crystal) is inherent to the material and is due primarily to spin-orbit and orbit lattice interactions of the electrons in the materials crystal lattice. Shape anisotropy is due to the shape of the magnet, which affects the magnet's demagnetization energy. Stress anisotropy, like magnetocrystaline, is also due to spin-orbit interactions, though stress causes the orbits to reorient changing the properties of the material. Finally, Exchange anisotropy is due to a coupling between ferromagnetic and antiferromagnetic materials in very close proximity, typically thin film layers. While all types of anisotropy play an essential role in magnetism, shape, and stress are used extensively in this research and will be discussed further.

2.2.5.5. Shape Anisotropy

Shape anisotropy is as the name suggests, due to the shape of the sample, which affects something known as the demagnetization (demag) energy of the magnetic sample. Inside a magnet, there is an H-field and a magnetization acting on the sample, which in turn leads to the magnetic induction, B, of the sample. Shown in Figure 2-11 is a magnetized magnet in zero external magnetic field[4]. While most of the field from the magnet follows a path external to the magnet, some of the field follows the near direct path from the north pole to the south pole. This field is known as the demagnetizing field, Eqn 3-6. The demagnetizing field is proportional to and never larger than the magnetization, so the net magnetic induction is still from left to right in Figure 2-11. Combining the demag field with the sample's magnetization then gives the magnetic induction of the sample, Eqn. 3-7.

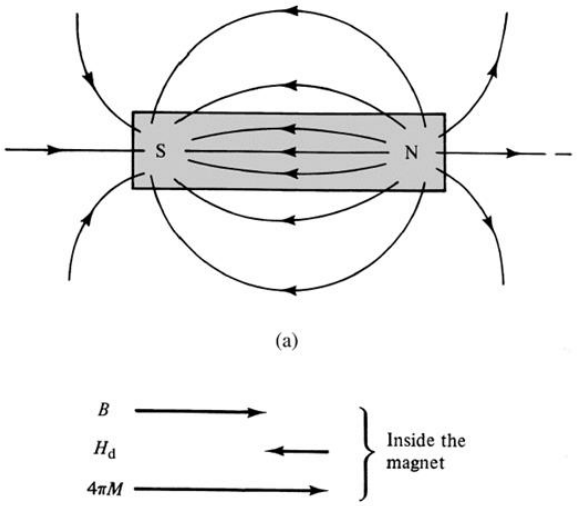

Figure 2-11. The magnetic fields inside a material [reff].

$$H_d = -N_d M \tag{2-22}$$

$$B = H_d + 4\pi M = -N_d M + 4\pi M, \ where\ H_d < 4\pi M\ (c.g.s) \tag{2-23}$$

The demagnetizing factor, N_d, is a geometry dependent number that relates the sample's magnetization to the demagnetization field in the sample, Eqn. 2-22. N_d can be very hard to calculate for arbitrary shapes, though for ellipsoidal shapes, the process is relatively straight forward. Three different ellipsoidal shapes are typically described and shown in Figure 2-12. A particular case of the ellipsoid is where $a = b = c$, which is a sphere. For the sphere, the demagnetization factors along each axis are equal, Eqn. 2-24. The prolate ellipsoid is one of the most used shapes as it can be used to approximate the demagnetization factor for a cylinder. For the prolate ellipsoid, $a = b < c$ and the ratio $m = c/a$ can be used to simplify the demagnetization equations shown below.

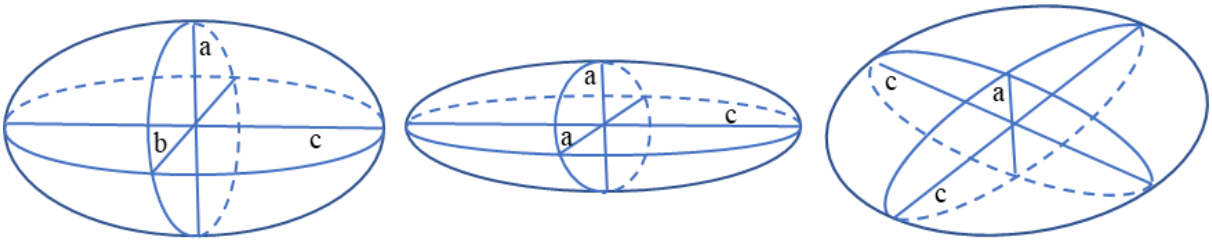

Figure 2-12. Simple shapes used to calculate the demagnetization factor. Left, General ellipsoid. Middle, prolate spheroid. Right, oblate spheroid.

$$N_a = N_b = N_c = \frac{4\pi}{3}(cgs). \tag{2-24}$$

$$N_a + N_b + N_c = 4\pi\ (cgs)\ or\ 1\ (S.I.)$$

$$B = H_d + 4\pi M = -N_d M + 4\pi M,\ where\ H_d < 4\pi M\ (c.g.s) \tag{2-25}$$

For long thin rods as used in much of the research to be presented, $a = b \ll c$ and

$$N_c = \frac{C_3}{m^2}(\ln(2m) - 1), \tag{2-26}$$

$$where\ m = \frac{c}{a}, C_3 = 1\ [SI] or\ 4\pi[cgs]$$

$$N_a = N_b \approx \frac{C_3}{2} \tag{2-27}$$

Using this relation along with Eqn. 2-28 for high permeability ferromagnetic material[7], an estimate of inductor core permeability can be obtained. This value can then be used in the design of inductors, sensors, and other transducers. Figure 2-13 shows this plotted along with the demanganization factor.

$$\mu_c = 1/N_d \tag{2-28}$$

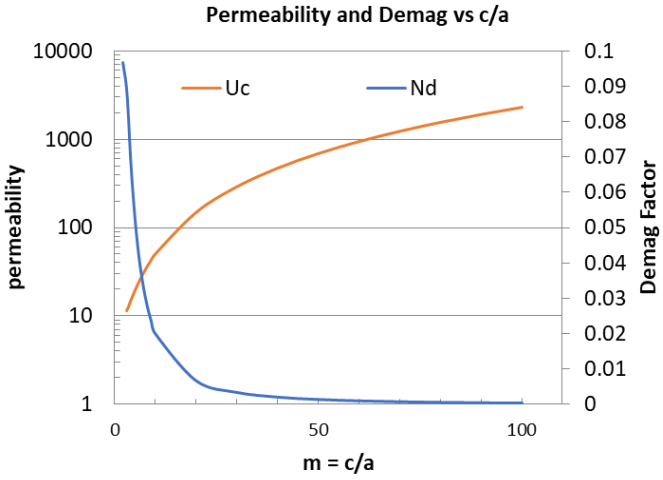

Figure 2-13. Permeability and demag factor plotted.

2.2.5.6. Stress Anisotropy

The basic concept of stress anisotropy is that in a "perfect state" the atoms of a material have some optimum distance from each other where their electron could have their minimum energy. As stress is applied to the material, the attractive and repulsive forces

with the lattice are brought out of their lazy low energy position and now must figure out how to relax again, even if it is not to the same minimum energy state they were in before. Figure 2-14 shows a simplistic cartoon depicting this phenomenon. In the upper left, the electrons are in their lowest energy state with no stress applied. On the right, stress has forced the electrons to start sharing space, and no one even an electron likes that. To cope, the electrons then spread out in different directions where they may not be as comfortable, yet still happier than sharing the space with the other electrons, Figure 2-14 lower-middle. Lastly, it is worth noting that as the electron clouds compress and expand so will the lattice leading to the change in the shape of the overall sample.

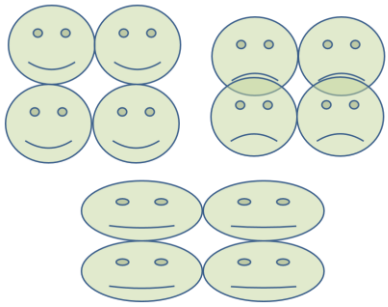

Figure 2-14. Cartoon illustration stress anisotropy.

2.2.5.7. Magnetostriction

The result of stress anisotropy in materials is often referred to as magnetostriction. There are a few different ways that magnetostriction occurs in different materials. A common analogy to magnetostriction is the piezoelectric effect. While a couple of types of magnetostriction effects are known, the Joule effect is the one most like the piezoelectric effect where instead of applying an electric field to induce strain, a magnetic field is applied. The inverse of this is called the Inverse Joule or Villari effect, where straining the sample will cause a change in the sample's magnetic properties (moment, permeability...). The Weidman effect and Matteucci effect are similar to the Joule effect and Inverse joule effect except that a helically applied field causes a twist of the material for the Weidman effect, and the application of torque to the material induces a helical anisotropy for the Matteucci effect.

Numerous applications have been proposed and implemented since its discovery. Possibly the first device to implement magnetostriction was a telephone receiver tested by

Phillips Reis[8]. Since then, applications like oscillators, motors, micropositioners, sonar transducers, and ultrasonic transducers have seen commercial success using the Joule effect [8]. Sensor applications such as the torque sensors (discussed in chapter 6), position sensors [9], and various vibration and structural health sensors have also been proposed and/or implemented [10]. Often sensors use the inverse Joule effect where the mechanical energy and can be harvested into an electrical signal. In a similar sense, energy harvesting is another area where magnetostrictive materials have seen a significant amount of research[11] due to the ability to couple mechanical energy into electrical.

For magnetostriction, typically one of several different materials are used. While all materials experience magnetostriction, only a few show a large enough effect to be usable. Some of the more popular materials include Ni, Fe, cobalt ferrite ($CoFe_2O_4$), Galfenol ($Fe_{1-x}Ga_x$), Alfenol ($Fe_{1-x}Al_x$), and Terfenol ($Tb_xDy_{1-x}Fe_2$). For magnetostrictive materials, the figure of merit most often used is its magnetostrictive strain measured at saturation. The symbol λ_s is often used to represent this saturation magnetostriction and is given in ppm. For materials where the λ_s is greater than 100 ppm, it is often referred to as large magnetostriction, and for materials with λ_s greater than 500 ppm it is referred to as giant magnetostriction. Alfenol, Galfenol, and Co-Ferrites fall into the large magnetostriction category while only Terfenol materials fall into the giant category.

The most commonly used of the magnetostrictive materials is Terfenol-D (sometimes just called Terfenol). This is directly related to it having giant magnetostriction with a single crystal value as high as 2000 ppm [12]. The material was developed in the 1970s by the Naval Ordinance Lab owing to the “nol” in its name. The material is typically made using bulk crystallization methods from which it can be mechanically modified for parts, or can be cut into targets for thin-film sputtering. While Terfenol has the largest λ_s, it suffers from low ductility and is hard to machine, making it tough to work with and fabricate finished goods.

Galfenol is a material that was developed in the 1990s to help overcome some of the issues with Terfenol. Similar to Terfenol, Alfenol and Galfenol were initially developed by the Naval Ordinance Lab. As can be seen in Table 2-2, the Youngs modulus of both Terfenol and Galfenol can be similar, though the tensile strength of Galfenol is almost 10x that of Terfenol. This feature of Galfenol allows it to be used throughout a larger dynamic

strain range with a safety factor that Terfenol would not be capable of. Terfenol and Galfenol are similar in terms of coupling factor, though Terfenol is slightly higher and has about 3x the strain of Galfenol. Not to be outdone, Galfenol has a permeability up to 10x that of Terfenol and a saturation flux density about 1.5x that of Terfenol. Another significant benefit of Galfenol is that it is highly machinable as compared to Terfenol. Additionally, it can be manufactured in several different ways. Various bulk manufacturing techniques can be used, but additionally, electrochemical methods such as that used chapter 6 are possible as well.

Table 2-2. Table of magnetostrictive properties. adapted from [12,13]

Tables of magnetostrictive properties	FeGa	$Tb_{0.3}Dy_{0.7}Fe_{1.92}$
strain	200-250 ppm	800 – 1200 ppm
Youngs modulus	40 – 80 GPA	18-90 GPA
Tensile strength	350 MPA	28-40 MPA
Saturation flux density	1.5-1.6T	1 T
Permeability	75-100	2-10

3. PRACTICAL REVIEW OF MAGNETIC SENSORS

3.1. Intro

Magnetic Sensors can be found all around you, and in all likelihood, more than one or two types may be closer than one might think. Whether it is a cellphone compass, computer hard drive, door close switch, or other, odds that most people are probably hands reach from at least one magnetic sensor. Someone would probably have to be living in a very remote area without a compass to get away from magnetic sensors. As noted, one of the most basic and possibly oldest sensors would be a compass that has its origins back in the 11th century as a navigation device[14]. Compasses still exist today, although many advances have been made, and the ones used in electronics typically rely on either hall or MR technologies. High-end compasses for flight and scientific studies often use fluxgate technology due to its higher resolution.

It can be hard to classify Magnetic sensors as there are many types of sensors and a lot of cross over in their uses depending on how they are designed and implemented. Some sensors, such as inductive based sensors can be classified as passive since they do not need power to operate, though they can also only sense time-varying fields. Active sensors would include sensors such as Hall, MR, fluxgates, vapor magnetometer, and squid sensors since they require power external to the sensing portion of the sensor. Figure 3-1 shows an attempt to classify magnetic sensors down into categories.

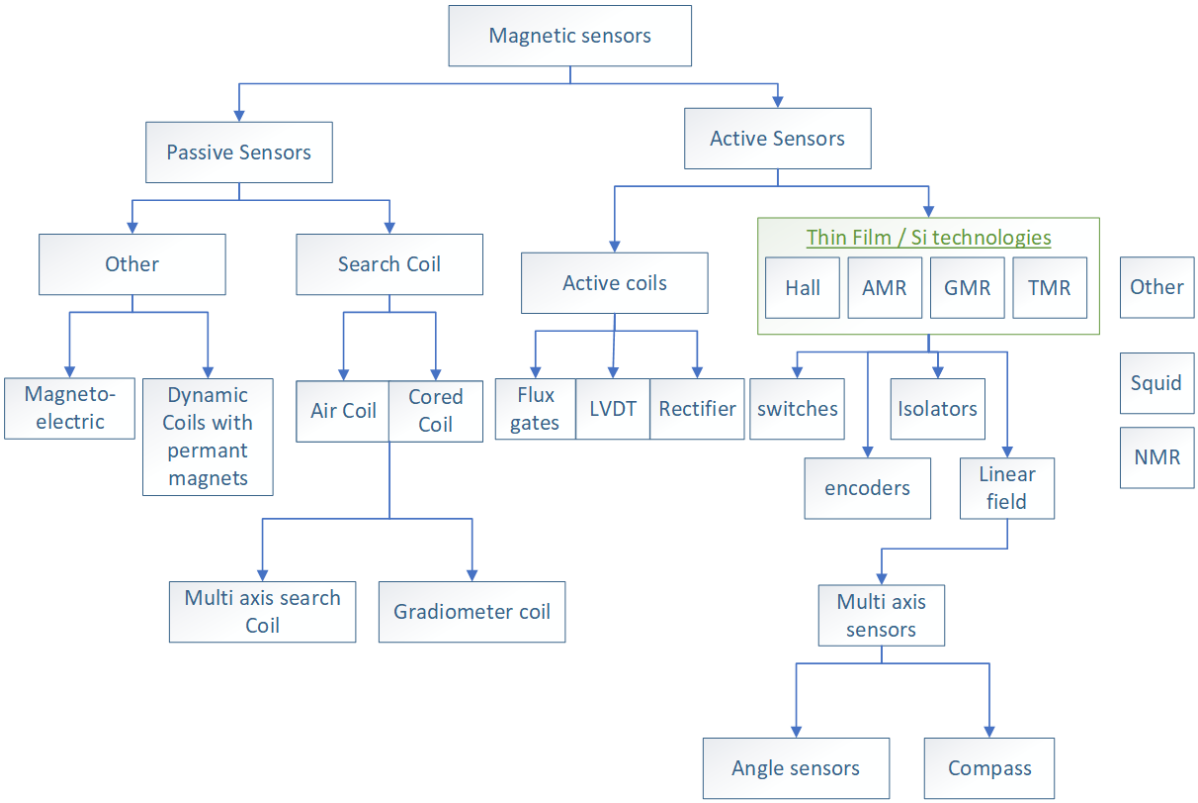

Figure 3-1. Classification of magnetic sensors

Another way to consider magnetic sensors is with respect to their usable range. Figure 3-2 shows various sensor technologies and their associated field ranges. For reference, the field range of earth and other medically relevant signals are shown. By far, the most versatile of sensors is the search coil, though the fields must be time-varying. All other technologies are capable of both time-varying and DC signal measurement.

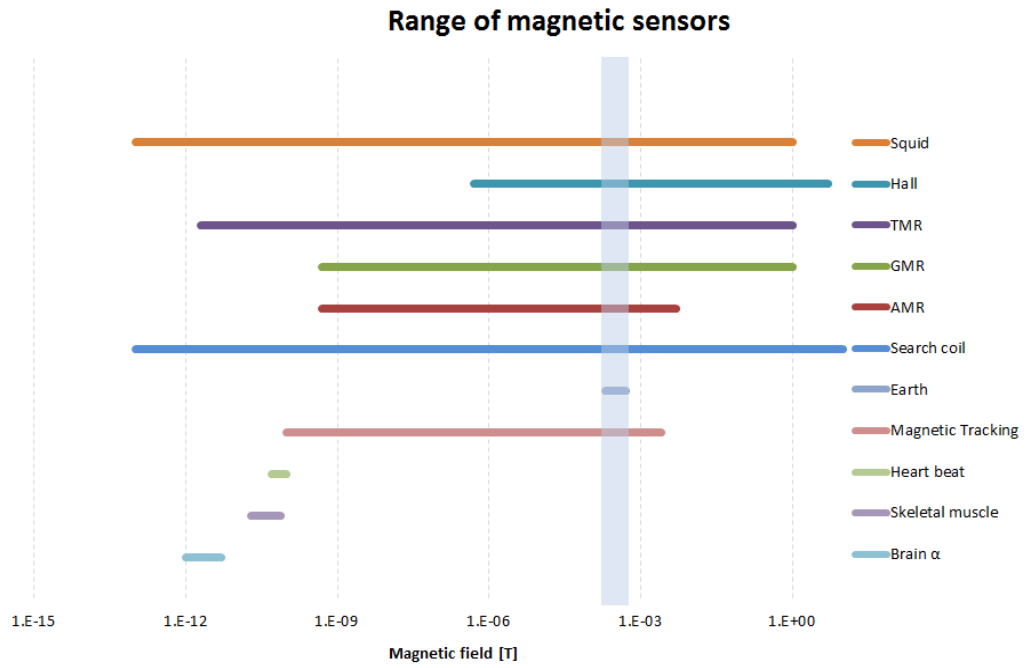

Figure 3-2. Range of various magnetic sensor technologies.

3.1.1. General sensor signal chain

When using sensors, their output usually is not useful until it can be measured. Ultimately, most sensors output a voltage that is proportional to the amplitude of the signal being measured. Analog methods of measuring a sensor's output still exist, though today it would be hard to imagine a system that does not include an analog to digital converter(ADC) somewhere in the measurement system. Figure 3-3 shows A generalized example of the signal chain of most sensors. First, there is the external stimulus which causes a change in the voltage output of the sensor. That signal then travels some distance, ranging from nanometers to meters or more at times, often through a conditioning circuit to reach an amplifier. From the amplifier, the signal may go through one more conditioning circuit whose function is to fit the signal to the input specifications of the ADC. Once the signal becomes digital, any number of operations may be applied to the signal before displaying it to the user. One advantage of modern sensors is that often they take advantage of application-specific integrated chips (ASIC) where much of the signal chain through the ADC may occur directly on-chip. This allows a smaller total package and a potentially less noise in the circuit in addition to other unique features an ASIC designer may implement.

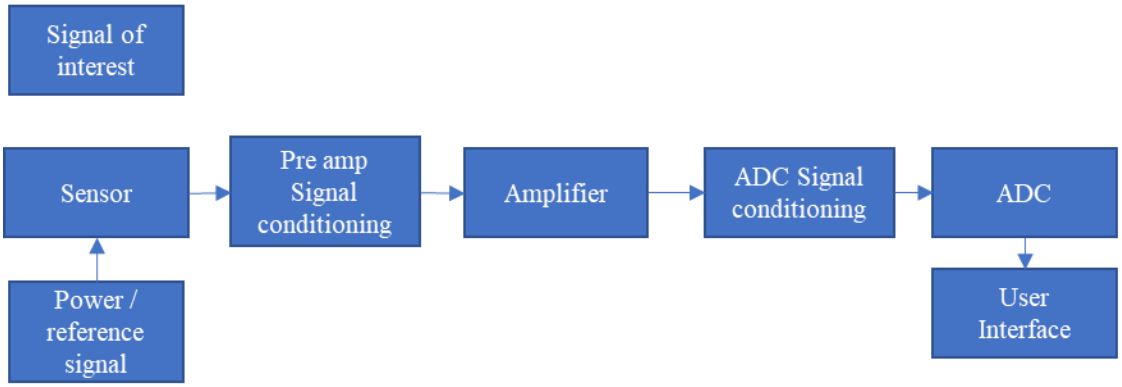

Figure 3-3. Typical signal chain of the sensor.

When designing sensors or designing with sensors, the figure of merit most often touted is the signal to noise ratio (SNR). There are various ways it can be calculated, but in general, it is the ratio of the signal of interest to any noise that may exist in the system of interest. The higher this value, the better, though rarely is there too much signal and very little noise, and so this is typically optimized as much as possible. To maximize the SNR optimization of both signal and noise must be performed.

$$SNR = \frac{Signal}{Noise} = \frac{Sensitivity * Signal\ amplitude}{Noise} \tag{3-1}$$

Optimization of the signal typically involves one of two primary methods, either making source signal larger or increasing the sensitivity of the sensor. Often the source signal cannot be increased, so instead, the position of the sensing element is optimized to make the most of the signal. This may mean physically moving the sensor closer to the signal source, or orientation of the sensor so that the signal is in the direction of the sensor axis of highest sensitivity. If the source signal cannot be made strong enough, the only other option is to increase the sensitivity of the sensor. For the system designer, this often means finding the sensor with the largest sensitivity for their signal range. For the sensor designer, this is at the heart of what they do. Sensor designers often have several strategies for optimizing sensitivity. The methods may include sensor material choices, bridge

circuits, sensor size, integration techniques, flux guiding, and other methods that vary depending on the sensor technology.

Optimizing noise is the second way of increasing SNR but by no means a secondary concern. Noise in both the sensor and its circuit can kill any sensor design. The best sensor design will be useless in a circuit with high noise, and a low noise circuit is useless or wasteful if the sensor is the primary source of noise. The noise in a system can come from any number of sources within the system. An equation describing these sources is given in Eqn. 3-2. Three generalized noise sources are given, sensor noise, circuit noise, and environmental noise. Sensor noise often comes from the intrinsic behavior of the materials chosen and what in how they are used. For example, magnetic sensors often have noise due to 1/f noise, hysteresis, and thermal fluctuations. Circuit noise can and will come from every point in the signal chain. A couple of examples of such noise include Johnson noise, shot noise, and signal coupling within the circuit. Environmental noise comes from other unintended signals in the environment such as other electronics, radio waves, thermal changes such as air conditioning, mechanical vibrations, and more.

$$Noise_{total} = Noise_{sensor} + Noise_{ciruit} + Noise_{enviormenal} \qquad (3\text{-}2)$$

Environmental noise sources can be hard to control. It often becomes an exercise in understanding what noises may be encounter and how to compensate for them. One strategy is shielding. Insulation can be used to protect from thermal fluctuations. EMI can be shielded in part by using a grounded case around a circuit, or a magnetically shielded case to minimize external magnetic fields. A second strategy can be tuning the frequency band of the sensor. If there is a know frequency range of the signal of interest, the circuit can be tuned to be sensitive to this frequency band using a filter. Alternatively, the sensor may be able to modulate the frequency of the signal, which again would allow the sensor to hone in on a frequency away from the external noise sources. One pervasive noise source is 50Hz/60Hz noise due to the frequency of power lines. This is handled in several ways, including the use of notch filters that directly cut this noise down, and good grounding techniques within sensors signal chain circuits.

Minimizing circuit noise is the domain of a good ASIC and/or circuit designer.

While all circuit designs should consider circuit design noise aspects, the extent to which this is done is dependent on application. A picoTesla sensing magnetometer will require infinitely more work controlling noise than an Earth's field or greater sensing magnetometer. Component choice is critical to getting the highest performance out of a circuit. Choosing the best technology for the sensors amplifiers, what types of integration techniques it may utilize, the input impedance, bias current, power, and more are choices the good ASIC designer will help make. Similarly, on a PCB circuit component choices, component placement, trace layout, and noise suppression techniques can make or break a circuit. For example, placings a switching circuit or a power source right next to a low noise amplifier will almost certainly couple noise into the sensors signal. Similarly, a high voltage trace next to a low voltage trace could do the same.

While addressing all noise sources is essential in attaining a high sensitivity circuit, special attention will be paid to the sensor technology specific noise sources. Magnetic sensors can be everything from a simple loop of wire to highly complicated thin-film resistors with flux guiding, mems resonators, piezoelectric actuation, controlled feedback and more. The strategy to minimize the noise is highly dependent on the technology as will be discussed concerning each technology.

3.2. Inductive sensors

Inductive based sensors, in a broad term, are the most commonly used sensor/transducer technology. As discuss was Chapter 2, inductive sensors rely on a time changing magnetic flux through the coil which induces a current into the coil. One could physically move or rotate the sensor in Earth’s field, for example, and the voltage output would be proportional to the portion of Earth's magnetic field captured by the coil and the rate at which the coil is rotated. This type of sensor is called a rotating coil magnetometer and can be used to measure DC field. More typical is where the sensor is kept fixed while a time-varying field such as a sine wave is applied to the sensor. For both cases, the voltage generated can be given by Eqn. 3-3, where μ_0 is the permeability of free space, n the number of turns, A the area of the coil and dB/dt the time-varying magnetic flux that travels normal to the coils cross-sectional area. The μ_r term is for the relative permeability

of the core, which is relative to the vacuum permeability of free space and so unity in a vacuum. Often, there is no core and so μ_r of air is used, which is typically taken to be 1, though more accurately, air is paramagnetic, and the value is 1.000,000,37[4]

$$V = \mu_0 \mu_r n A dB/dt \tag{3-3}$$

There are several advantages and disadvantages of an inductive sensor that should be considered when determining whether they are the right choice for a given application. Properties of the coil such as size and manufacturability may affect its usability and cost. At the same time, the sensitivity, noise, frequency effect, and size from a performance point of view have to be considered.

The SNR as previously noted, is probably one of the first considerations when using a sensor, and inductive sensors are certainly no exception. For an inductive sensor, the primary contributors to its sensitivity are the $\mu_r, n, A, dB/dt$. Each of these values can be optimized but often at a cost. The noise of the sensing element(excluding the circuitry), is typically limited by the thermal noise given by Eqn. 3-4,

$$Vnoise = \sqrt{4 k_B T R \Delta f} \tag{3-4}$$

where $k_B$is the Boltzmann constant, T the temperature, R the DC resistance of the sensor, and Δf the bandwidth of the measurement, often taken to be 1Hz. Other noise sources of the inductive sensor include thermal noise due to a core(if used), the hysteresis of the core, and environmental noise and circuit noise, Eqn. 3-5.

$$V_{noise} = V_{Thermal,coil} + V_{Thermal,core} + V_{Hyst} + V_{circuit} + V_{enviormental} \tag{3-5}$$

One of the first specifications to consider when making an inductor is the size. Length and area can play a huge role in increasing an inductors sensitivity. The area of the coil increases as r^2 so enlarging the coil quickly adds more sensitivity. Depending on the application, this may not be an issue, but typically it is. An increase in size also yields an

increase in the resistance of the coil. Fortunately, this is typically outweighed by the sensitivity improvements and the ability to reduce turns. Size lengthwise is also an essential factor. A longer sensor allows for more turns and a longer core which increases permeability as noted in chapter 2. The primary downside to length is the size and spatial resolution. If the time changing field has a large spatial gradient within the volume of the sensor, then what the sensor measures is the average magnetic field value in that volume. Depending on the spatial resolution requirements, this could be a challenge. An interesting approach to this comes in the form of a spherical coil[7]. The concept behind it is that once the voltage from each turn is integrated the voltage is proportional to the magnetic field at the center of the coil. Unfortunately, this shape is inconvenient, and so "barrel" shape inductors have been designed to try and take advantage of this effect[15].

The second option to consider in an inductive sensor is the core material which gives the μ_r term in Eqn. 3-3. The core material can give a sensitivity increase ranging from 1x to 1,000,000x. With a high permeability core comes the limitations of ferromagnetic materials. The first is that since a ferromagnetic core can saturate the sensor will have a limited range of use. Once the core saturates, it acts as an air-core ($\mu_r \approx 1$) sensor, so it may still be useful if the application can handle the nonlinearity. While the saturation magnetization is a material property, the field at which this value occurs can be controlled to some extent through design. The choice of material and core aspect ratio plays a significant role in this. A high permeability material will saturate at a lower field strength than a low permeability material. Similarly, a high aspect ratio core will have higher permeability and a lower saturation point than a low aspect ratio core of the same material (along its c-axis). For inductive sensors, a long narrow core minimizes the demagnetization factor, N_{demag}, and gives the highest sensitivity along its long axis. The cores permeability can often be estimated using Eqn. 3-6[7].

$$\mu_{core} = \frac{\mu_r}{1 + N_{demag}(\mu_r - 1)} \tag{3-6}$$

The nonlinearity of the cores magnetization curve can also be a significant limitation in the use of cored inductors. To minimize nonlinearity, either a limited magnetic

field range is used, relative to the cores saturation points, or soft magnetic materials specifically designed for this application are used. Soft and linear materials such as permalloy, amorphous materials like Metglass and sintered materials like carbonyl iron are designed for this purpose. Often though, each of these materials comes with their limitations.

Thermal effects can also be a significant issue with a ferromagnetic core. Typically, the permeability of the material will decrease with temperature until the currie point is reached, at which point the material is no longer ferromagnetic. Depending on the sensor application and material, this may or may not be tolerable. Additional thermal effects can come from heating due to hysteresis and eddy currents generated in the material. Typically a high electrical resistance material is chosen to limit the latter while soft magnetic materials typically reduce the former.

The last of the sensor characteristics noted here are their frequency effects. In addition to eddy currents that can be generated in the core as noted above, the inductive sensor is always part of an RLC circuit. Due to this, its response can be modeled as such Figure 3-4 (Left). Depending on the frequency of interest, this can have significant effects. If the sensor only needs to sense a specific frequency, the sensors RLC characteristics can be designed to make this the resonant frequency of the sensor circuit Figure 3-4 (Right). If on the other hand, a range of frequencies needs to be sensed, the resonant peak may be flattened by loading the sensor with external resistance and capacitance or use along a portion of the curve where the frequency response is linear, Figure 3-4.

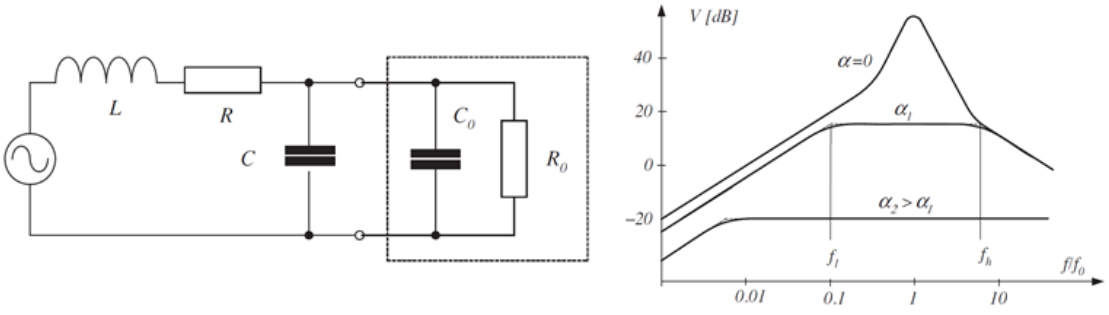

Figure 3-4. Left, representation of inductor as part of RLC circuit with added capacitance C_0 and resistance R_0 to the circuit. Right, frequency response of circuit on left loaded with different amounts of resistance where $\alpha = R/R_0$[7]

One last thing to note on the use of inductive sensors is their manufacturability. Coils can be great for their simplicity and ease of manufacture. A researcher could quickly grab wire off a shelf and wind one. In commercial manufacturing where tight tolerances are often demanded along with high throughput, coils can become a struggle to produce. Inductive coils today can be made with a wire down in the 10µm range which can yield sub-mm diameter coils capable sensing with pT range resolution. In order to make these miniature coils, significant effort has to go into the machine design, set up, and handling processing, which limits commercial output and increases the cost. Currently, only the best MR sensors can come close to this, though there are tradeoffs. With micro-manufacturing, MR and hall sensors can be made in the 10's of thousands per wafer and costing pennies in volume, which makes coils look like ancient technology. With that said, it is hard for any other magnetic technology to sense such a wide range, have high SNR and size of inductive coils, which can make them worth the extra manufacturing cost.

3.3. Hall sensors

One of the most common magnetic sensors in use today, the Hall-effect sensor, has been in use since the 1900s. While newer magnetic sensors are continually being developed, Hall effect sensors have continued to advance. The vacuum tube sensors of the past have been replaced with modern chip packaging technology. Conventional Hall-effect devices and measurements have been used in everything ranging from the ignition timing of cars, keys on a keyboard, to the measurement of electron and hole mobility of semiconductors.

The ease with which Hall sensors can be manufactured is in part the reason why they are so widely used today. Hall sensors of the early to mid-1900s used vacuum tubes for amplifiers and other circuitry which limited their use to mainly laboratory devices[16]. The development of semiconductors led not only to the shrinking of the size of the external circuitry but also to increased use of the Hall sensors. The manufacturing of basic Hall sensors is done using the same processes as used in the semiconductors industry. Most modern Hall sensors use doped semiconductors as compared to metals that were used in the first Hall experiments[17]. The use of doped semiconductors vs. metals increases the

Hall voltage of the sensors due to the larger Hall resistance and allows the use of semiconductor processing technology. Thus, as semiconductor processing advanced, so to did the development of Hall sensors. This has helped to bring down the cost of a Hall sensor in the same way the transistor's cost has dropped. Today, a Hall sensor can be purchased for pennies, and easily integrated directly into an ASIC design.

3.3.1. Hall Physics

It would be fair to say that any student who has taken college physics has probably been introduced to the phenomena of the Hall-effect, though a brief review is often helpful. The Hall-effect is due to the interaction of a magnetic field with holes and electrons. In an electric field, the force [N] on a moving charged particle is given by:

$$F_{Electric} = q_0\vec{E} \tag{3-7}$$

where q_0 is the charge of a particle 1.6x10-19 C, and E is the electric field (V/m or equivalently N/C). The force of the magnetic field acting on the charged particle is given by the Lorentz force:

$$F_{Lorentz} = q_0\vec{v} \times \vec{B} \tag{3-8}$$

where $\vec{v}$ [m/s] is the carrier drift velocity of the charged particle and $\vec{B}$ [T] well-recognized the magnetic field acting on the particle. The sum of the two forces on the particle is then given by Eqn. 3-9.

$$F_{Total} = q_0\left(\left(\vec{v} \times \vec{B}\right) + \vec{E}\right) \tag{3-9}$$

F_{Total} then induces the charge carrier to take a curved path. Depending on the nature of the velocity and the magnetic field, the trajectory can be a circular or helical in the direction of the current flow. Given the thin nature of Hall devices, this ends up being more arc-like [16].

From Eqn. 3-9 the electrical characteristics of the Hall device can then be described. Figure 3-5 illustrates the typical set up of a Hall-effect measurement in a metal similar to the one originally performed by Hall.

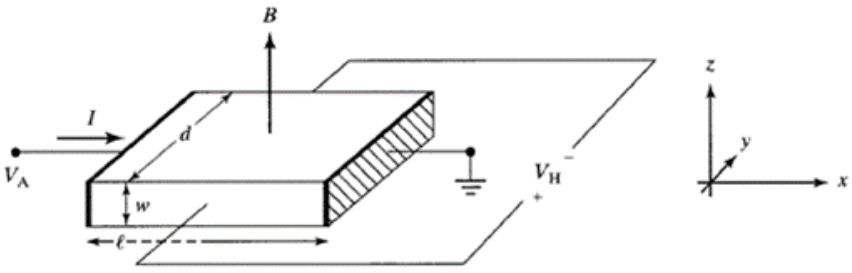

Figure 3-5. Diagram of hall measurement[18].

In the diagram, the current is the x-direction, and the magnetic field is being applied perpendicular to the current in the z-direction. In the direction transverse to the current, y-direction, a voltage can be measured. As the current travels through the metal, the force acting on the charge carriers is given by Eqn 3-9, and the carrier drift velocity is given by:

$$v = \frac{I}{q_0 NA} \tag{3-10}$$

where N, is the density of carriers (carriers/cm^3), A is the cross-sectional area (cm^3), and I is the current [A].

When measuring the Hall voltage, V_H [V], if the transient effect is neglected, it can be assumed that the electric field and Lorentz force are at equilibrium in the y-direction such that,

$$F_{Total} = q_0\left(\left(\vec{v} \times \vec{B}\right) + \vec{E}\right) = 0 \tag{3-11}$$

which in turn yields,

$$\vec{E} = -\vec{v} \times \vec{B} \tag{3-12}$$

Through integration across the width of the slab, d, the Hall voltage can be given by,

$$V_H = d\vec{v}B \tag{3-13}$$

then through the use of $I = Ndw\vec{v}e$,

$$V_H = \frac{IB}{q_0 Nw} \tag{3-14}$$

which is the standard equation for the voltage across a Hall device.

For Hall sensors, there are several noteworthy parameters used in their design and use. From Eqn. 3-13, V_H is directly dependent on the distance between the probes, velocity, and the magnetic field. This can be important in the design of sensors where typically a design as small as possible is desired. A small sensor area can severely cut down the V_H, especially in a metal Hall sensor where v is quite small. From the second form of the equation, Eqn. 3-14, it can be seen that V_H is inversely proportional to the carrier concentration, which can have a significant impact on the Hall voltage, and will be discussed next.

The Hall-effect in semiconductors, while essentially the same as that of metals, is distinct because the material properties of semiconductors allow for a more optimized design. As noted above, the Hall voltage is inversely proportional to the carrier concentration. For metals, this is very high on the order of $1x10^{23}/cm^3$. In contrast, for SI, the intrinsic carrier concentration is $1.5x10^{10}/cm^3$. This can make a significant difference for Hall devices in semiconductors as compared to metals.

Looking at Eqn. 4-15, and comparing with Ohms law,

$$V_H = \frac{IB}{q_0 Nw} = I \cdot \frac{R_H}{w} \cdot B \tag{3-15}$$

where $R_H$is the Hall resistance which can then be given as,

$$R_H = \frac{1}{q_0 N} \tag{3-16}$$

For a semiconductor, it is well known that the resistivity,ρ, is inversely proportional to the carrier mobility, μ, and carrier concentration, n and p, and is given by,

$$\rho = \frac{1}{q_0(\mu_n n + \mu_p n)} \tag{3-17}$$

For a doped semiconductor, the resistivity can then be expressed by Eqn. 3-16.

$$\rho = \begin{cases} \frac{1}{q_0 \mu_n n} \text{ for } n \gg p \\ \frac{1}{q_0 \mu_p p} \text{ for } p \gg n \end{cases} \quad (3\text{-}18)$$

This yields the Hall mobility, μ_H, of the semiconductor as

$$\mu_H = \frac{R_H}{\rho} = r_H \mu_p \text{ or } r_H \mu_n \quad (3\text{-}19)$$

where r_H has been introduced as a correction factor for the Hall resistance. For the Hall resistance, it varies based on many factors of the measurement such as temp, material, carrier type, B strength, and scattering mechanism[18]. The value is typically near unity and rarely varies by more than 0.5. Additionally, the value of r_H approaches unity as $B \to \infty$ [18], so omitting this factor does not necessarily diminish any results. As a more general form of the Hall resistance based on Eqn. 3-18, and 3-19, one can write the Hall resistance as

$$R_H = \frac{r_H}{q_0} \frac{\mu_p^2 p - \mu_n^2 n}{(\mu_p p - \mu_n n)^2} v = \frac{I}{q_0 NA} \quad (3\text{-}20)$$

Thus, from a simple semiconductor I-V measurement, if one carrier is much more heavily doped than the other, carrier concentration and mobility can be determined as shown below. It should also be noted that often in the literature the measured values listed for $n, p, \text{and } \mu_{p \text{ or } n}$ are based on the assumption $r_H = 1$[18].

$$n \text{ or } p = \frac{r_H}{q_0 R_H} \quad (3\text{-}21)$$

And

$$\mu_p = \frac{R_H}{r_H \rho} \quad (3\text{-}22)$$

3.3.2. Hall effect geometry

While the diagram of Figure 3-5 is the typical geometry shown in most textbooks describing the Hall-effect, in practice, this geometry is modified or even thrown away all together. The three most basic Hall structures used are the rectangle, cross, and diamond[18]. The geometry can have a significant effect on the function of the sensor. Many variations of hall geometry are available in the literature, though analysis and optimization of a few of the basic structures are common [16,19, 20].

A general rule for the Hall device is that the length, d, between the biasing electrodes, should be three times that of the width, d, between the probing electrodes[21]. This helps prevent the charge carriers from reaching the other side of the biasing electrodes before being substantially deflected. Often a geometric factor, G, as a function of l/d can be introduced to account for this, and V_H is then given by Eqn. 3-23[21]. In [17], a more in-depth look at the geometric factor is given based on numerical simulations where a more complex form of G is presented.

$$V_H = G \cdot R_H \cdot d \cdot B \qquad (3\text{-}23)$$

One geometry worth noting is the vertical Hall sensor geometry. This geometry is quite unique in design though ubiquitous among many modern Hall-effect designs. Describing this design must be done with a picture in mind. Figure 3-6 shows the original drawing of this design[22]. First, imagine a conventional Hall device. Then take that device and, while keeping it planar, bend the two sensing contact in a “U-like" fashion such that when done you have three terminals in a "w-shape” where the sense electrodes are at the outside of the w, and one of the current electrodes is at the center. Initially, one may think that this configuration would significantly change the physics of the device, though in reality it does not, other than that, it allows measurement of a magnetic field in the plane of the device. Combining this technology with tradition Hall allows for the fabrication of a compact 3-axis Hall sensor.

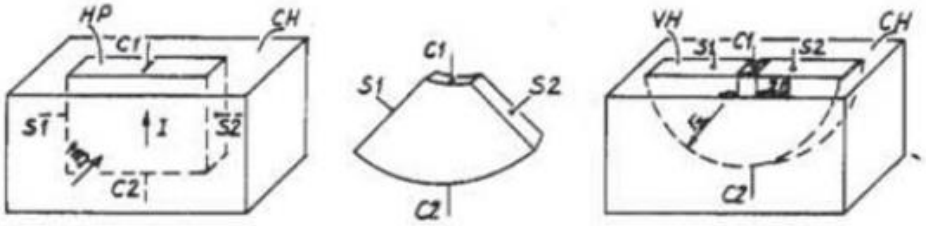

Figure 3-6. Vertical hall geometry[22].

3.4. AMR sensors

Of the MR technologies, AMR (Anisotropic MagnetoResistance) is the most mature, having been discovered back in 1851 by Sir William Thompson. The AMR sensor did not start to become the well-recognized sensor that it is today until the 1970s. As vacuum deposition and thin-film processing advanced along with the semiconductor industry, so did the computer industry's need for smaller and smaller sensors to read the shrinking size of magnetic media. Hard drive read head development drove a lot of MR technology advances both commercially and in research labs across the world.

For AMR, the change in resistance comes from the change in electron scattering due to an applied field. Figure 3-7 illustrates the basic principle of AMR. The image shows a strip of ferromagnetic material, with electrical contacts at both ends. The resistance of the strip can be given by Eqn 3-23. In Eqn 3-23, R_0 is the base resistance of the strip, ΔR the maximum change in resistance, and α the angle between the strips magnetization and the current direction. The maximum change in resistance of the strip normalized by its base resistance is referred to as the strip magnetoresistivity coefficient, Eqn 3-24. For permalloy, a common AMR material, the change is typically around 2%[7]. As current is driven through the strip, a base resistance can be measured. When a magnetic field is applied perpendicular to the direction of the current, Figure 3-7b, the electron scattering events decrease, and a drop in resistance is measured.

$$R_{amr} = R_0 + \Delta R \cdot \sin(\alpha) \qquad (3\text{-}23)$$

$$\%AMR = \frac{\Delta R}{R_0} = -\frac{\Delta \rho}{\rho} \sin^2\theta \qquad (3\text{-}24)$$

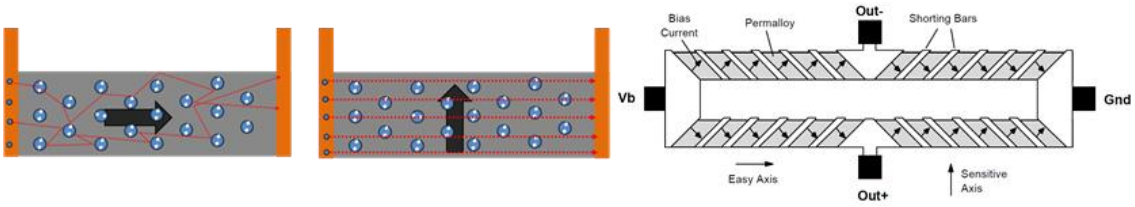

Figure 3-7. Illustration of AMR effect. Left, high resistance configuration and, low resistance AMR strips. Right, Barber pole style AMR sensor[23].

For AMR, when used as a magnetometer, the most common style of AMR sensor is the Barber pole style AMR sensor, Figure 3-7. The advantage of the barber pole is that it makes the sensor linear about the zero applied field point. Four of the barber poled elements can be placed into a bridge on a single die, which helps to create a near-zero offset voltage (within the tolerance of manufacturing a balanced bridge). Additionally, the push-pull style bridge helps increases sensitivity. For high sensitivity AMR sensors, there may only be a few percent change in resistance, which makes getting the 2x increase of using all four bridge elements active is very important.

For the AMR as with the other sensors, the SNR, linearity, and range are of significant importance. The noise of the AMR comes from two primary sources. The first being the 1/f noise which is due to domain fluctuations and the second being linearity. The 1/f noise dominates at low frequencies, but for AC waves by the time the sensor gets in the range of a couple of tens of Hz to hundreds of Hz, the prominent source of noise is thermal. For the linearity, this issue occurs due to the saturation of the material. Since the ferromagnetic strip will saturate there is a limit at which the sensor response will become highly nonlinear. One technique to extend their linear range is shorten the strips aspect ratio, thereby decreasing the permeability of the strip and increasing the field that can be applied before saturation. Unfortunately, this technique also decreases the sensitivity of the sensor in a near proportional manner. A second technique is to limit their range to limited portion of the transfer curve which decreases the total signal that will be received to only a small portion of the %MR of the sensor. One technique for getting around this is to use a magnetic

field feedback system which nulls the field to keep the senors in its linear range. The current used in the feedback system is then measured to determine the magnetic field. To implement a system like this requires more power, size, and complexity, which may not be acceptable.

3.5. GMR sensors

GMR(Giant magnetoresistance) is relatively new when compared with inductive, hall, and AMR. In 1988 groups led by Albert Fert and Peter Gruenber Independently discovered the GMR effect[24]. In the Hard drive industry, this was an enabling technology which allowed them to significantly increase density in the 90's due to the small size, sensitivity, and mass manufacturability of the sensors. The technology was primarily driven by the Hard drive industry, though the breakthroughs and scientific knowledge gained there helped to propel their use as magnetometers. The technology also led to discovery TMR, which is now a competing technology to GMR and AMR.

3.5.1. GMR physics

The basic physics of the GMR structure is shown in Figure 3-8. A three-layer sandwich structure is shown. In this sandwich structure, there is a ferromagnetic(FM) base layer (light grey) and a ferromagnetic top layer (dark grey) separated by the conductive nonmagnetic(NM) spacer layer (orange). For this structure, one of the FM layers is called the pinned layer since its magnetization is fixed in one direction. The second FM layer is called the free layer since its magnetization is able to rotate with an applied field. The middle NM layer is typically a good conductor of some sort, such as Au, Ag, Cu, Cr, or other. The concept behind GMR can be described as spin-dependent scattering. Figure 3-8 shows a GMR sensor in two different states, field parallel(Left) and field perpendicular(Right) to the long axis of the GMR element. The resistance of the sensor is dependent on the magnetization angle between the two FM layers. As the angle increases from 0° to 180°, the sensor goes from its lowest resistance state to its highest resistance state. The reason this occurs is due to the mean free path of the electrons. Scattering off the top and bottom surfaces increase the resistance, which is proportional to the angle between

the two FM layers. Due to this, the mean free path is one of the primary considerations when determining the thickness of the NM layer. The NM layer needs to be such that the electrons interact with both layers, and is typically on the order of 10nm[25].

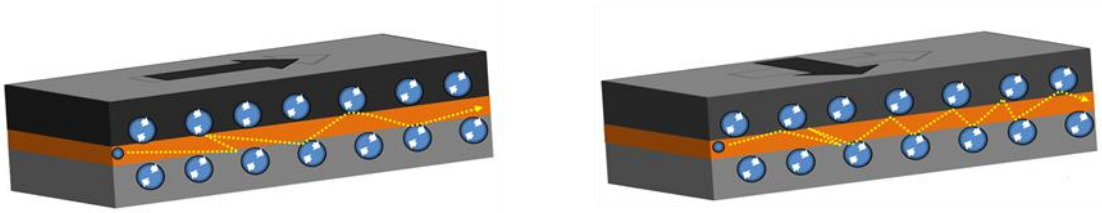

Figure 3-8. Basic way GMR works

Figure 3-8 shows what would be considered a current in plane(CIP) spin valve, though with a few modifications, this could have been a current perpendicular to plane (CPP) spin valve or what is often called a multilayer(ML) GMR sensors. For a current CIP vs CPP, as the name suggests, the current flows either in-plane as in Figure 3-8 or perpendicular to the plane for the sensors shown in Figure 3-9.

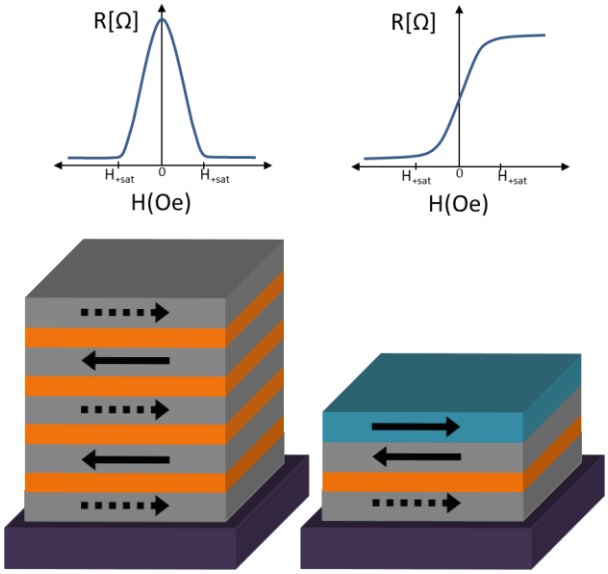

Figure 3-9. Current perpendicular to plane sensor. Left, GMR multilayer. Grey layers are ferromagnetic and orange are conductive. Right, Spin valve GMR. The top layer is for antiferromagnetic pinning.

GMR Spin valves(SV) and GMR ML sensors are similar in that both can use CPP, multiple layers, and scattering at the interfaces of those layers to produce resistance, the

main difference is in the magnetic layer pinning and magnetic coupling of the layers. In general, the ML relies on AF coupling between the magnetic layers such that the applied field works to overcome the AF coupling. The ML is typically composed of multiple FM-NM layers. Spin valves, on the other hand, do not rely on the AF coupling between FM layers. Instead, the pinned FM layer is uncoupled or weakly coupled to the free layer. The pinned layer is typically AF coupled to another layer, or a magnetically hard layer is used and set is in the desired direction. It is worth noting that overcoming the AF coupling in the ML sensors can require a strong field in the 10KOe range, whereas the SV with its weak coupling can easily be used in the single Oe range. One other distinguishing feature can be their transfer curves. As shown in Figure 3-9, ML sensors have a bell-shaped transfer curve, whereas SV sensors tend to have more of a sigmoidal shaped transfer curve. If the field being sense requires bipolar differentiation, an SV may be the best choice.

3.6. TMR sensors

The newest of all the MR technologies listed is TMR. As noted above, a large portion of TMR's development was driven by the hard drive industries need to increase memory density. Interestingly, the theoretical physics of TMR were predicted in 1971 and then confirmed in 1975, but at low temperature. Unfortunately, the technology to produce high-quality pinhole-free oxide films was not available. The first successful TMR at room temp was prepared in 1995 using an AlO2 insulating layer[7]. The Hard drive industry was very interested in this technology, and the first TMR read head was introduced in 2004 by Seagate[26]. In the last decade, TMR's use has expanded immensely with relatively quick adoption. Today several commercial sensors can be purchased from NVE, Multidimention Technology, Sensitec, Bosch, Micromagnetics, and more.

The physics of the TMR shares some similarities with that of GMR. Namely, the magnetic coupling between FM and AF layers. Beyond this, there are stark differences between the two. The TMR structure is typically like that of the SV in Figure 3-9, but instead of a conductive layer, there is a nonconductive oxide layer. Due to the presence of the oxide, conduction electrons cannot pass through as they would in a metal.

For TMR sensors, there are two main types classified by the type of Oxide used. AlO_2

was the first material in which TMR was demonstrated and then again the first material to be commercialized. For AlO_2, the highest %MR ratio that has been obtained was 80%[7]. In the 2000s development of MgO based TMR has led to %MR ratios of up to 600%[27]. While AlO_2 was first to be commercialized, The higher %MR ratio of MgO is leading it to replace AlO2 as the technology of choice.

For TMR sensors, while they do have large %MR ratios, which yields high sensitivity sensors, they can also have significant noise. For TMR sensors, the parameters affecting their sensitivity was explained well by Egelhoff[28]. Below in Eqn. 4-25 the total noise power, S_B, come from multiple sources including the Amplifier noise S_b^{amp} (note this is not intrinsically part of the sensing element), S_b^{shot} shot noise, $S_b^{elec\ 1/f}$ the electric 1/f noise, $S_b^{therm.mag}$ the magnetic thermal noise, $S_b^{mag.1/f}$ the magnetic 1/f noise. From this analysis, it is easy to see that the noise in TMR can be quite complicated. Noted in the paper is that reduction of B_{sat} can give a substantial reduction in noise, though at the same time this would tend to limit the range and linearity of the sensor. Sensor noise also changes with voltage, which can be advantageous from a power perspective, though at the cost of the signal. Lastly, just like AMR and GMR, TMR is also strongly effected by 1/f noise. One approach to minimize the sensors noise is to us a mems device to modulate the signal to a higher frequency where the noise is lower[28], [29]. For these methods, it introduces more complexity, and to the author's knowledge, no such sensor is on the market. Interestingly, as shown in Figure 3-10, the company MultiDimension Technology now sells a TMR device that achieves sub nT resolution near DC and would have similar noise to that of [28] and [29]without the modulation.

$$S_B \approx \frac{4B_{sat}^2}{\left(\frac{\Delta R}{\bar{R}}\right)^2 N^2 V_J^2}\left[S_V^{Amp} + N\frac{2eV_J[RAP]}{A}\coth\left(\frac{eV_J}{2k_BT}\right) + \frac{N\alpha_{elec}V_J^2}{Af}\right] + \frac{4k_BT\mu_0\alpha_G}{N\Omega\gamma M_s} + \left(\frac{2B_{sat}}{\Delta R/\bar{R}}\right)\frac{\alpha_{mag}}{N\Omega f} \tag{4-25}$$

3.7. Comparison of MR technologies

From the above discussion above, it can be seen that there is an obvious difference

between the MR types though there is also some strong commonality. They all have to deal with magnetic noise sources and thermal noise. For TMR and GMR, they are both a multilayered technology in comparison to AMR, which yields advantages and disadvantages.

The frequency at which the sensor is to be used can play a large impact on sensor technology chosen. In Figure 3-10, noise plots for some commercial high-performance AMR, GMR, and TMR are shown[28], [30]. In general, AMR typically has the lowest noise in the low-frequency regime up to about a couple hundred to a couple of hundred Hz. The MDT TMR 9001 is exceptional with respect to their lower noise, but it comes with the caveat of relatively large die area and significant cost. In the single kHz range, the noise of each technology can be comparable. In this case other factors such as linearity, cost, and power may drive the decision. Above 10 kHz, the 1/f noise of most TMR starts to level off, and TMR and GMR start to outperform AMR from a noise perspective.

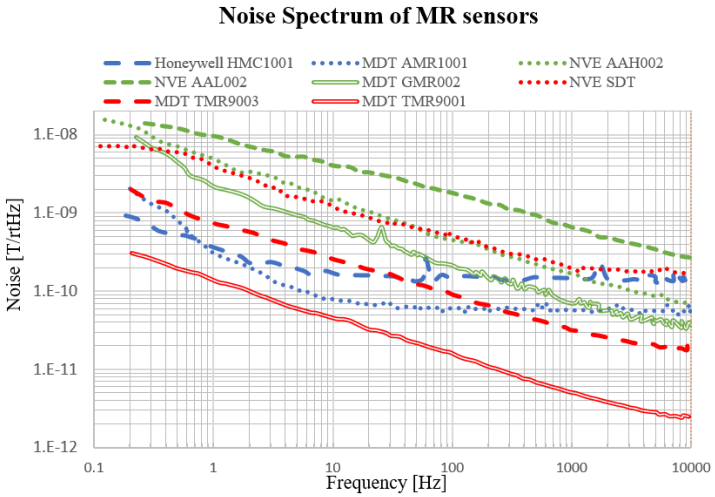

Figure 3-10. MR noise[28], [30].

Between the three sensor types, the choice of technology may depend on signal strength and power. As mention above, AMR may only have a %MR around 2%, whereas GMR can be in up to 5%-20% range, and TMR can be 100% or more[31]. If the application allows for a preamplifier in very close proximity to the sensor, signal strength may not be a driving factor. On the other hand, if there is a concern that noise may couple into the signal lines before it can be amplified, having the larger signal of GMR or TMR would be advantageous. For low power applications, the high resistivity of the TMR can offer a significant advantage. For TMR though, it comes at the cost of ESD sensitivity, and the

disadvantage of high impedance lines such as potential noise coupling and the need for a high input impedance preamp. GMR and AMR can get away without ESD protection as long as it is not being used in conjunction with ESD sensitive ASIC components.

Two more factors not mentioned yet for the MR sensor is hysteresis and thermal drift. All the MR sensors suffer from thermal drift. The values of this are typically in the thousands of ppm/K. This can add a significant offset and drift to the performance of a sensor if this is not known. Similarly, hysteresis can play a significant role in sensor nonlinearity as well. Most manufacturers will list the hysteresis of their sensor and sometimes even call it hysteresis-free, though there is typically some. Hysteresis values below 0.1Oe can be obtained, and AMR probably has the least, which can be sub 0.01Oe. The one catch with AMR is that they typically require a reset coil in order to set the magnetization direction of the sensor. The sensor must be reset if too large of a field is seen or if it starts to drift with time. On the upside with the reset coil, it does allow some degree of thermal compensation.

Finally, the obvious differentiator beyond all technical considerations is the price. Currently, AMR and GMR being the older technologies they are easier to fabricate and tend to be cheaper than TMR. Still though, Hall effect sensors are the cheapest to produce and thus are often the cheapest option, especially when ASIC integration is required for the application. As MR technology continues to develop this may change at some point and make MR technology more competitive from a price perspective.

3.8. Sensor Conclusion

As discussed in this chapter, numerous types of magnetic sensors are available, and they each have their advantages and disadvantages. Inductive sensors, while a very old technology, they have stood the test of time and continue to be some of the most sensitive AC magnetometers available. The largest sector of magnetic sensors in use today is in the consumer electronics industry in which cell phones, cameras, computers, and more all contain magnetic sensors for compassing or other sensing applications. As such, the fields sensed are on the order of the Earth's field (0.5G or 50μT). This is relatively easy to sense for Hall, AMR, GMR, or TMR, and thus the main criteria that drives their use tends to be

cost. Higher performance applications such as geolocating, distance, and rotation sensors such as those used in aerospace, medical, automotive, and other industries where higher performance is required is likely the areas where MR technologies may have the most impact. As MR continues to develop and become a widespread technology, its price is likely to become more competitive with Hall.

4. MAGNETIC SENSORS FOR MEDICAL DEVICES

4.1. Intro

The use of magnetic sensors in medical devices is an area of particular interest to the author. Within medical devices, there are many unique applications in which magnetics play a role. Depending on the application, the type of sensor and how it is implemented may change. Four general categories of medical devices that utilize magnetic sensors are implantable devices, medical wearables, diagnostic/hospital equipment, and catheters/ electromagnetic navigation. While each of these categories is quite different, they all work to improve/monitor our health and as such, often require some different design considerations vs. what might be used in other industries such as automotive, aerospace, and consumer electronics.

Implantables and wearables are two categories of medical devices that can have similar requirements. Both types of devices typically run off battery power, require small form factor, and often measure moderate fields (0.1 Oe to 100 Oe). In these devices, the magnetic sensor may perform various functions, including acting as a magnetic switch to modify the state of the device, measuring current delivered, or even orientation. If the device is measuring current in its internal circuity or an easily detectable field, it may be possible to integrate a hall sensor directly into the ASIC. If integrating a hall directly into the device's ASIC is possible, this is probably one of the best solutions for cost and size. Other thin-film technologies such as MR can be integrated onto ASIC though this often requires a secondary manufacturer to do post-processing of the ASIC, which may not be practical. While a sensor may not be able to be integrated directly into the device's ASIC, most manufacturers will offer their magnetic sensors with ASIC in a chip-scale package or

even raw die if required. If a non-integrated technology is to be used, TMR can be a good choice due to its very low power requirements. No matter the sensor, it is also advantageous in these applications to power cycle the device so that it is only on as often as need be to save energy. The power cycle may be on for only a few milliseconds a minute, depending on the required measurement frequency and accuracy. One additional requirement for the implantable devices can be the ability to go into an MRI, which again introduces the large field requirement. For implantables, sensor reliability can one of the most significant concerns. Fortunately, this does not tend to be an issue for most magnetic sensor types. Many magnetic sensors are built to withstand the harsh conditions of automotive applications where harsh chemicals, vibration, and temperature are present, so the human body is relatively benign. Typically, as long as the sensor can make it through the manufacturing and burn-in process without error or unexpected drift it is unlikely the sensor will see these harsh conditions in regular use.

Medical equipment such as lab measurement devices and Operating room equipment includes a broad range of applications. These applications can include everything from position/rotation sensor on a fluoroscope to a microbead sensor for a protein assay. As such, the requirements can significantly vary, though there is some commonality. Sensors in these applications typically have to work in a standard operating room (OR) environment, though they often have fewer size constraints. Shielding and or larger signal sources can also be used to improve their SNR. For a fluoroscope rotation sensor, it may work based on a sensor that measures the field of a reference magnet. As such, the magnet can be tuned to help with the SNR. For a protein assay or even a microflow sensor (Ch6), the magnetically sensitive portion of the device may be able to be shielded from outside interference. Additionally, these sensors do not typically have the power constraints of implantable or catheter-based applications, which may allow increased sensor performance. Without a small power requirement, active sensors with secondary fields or aligning fields may be used to reduce noise or put the sensor in its sensitive range. In these applications, fields over a couple of hundred Oe are rarely present, so the use of high permeability materials is possible as well.

One of the most well-known uses of magnetics in medicine is magnetic resonance imaging (MRI). MRI may be the most important and successful use of magnetics in the

medical field. An MRI image can allow a physician to perform a sort of magnetic X-ray of the patient and get a 3D image of the inside of a patient. Physicians can use this data to look for number abnormalities that may be causing some ailment within the patient. Inside the MRI is a fascinating mix of electromagnetic fields. The most well-known field is the B_0 field, which is a static field of 1.5T or 3T. Beyond that, there are three more magnetic gradient coils (X, Y, Z coils) used to generate 3D gradient fields in the mT range and then there are RF-coils used to perpetuate and measure the H-ions in the cells

With all the magnetic fields and large magnitude of the signals, some might think it would be trivial to create a sensor for this environment. In reality though, some consideration must be given in order to choose the best technology. Due to the large B_0 fields of the MRI, many sensors will not works. The large field will saturate most sensors that rely on a ferromagnetic material as part of its sensing mechanism. This primarily leaves inductive air coils, Hall sensors, and NMR based magnetometers as solutions. The inductive coils can only be used to sense the gradient and RF fields due to needing the varying time field. The Hall can potentially measure both the static and dynamic field, while the NMR would struggle with the dynamic field due to their temporal resolution. For either sensor, some form of filtering/shielding consideration would undoubtedly be needed as it is likely that the high-frequency fields could easily induce noise into the system.

The last application and one of notable interest is the use of magnetic sensors in catheters and non-invasive procedures. There are several ways a magnetic sensor can be used in a catheter, though the vast majority of the work found is in its use for force sensing and electromagnetic tracking (EMT)[32]–[34]. In a force-sensing application, the goal is typically to measure the amount of force a catheter is applying to a tissue. This information helps physicians gain tactile information that can help guide catheter positioning, and more importantly, is its use in RF ablation where the quality of an ablation treatment can be correlated to the pressure on the tissue during ablation. In electromagnetic tracking applications the goal is to use a magnetic sensor to triangulate the position of a catheter within the body similar to the way GPS works, but with magnetic field sources acting as the satellites and the magnetic sensor as the GPS receiver.

The area of EMT has been researched by several authors, though almost none of the work discusses the optimization of the tracking sensors. EMT tracking systems are

typically composed of three main components: a field source, a magnetic field sensor, and the hardware drives the field source, reads the sensors, and processes the signals into position and orientation data. The majority of research involves how to integrate off the shelf (OTS) hardware systems in medical applications with a focus on calibration, registration, and distortion reduction. As research has started growing, several papers have focused on different system architectures and algorithms for EMT[35], [35]. To this author's knowledge though only one paper can be found on the design of sensors specifically for medical applications[36].

Within EMT and navigation in general, two primary types of sensors are often referred too. The first is a five-degree of freedom (5DOF) sensor. The second is a six-degree of freedom(6DOF) sensor. For the 5DOF and 6DOF sensors, X, Y, and Z translations along with pitch and yaw can be sensed. The advantage of the 6DOF sensor is that it can sense roll about its sensing axis, which the 5DOF cannot.

The technology used for commercially available EMT systems is inductive coil or fluxgate sensors based. Both inductive and fluxgate sensors are available in 5DOF and 6DOF versions. For 5DOF, the sensor is essentially a single axis sensor, whereas the 6DOF sensors are composed either a triaxial sensor or two 5DOF sensors canted with respect to each other. The size of the sensors ranges from about 0.4mm to 1cm in diameter and lengths from about 4mm to 20mm. The smaller dia. sensors tend to be oriented to the non-invasive medical market, whereas the larger sensors tend to be used for motion tracking applications such as biomechanics or tool tracking such as for ultrasound probes. For the smallest Dia. sensors, they tend to be 5DOF, whereas the smallest 6DOF is 0.8mm in dia.[36].

Numerous examples of micro wound coils have been shown, though their fabrication is far from trivial. As demonstrated in [37], micro coils can be wound with wire down to 9µm dia. At this diameter Cu wire is exceptionally fragile, hard to produce or even see with the unaided eye. Winding these coils takes special equipment and processing which increases their cost, scrap rate and reduces their reliability. Additionally, the processing of these coils is singular in nature, so the advantages of parallel fabrication such as used in the semiconductor or mems industry are not had.

One approach to solve the issues associated with micro wound coils would be the use of microfabricated coils for EMT. Research into microfabricated can be found in the

literature, though nonspecific to EMT applications[38].The coils that have been fabricated, typically have low aspect ratio structures, and low packing density due to the limitations of lithography and etching. To overcome this and be able to create coils with high aspect ratio features, the novel use of anodized aluminum oxide (AAO) as a sacrificial template for coil fabrication is explored to determine its feasibility for developing EMT based inductive sensors.

4.2. Results

4.3. Basic EMT sensor spec requirements

The foremost concern facing most catheter sensing problems is the size. Catheters can come in a wide range of sizes ranging from around an 8mm dia. for some of the largest down to less than 0.5mm Dia. for some smallest guidewire applications. For coronary, electrophysiology, and pulmonary applications, the catheters are more often in the range of 1mm to 4mm. For these catheters, it must be remembered that the cross-section is round and so the maximum dimension inside the catheter will be notably less than if there was a square package typical of off the shelf sensors (i.e. QFN packaging). Looking at Figure 4-1 and Eqns 4-1,2, the loss in the cross-sectional area is at least 50%. What makes the situation more difficult is that in addition to wall thickness, the catheter may have a braided sheath, electrodes, wires, fluid channels, working channels, thermocouples, and other items that are required. In the case of electromagnetic tracking, the fact that the catheter is tracked is secondary to whatever therapeutic or diagnostic function the catheter provides. The one dimension working in favor of the sensor is the length of the catheter. Catheters are long and narrow objects, which means that this is the primary direction available to work with when greater size is required. With that said though catheters do require flexibility to go through tortuous pathways and flexibility towards the tip in order to precisely perform its function. Attention needs to be paid to what this length can be, and as a general guideline, this dimension is on the order of a couple mm to 15mms depending on the application.

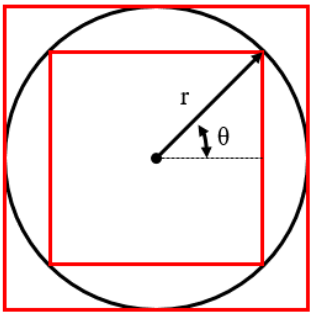

Figure 4-1. Catheter square vs round cross-section

$$A_{out} = 4r^2 \tag{4-1}$$

$$A_{in} = 4r^2 cos(\theta)\sin(\theta) \tag{4-2}$$

A 6DOF requirement means the sensor must have at least two sensing axis, which can be a struggle within the size requirements of a catheter. This is especially true for the off-axis (orthogonal to the length of catheter) direction. From a signal perspective, it is advantageous to have orthogonal sensors such as those of reffs[15], [39]. These sensors take up significant space and seem only to be offered in catheters with limited functionality. A recent approach from Biosense shows the use of three co-axial sensors presumably to allow space for the other functionality required from the catheter[40]. In [36], two different 6DOF sensor design approaches were used. The first is a 6DOF sensor composed of two canted solenoids wound around the outside of a tube with approximately 70° of angle between each coils axis. The second was the use of two 5DOF sensors canted with respect to each other at an angle that is not given. From a geometric consideration of the sensor, given its 0.9mm dia. x 1.8mm length, it can be assumed that there is approximately 20° between the sensors. The final three sensors were 5DOF inductive sensors of varying sizes down to 0.4mm dia. x 8mm length and 0.5mm dia. x 5mm length which could be turned into a 6DOF by canting two with respect to each other.

In EMT extremely low fields must be measured with excellent accuracy, which makes it a particularly interesting magnetic sensor application. For time-varying magnetic fields, IEEE C95 recommends fields no larger than 1mT in the 1KHz to 3Khz range (typical range of EMT), which makes a practical limit to the size of field that can be applied. From a spatial perspective the tracking range of EMT systems tends to be in the 300mm to

660mm range. Utilizing this range and along with the IEEE magnetic field limits, a model of the field sensed by an EMT sensor can be approximated from Biot-Savart, Eqn 2-19. Using a 10mm dia. coil with Current*turns = 300A-turns a field of 30G at 20mm can be generated, which is at the IEEE limit. This coil model suggests that for a sensor to track within a 660mm cube volume, it would need to sense magnetic fields over five orders of magnitude down to 0.001G (0.1μT) and gradients over seven orders of magnitude down to 10uT/mm (1nT/mm), Figure 4-2.

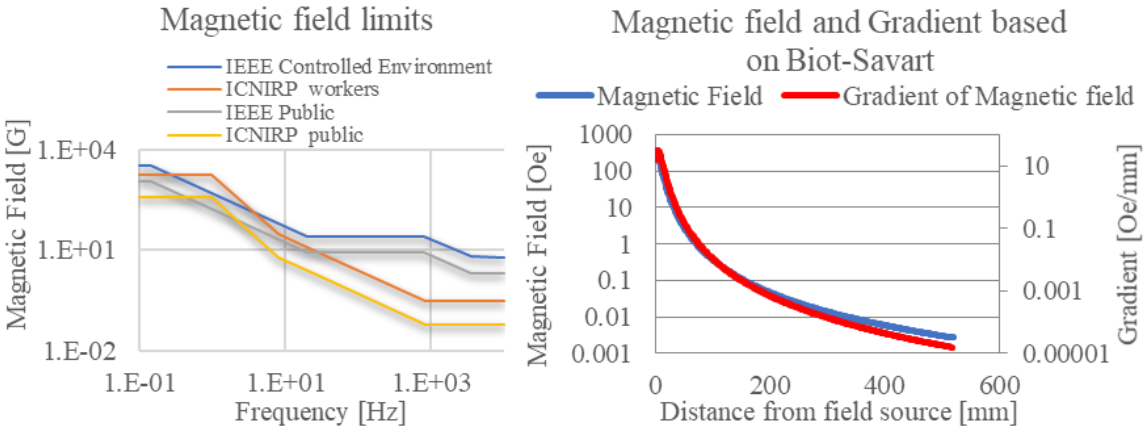

Figure 4-2. Left, time-varying magnetic field safety limits from IEEE and ICNIRP. Right, Model of the simple coil using Biot-Savarts law showing magnetic field and gradient.

The noise sources within a catheter can be unique as compared to traditional consumer electronics. The traditional noise sources discussed in Ch 3 exist, but the medical environment can add additional noise due to equipment in the environment such as x-ray, catheter construction, or other functionalities within the catheter. One common application of catheters is RF ablation for pulmonary, electrophysiology, and urological applications. In these applications, an RF signal is pulsed through the catheter tip to induce therapeutic tissue damage. The power of the signal can be over 50W, and the frequency is typically 300kHz to 500kHz. The RF signals can induce significant noise into a system. What makes the situation worse is that the wires from the sensor may run directly alongside the wire carrying the ablation current, allowing even greater noise pickup. Lastly, the RF ablation adds extra heat to the system. If the sensor is not thermally compensated this may cause accuracy problems. Similarly, other conditions may exist such as ultrasound, impedance signals, forced cooling, vibration, digital signals and more. Thus the catheter environment

itself can be quite challenging.

From the analysis above, a chart showing some desired requirements from an EMT sensor is given in Table 4-1. The combination of size, field strength alone makes finding a sensor no trivial task.

Table 4-1. Proposed EMT sensor requirements

EMT Sensor design requirements	
Max dia.	0.5mm
Max length	5mm
Field range	1mG to 30G (100nT to 3mT)
Spatial field gradient	10μG/mm to 10G/mm (1nT/mm to 1mT/mm)
6dof potential	Min: 2 canted axis Max: 3 orthogonal axis
Frequency range	100Hz to 10kHz

4.4. Inductive Sensors for EMT

Inductive sensors are by far the most used sensors for EMT applications. Two of the most successful systems used in medical EMT are the Biosense Webster (BSW) Carto and the Northern Digital Inc. (NDI) Aurora, both of which use inductive coils. The coils used are available in a variety of shapes and sizes to meet the individual system and catheter requirements.

The NDI Aurora system is the most commonly used in research, and some information is available on their sensor performance, which is used as a base to derive inductive sensors with similar performance. As shown in [36] a variety of inductive sensors designs are capable of being used on the NDI system. In [41], it is noted that one model of the NDI sensor has a sensitivity of 10mV/Hz G^{-1} in addition to a resistance of 70Ω and 2mH of inductance. Using this information along with known equations, the basics of the market available inductive EMT sensors can be estimated and used to determine what room there is for improvement.

Figure 1. from [36] shows a couple of experimental inductive designs very similar to what is used in NDI systems. Using ImageJ, figure ##, dimensions of the sensor core and windings can be determined. From the core dimension along with Eqn 3-6 for a high permeability material, the relative permeability can be estimated as μ_r =1329. With permeability determined, the number of turns can be had using Eqn. 4-3 and assuming a 10mV output at 10kHz and a 1Oe (80 A/m) field.

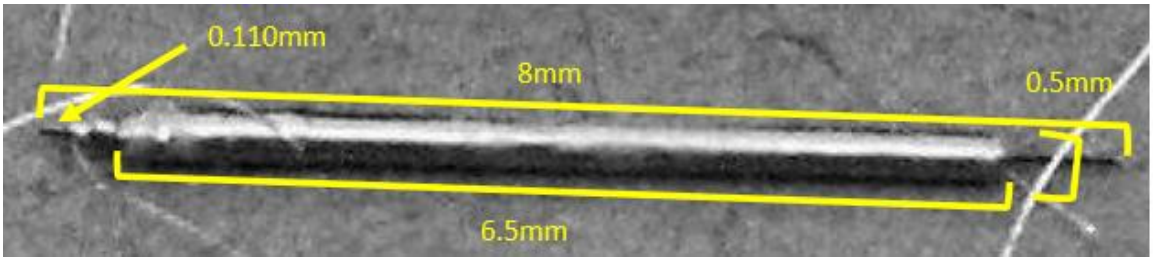

Figure 4-3. Measurements of EMT sensor from [36] using ImageJ.

$$V = \frac{\mu_0 \mu_r nAdH}{dt} = \mu_0 \mu_r nAfH$$
$$n = \frac{\mathrm{V}}{\mu_0 \mu_r nAfH} \approx 1000 \tag{4-3}$$

To confirm these numbers, an equation for the inductance of a solenoid can be used to show that this inductor would have an inductance of 2.2mH, which is a reasonable approximation[7]. A simple calculation based on the estimated cross-section also provides that the wire used for this design is likely in the 30µm or less range. To summarize, the predicted specs of an inductive sensor capable of being tracked by a COTS tracking system can be estimated by the parameters in Table 4-2.

There are two primary ways coil-based sensors are designed for catheters. The first is a coil wrapped around the outer diameter of the catheter's primary diameter. To make these coils, micro winding is typically used. The coils are wrapped with wire with as small as 8 µm Dia. (60AWG) and a couple hundred to a couple of thousand turns can be used. The coil may be wound on a hollow tube, a magnetic core, or a temporary substrate for later processing. Wrapping the sensor on the OD catheter can give considerable advantage in terms of coil area and sensitivity vs a sensor within the interior of the catheter. Using the OD can allow the design to reduce the number of turns or length of the coil and keeps the interior of the catheter free for other devices. The two primary downsides are

manufacturability of the coil and integrating a second axis for 6DOF tracking.

Table 4-2. Estimated EMT inductive sensor specs.

Estimate of OTS EMT Sensor spec	
dia.	0.5mm
length	8mm
Inductance	2mH
Sensitivity	10mV/G @ 10kHz
DC resistance	70Ω
turns	1000
Relative permeability	1329

The second method is the use of smaller inductors in the catheter's interior. For these sensors, the OD of the coils ranges from around 0.4mm to about 1.5mm,Figure 4-3. For these coils 50AWG to 60AWG wire is common. There has been some work to make lithographic coils [42], [43], though no market applications or research in this area is known for EMT. To compensate for their smaller size, these coils often will have a longer length and a high permeable core. For a single axis the design, a single inductor in the range or 2mm to 15mm can work with varying degrees of accuracy. To get 6DOF two primary options exist. The first is what BSW and Super Dimension (SD) show in [15], [39] where three or more small coils are used. The SD design has six coils, two sets of orthogonal coils, which makes it longer and more complex to make, but could allow for gradiometric measurements. The second design involves orienting two coils such that there can is an angle between them, forming an "X" design [36]. A set amount of angle appears to be required, though as the angle between the sensors decreases so does the ability to resolve the 6th degree of freedom. The primary issue with using these sensors is their length, which causes a couple problems. The first is that the longer coils limit the flexibility of the catheter as the coils need to be rigidly placed to prevent breakage and maintain the calibration/position of the sensor in the catheter. The second issue is that the magnetic field measured by the sensor is averaged over the length of the sensors, which can induce

displacement errors for longer sensors.

Even with the issues mentioned, there are reasons inductors are the most common sensors in EMT. The primary reason is SNR. The intrinsic noise of an inductor is typically its thermal noise due to wire resistance. The microwire does induce higher resistance, though inductors still typically have a resistance below 200Ω. For a 100Ω case with a 100Hz bandwidth at 25C, this would lead to a thermal noise of only 13μV. The low resistance, as noted before, helps with minimizing noise coupling on the long leads used in catheters. The sensitivity of EMT sensors can also be increased simply by using a higher frequency to some extent (I.E., Figure 4-2). Both cored, and hollow cored inductors can have excellent linearity. For the hollow core inductors, the linearity is primarily determined by the LRC characteristics of the circuit, whereas for a cored inductor, it may be more influenced by the ferromagnetic properties of the material. Lastly, the manufacturability of inductors is not trivial though industrial resources exist that micro wind coils, and for the researcher, it is possible to wind a moderately small sensor by hand allowing lab-scale R&D.

4.5. AAO Inductor development

In order to overcome some of the challenges of creating a small sensor for catheter applications, fabrication of two primary inductive options were explored. The driving concept behind both options was the use of AAO as a fabrication matrix that could allow for high aspect ratio structures hard to achieve with traditional lithography. The first was the development of a microfabricated solenoid style inductor utilizing etched AAO to allow mass production of high aspect ratio solenoid with conductor diameter 10 μm (Figure 4-4) or less. The second was a planar inductor that utilized the high aspect ratio of the AAO etching along with nanowires as a method of creating a high aspect ratio core in a flat microfabricated package (Figure 4-4. For both coil concepts, the development of a simple inductor could additionally be a stepping stone towards more complex inductive sensors and circuit elements such as a fluxgate style sensor or even a transformer though neither was pursued in the work below.

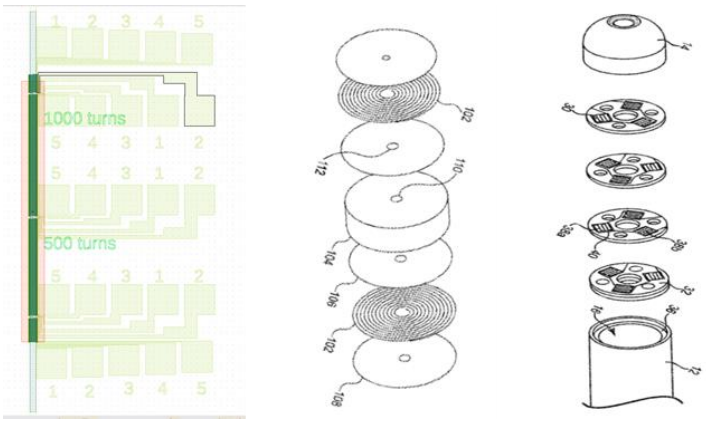

Figure 4-4. Left, image of lithographic solenoid mask. Middle and Right, AAO inductor concepts [44],[45].

4.6. AAO Planar coil design

The AAO Planar coil concept was to use the high aspect ratio pores of the AAO to create a core with high permeability normal to the plane of the coil. This concept could be carried out in two ways for a high aspect ratio planar coil. By using AAO, nanowires could be electroplated into the pores between the coil turns (Figure 4-4, Left). Since the porous AAO can have pore diameters in the range of 30 nm to 200 nm, this would lead to aspect ratios of 500 to 3000 for 100 µm thick AAO templates. The second method would be to plate a high permeability material directly between the turns, which could lead to various aspect ratios depending on the thickness and pitch of the turns (Figure 4-4, Right).

One additional advantage of using the AAO matrix for the planar coil is the ability to lower the overall coil resistance while keeping a tight pitch and maximizing flux area. The typical approach to planar coils uses traditional lithography or potentially LIGA. To minimize the coil's resistance, the designer can use fewer turns, which lowers the inductance or wider/thicker turns, which increases the planar area. Using AAO's high aspect ratio, a 100 µm wide by 1 µm thick turn can essentially be stood on edge, allowing a low resistance high turn pitch coil. Similarly, the narrow turns allow more efficient use of the turns since densely packing turns at the periphery induces a larger coil area.

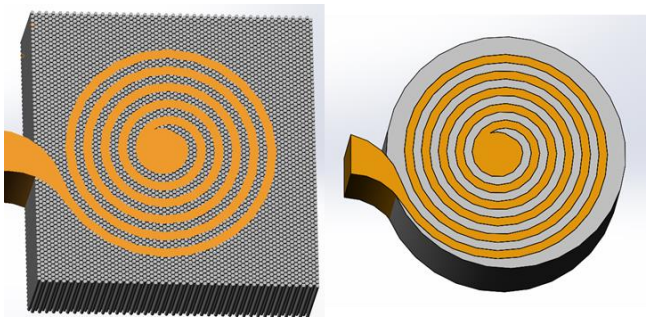

Figure 4-5. Left, AAO planar coil with plated wires. Right, AAO planer coil with plated gaps.

For planar coil development, the first step in the process was to test lithography limits on a Si wafer before moving to AAO. For this, a test mask was made with planar coils of various sizes that may be used within a catheter application. Figure 2-1shows the mask and wafer with lithography on it. In the design, four different coil designs were drawn and then made using five different variants of turn with and pitch (Table 4-3. Planar coil test mask design matrix. Table 4-3). Using standard lithography designs down to 1µm wide with a 2 µm pitch were able to be lithographically defined using the test mask (Figure 4-6, Right).

Table 4-3. Planar coil test mask design matrix.

Size 1: W≤ 250µm L ≤ 4000µm												
Design	**circle**			**oval**			**square**			**Rect**		
T = Trace width [µm]; P = Trace Pitch [µm]; ## = number of turns												
	T	P	##	T	P	##	T	P	##	T	P	##
#1	1	2	49	1	2	49	1	2	49	1	2	49
#2	2	3	30	2	3	30	2	3	30	2	3	30
#3	2	4	25	2	4	25	2	4	25	2	4	25
#4	5	6	15	5	6	15	5	6	15	5	6	15
#5	5	7	14	5	7	14	5	7	14	5	7	14
#6	5	10	9	5	10	9	5	10	9	5	10	9
#7	10	11	9	10	11	9	10	11	9	10	11	9
#8	10	12	8	10	12	8	10	12	8	10	12	8
#9	10	15	7	10	15	7	10	15	7	10	15	7

#10	10	20	5	10	20	5	10	20	5	10	20	5

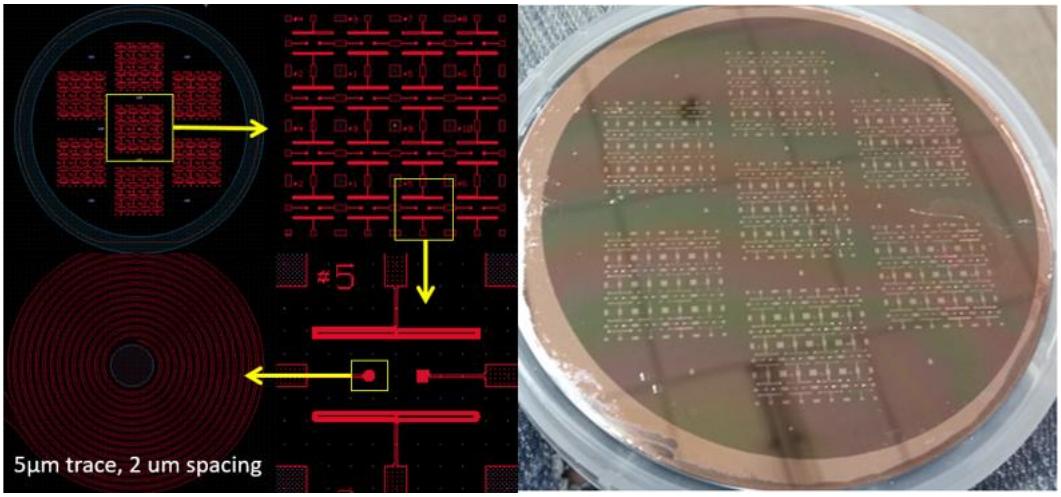

Figure 4-6. Planar coil mask, and resist coated wafer.

The next step was to test the deposition on the wafer. To do this two approaches were taken. The first approach involved plating in a simple copper sulfate bath consisting of 18g/l of $CuSO_4$ and using rotation and pulsed deposition to try and achieve conformal coverage. To do this, a custom RCE electrode fixture was developed which would contact the wafer on the side and seal on the photoresist surface. Figure 4-7shows the outcome of the plating. While all the coils did plate, overplating caused the coils to short out and underplating caused shorts. Attempts to polish the over-plated coils were attempted, but the coils often scraped off before the could be made useful.

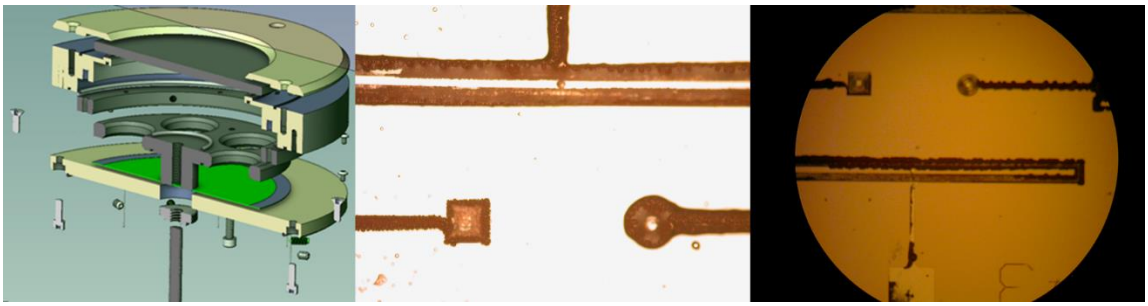

Figure 4-7. Left, RCE wafer fixture. Center and Right, examples of over and underplating planar coils.

The two primary issues in the plating design were due to lithographic feature aspect ratios and the plating conditions. First, the plating bath conditions were not optimized.

There is significant work that has gone into developing commercial Cu plating conditions that were not available during the plating attempts. Working with Silicon Valley Wafer Plating, future plating attempts were performed by them using their proprietary conditions. The second problem of different aspect ratio structures in close proximity to each other is shown in Figure 4-8. The aspect ratio of the coils center tap and exiting trace on the original are significantly larger than the trace width of the turns. This leads to a condition where the large aspect ratio structure pulls the Cu from solution and away from the other turns leading to pore deposition. By modifying the center tap and exit trace to have the same aspect ratio that resolves the issue.

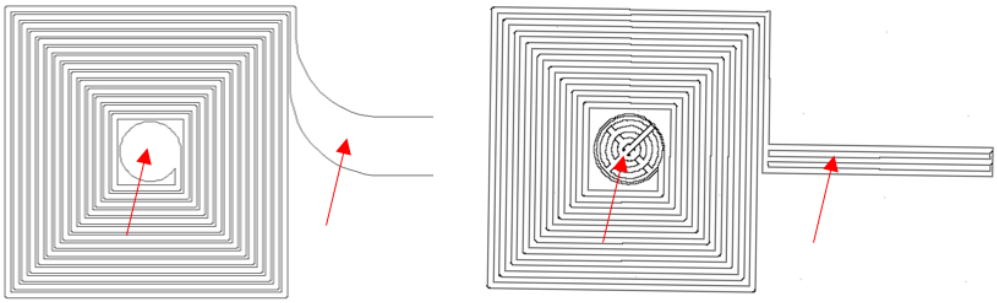

Figure 4-8. Left, an example of the original coil design aspect ratio, showing coil 5. Right, updated coil design with equivalent aspect ratios throughout the structure.

The second attempt at plating the coils was performed by Silicon Valley Wafer Plating. The new coil designs were plated using a rotating counter-electrode for stirring, along with their proprietary plating conditions (Figure 4-9). The coils showed even deposition across the wafer though continuity could not be checked until the contacts where sputtered. With sputtered contacts, most coils appeared connected and had resistance values in the 10Ω to 100Ω range. Since these coils were only on the order of a few μm tall, the resistance is significantly higher than an AAO planar coil with 100μm tall turns would be. Assuming that each tun is only in the 3μm to 5μm tall range, a 20x to 0x resistance decrease could be expected along with a 4x to 6x decrease in thermal noise.

Further development of the planar coils required the development of AAO etching. The AAO etching process is discussed in section 4.8. The final development of the planar coil was never pursued due to issues presented in section 4.8.

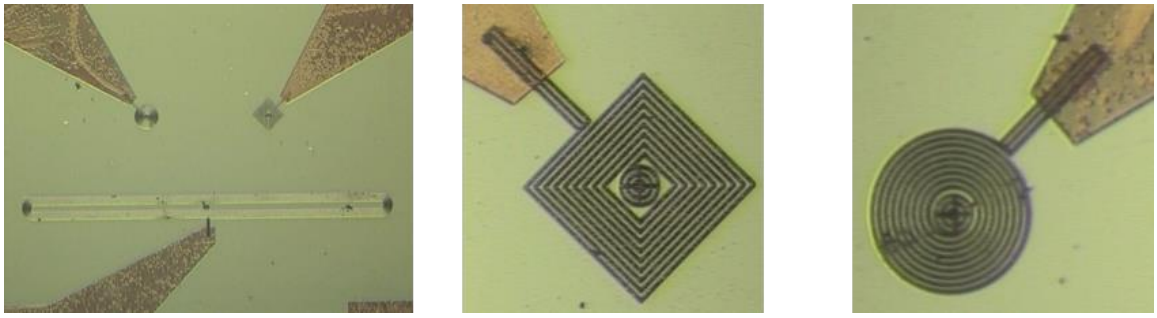

Figure 4-9. Plated planar coil, design 6, on silicon wafer with contacts deposited. Left, all three coil designs. Middle, square design close up. Right, circular design close up.

4.7. Solenoid coil design

For the solenoid style AAO based lithographic coil, an initial design and associated masks were developed. The dimensions of the vias were based on AAO test etching carried out in section 4.8. The mask was designed for a 10mm square AAO sample and is shown in Figure 4-10. The design allows for the deposition of up to 1000 potential turns (2000 vias) using only the first layer of vias. The vias were 10 µm with 10 µm spacing. Extra contact points were added to allow for measurement at the 100, 500, 900, and 1000 turn points within the coil. The complete design, if built, would allow for a 2mm coil with up to 5000 turns and the addition of a core.

4.8. AAO etching process development

In order to use AAO as an electroplating template for high aspect ratio structures, a suitable fabrication process had to be established. Initially, no such work was found, though soon after starting a relevant paper [46] was found which demonstrated AAO etching, though few details of the process were given. While the etching procedure was discussed, many details of the process such as fabrication, handling, lithographic parameters, and more needed to be worked out in order to determine feasibility for a manufacturable process. For the development of the AAO etching process, the solenoid coil design was primarily pursued. A manufacturing process road map for the development of the solenoid design is shown in Figure 4-11. The map is a fifteen-step process that covers the general steps though more detail could easily be added to this for a full production process tree.

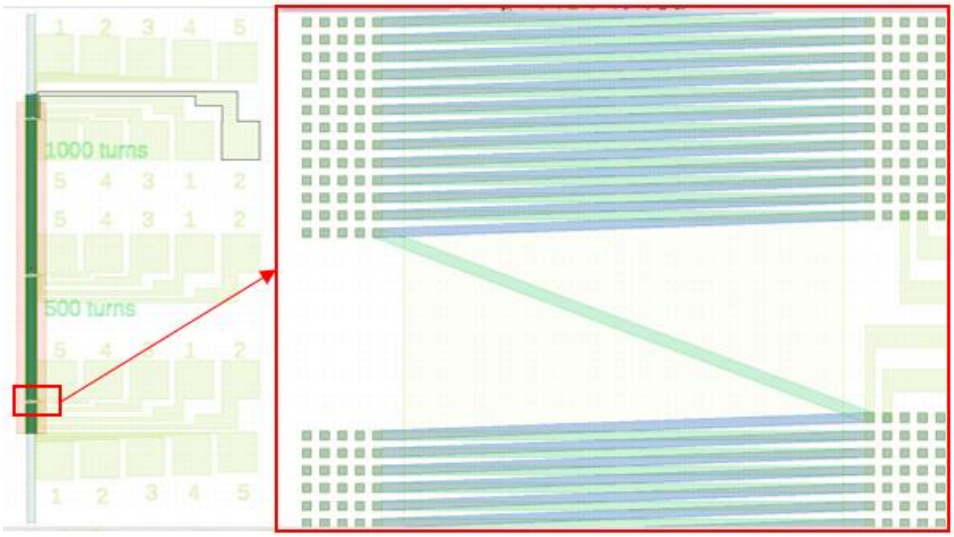

Figure 4-10. AAO coil mask design.

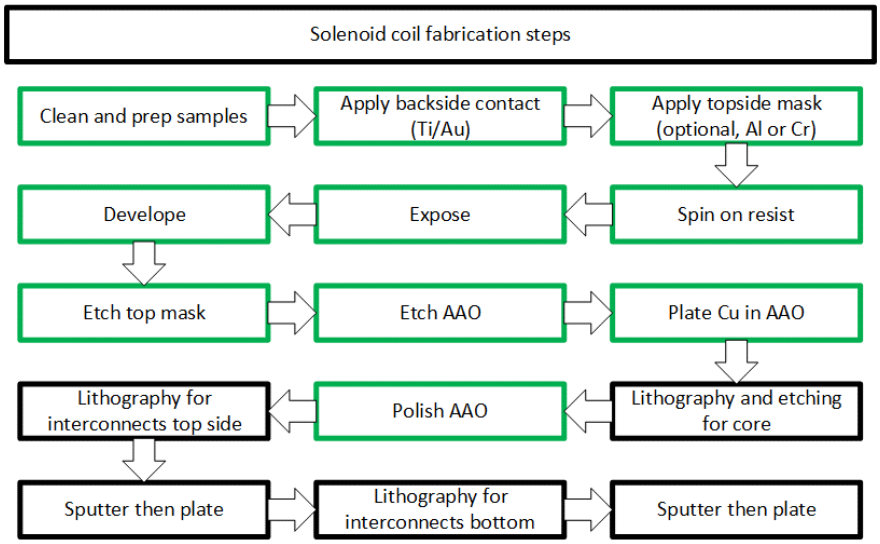

Figure 4-11. Road map for AAO solenoid coil development

The first step in the fabrication process was the sourcing of the AAO. For an industrial process, a standard wafer size such as a 150 mm wafer would likely be used, and so a 150 mm AAO wafer was developed with Nanomotif LLC. During wafer development, 10 mm square samples from Synkera Technologies Inc. with 30 nm to 100 nm pore size were used. As the work progressed, it was found that the AAO surface was a limiting factor in lithographic resolution. Working with Nanomotif LLC, the 150 mm AAO wafer was

fabricated using 0.9999 purity Al foil that had been polished prior to anodization to minimize surface defects in the end product. The AAO was fabricated using the two-step anodization process in an Oxalic bath to achieve 55nm pores with a thickness of ~80µm. Additionally, in order to aid large scale fabrication, 150mm diameter wafers with an outer Al ring were developed that allowed easier handling of the very fragile wafers (Figure 4-12, Left). Due to the cost of such a wafer (~$1.5K), smaller samples were cut from the 150 mm sample for continued concept development.

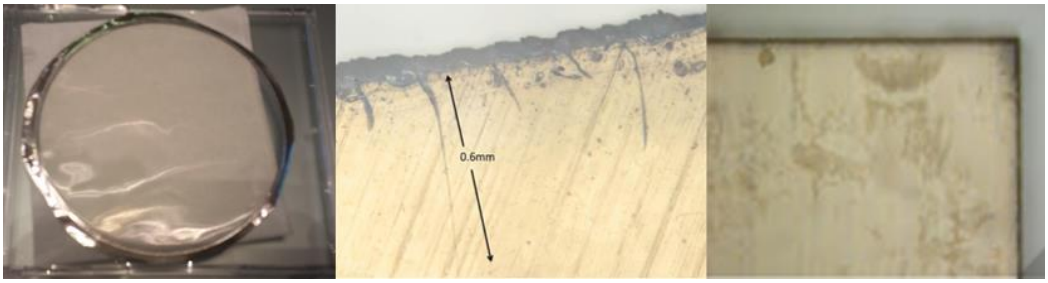

Figure 4-12. Left, 150 mm AAo wafer design. Middle, CO_2 cut AAO with cracks. Right, Femtosecond laser-cut AAO free from cracks.

In order to fabricate 10mm square samples from the 150 mm wafer, an efficient method of cutting had to be developed. Initial cutting was performed using a CO2 laser. Test with the CO2 laser showed that it was effective in cutting AAO, though it caused a significant amount craking around the periphery of the sample (Figure 4-12, middle). The size of the cracks was small, though during processing it may serve as a nucleation path for further cracking or a leakage pathway during etching and electrodeposition. Test with a 355nm laser and a femto second laser (raydiance Inc.) showed that both lasers were capable of producing crack-free cuts. Between the femto laser and the 355nm laser, the fempto showed less fouling of the sample and was used for all subsequent cutting (Figure 4-12, Right). The optimized cutting values are given in Table 4-4. In later processing, a layer of photoresist was spun onto both sides prior to cutting to aid in minimizing surface fouling.

Table 4-4. Optimized cutting parameters

Laser type	femtosecond
Laser manufacturer	Raydiance Inc
Power	10 watt
Frequency	12.5 kHz
Pulse energy	50 uj
Assist gas	10 PSI Nitrogen or less
Feed Rate	.01 IPS
On/Off dwell	0.5 sec

Applying the back contact was the next step to be developed. For the back contact, 150nm Ti / 200nm Au was applied via PVD. Initially, the samples were held in place with high temp polyimide tape to a Si wafer for deposition. Issues with foreign matter during lithography and cracking of AAO during removal of the tape lead to the development of a fixture for the 10 mm samples. Shown in Figure 4-13 is the CAD model of the fixture. The two-piece design with tapered pockets and 150mm wafer size allowed the sample to fit into standard equipment and conformal coverage of 18 AAO wafer without risk of cracking or added contamination.

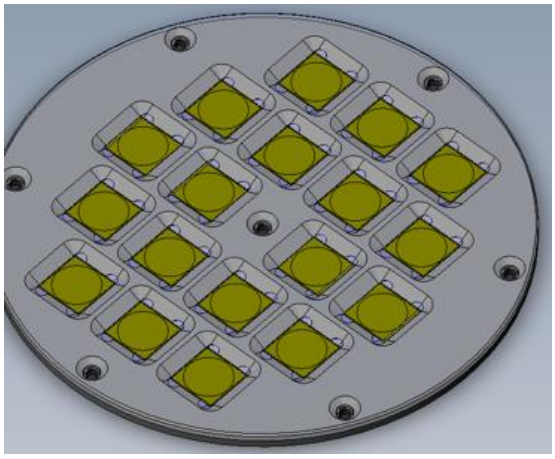

Figure 4-13. 10mm square AAO sputtering fixture.

Lithography on top of the AAO was the next process to be developed. For the Lithography, a number of steps had to be developed in order to achieve good resolution of the features. In order to use photoresist spinners with the 10 mm AAO samples, a special

fixture had to be created. Figure 4-14 shows the AAO lithography fixture. The fixture mimics a 150 mm wafer, which allows it to be used in standard processing equipment. In the middle there is an inset with 200 µm holes to allow vacuum to hold the sample in place. Small reliefs in the corners were added to aid in removing the AAO sample with tweezers.

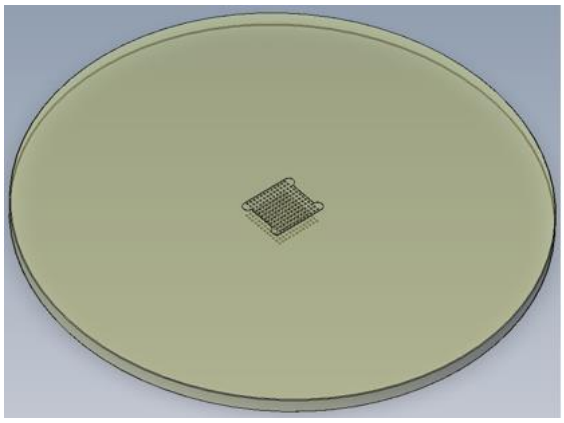

Figure 4-14. 10mm AAO lithography fixture.

To test out the limits of lithography on AAO for the solenoid and planar coils, a test mask was designed.

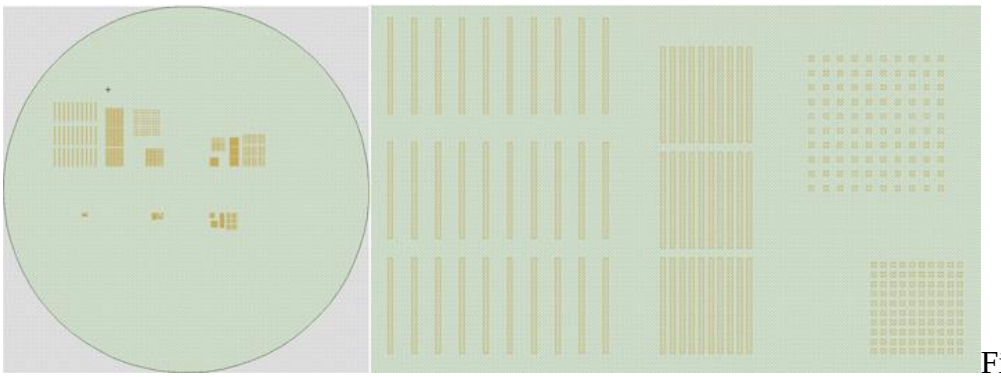

Figure 4-15 shows the full design along with a close up of the pattern, which is repeated five times. For the five designs, a primary feature size of 20µm, 10 µm, 5 µm, 2 µm, and 1 µm were used. The tight square pattern consisted of a 1:1 ratio of feature size to gap. The expanded square consisted of a 1:2 feature to gap ratio. Similarly, the tight rectangular structure had a 1:1 ratio of width to gap, while the width to length ratio was 1:20. For the wide rectangles the gap was 4x the feature width. The squares were designed to approximate the vias used for turns in the solenoid coil, whereas the rectangles were there to represent either a rectangular via for the solenoid or to help approximate the etching process on long narrow structures

as would be required for the planar coil.

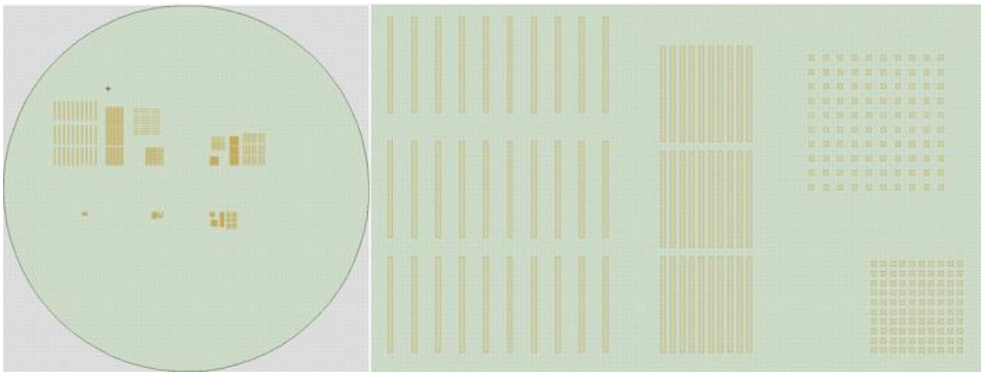

Figure 4-15. AAO etching test mask design.

During the development of the lithography, various aspects of the AAO surface had to be optimized to attain high resolution. The first attempts at lithography were performed on the bare AAO surface. Resist was spun onto the AAO and then developed using the test mask. Some of the larger 10 µm and 20 µm structure would resolve though the smaller ones did not. The next attempts involved using an Al coated pore such as used in [46]. For these samples, 150nm of Al was coated onto the AAO using the same fixture as for the back contact. The Al allowed to AAO to have a more reflective and smoother surface, which allowed for finer lithography. While the Al did aid in exposing the lithography, the developer was found to cause some lifting of the Al. Additionally, little "mouse bites" in the lithography occurred as well. To help, a surface cleaning step was introduced using a plasma cleaner. The reflectivity of the surface was then further enhanced using a Cr layer instead of the Al. Lastly, it was found that the backside of the AAO was typically smoother than the top and thus served as a better lithography surface. With these process steps, lithographic features down to the 5 µm range were able to easily be resolved, while the 2 µm and 1 µm features could be resolved but with less repeatability.

After lithography, a two-step etch process was carried out. The first step was the removal of the Al or Cr layer. The etching was carried out with an Al etchant as described in [46] or using Cr125 etchant for the Chrome layer (Figure 4-16). Following removal of the metal, the AAO could be etched using 3% phosphoric acid. The samples would be placed in a sonicator and allowed to etch for up to 8 hrs. Figure 4-17 shows that the square

features and 1:4 ratio rectangle feature etched well, whereas the 1:1 ratio rectangles would typically break. The breakage of these features was thought to be primarily due to surface tension as the liquid would evaporate.

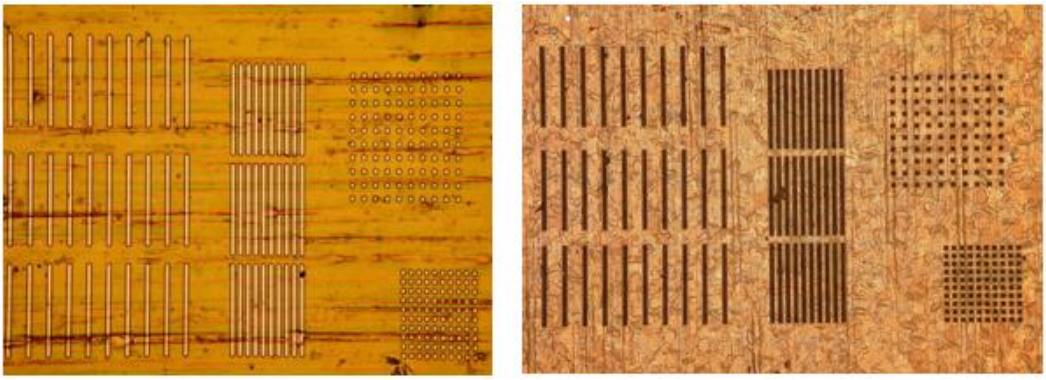

Figure 4-16. Left, AAO with lithography on top of Cr. Right, Lithography on AAO wi with Cr etched away.

Figure 4-17. Various pictures of etched AAO

Based on the etching test mask results, it was determined that the process could move towards coil fabrication. For the planar coil mask of Figure 4-6 it was decided not to pursue the design due to the etching test mask results. The etch test mask showed that the

long high aspect structures with a tight pitch were likely to fail the etch process. Further concepts of how to improve this via stress relief by annealing or stiffening the template via ALD filling of the pore not intended for etching were considered though not pursued. For the solenoid coil mask design, Figure 4-10, a microscope image of a large section of etched AAO is shown in Figure 4-18 Left. It can be seen that the lithography and etching appear to have worked, though a zoomed-in view is needed. In the middle of Figure 4-18, the vias appear to be well-formed and with only some minor defects occurring at the corners of the squares. An SEM image of a single pore shows a well etch 10:1 ratio structure.

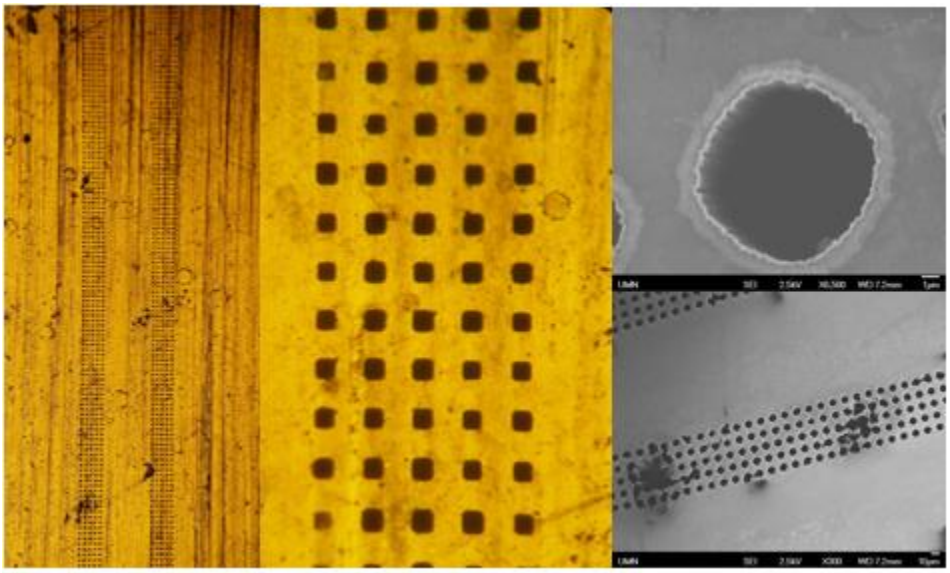

Figure 4-18. Example of etched solenoid coil design.

An SEM view of another section (Figure 4-18, Lower Right) shows a spot where etching broke the line between two or more pillars creating a large defect. A defect of this nature is a significant issue for coil fabrication and function. With a defect like this, the plating of the coil would likely be uneven and create a large blob of copper during deposition. This would effectively choke out other pillars from growing and leave opens in a finished coil. Similarly, connected pillars would cause shorts in the coil structure if fully developed. Etching using different AAO etchant concentrations, temps and times were used in an effort to minimize breakthrough of the vias, though only local areas could be controlled.

4.9. Conclusions

The goal of the experimentation was to determine if etched AAO could feasibly be used as a method of developing high aspect ratio coils. By developing a repeatable process, the ability to form lithographic features on AAO with dimensions down to 1 μm was demonstrated. Etching of 80:1 vias without the complex tooling associated with LIGA was also demonstrated. This process could be used with thicker AAO and potentially allow 200:1 or higher aspect ratios surpassing the capabilities of LIGA.

Further development of the process is needed in order to make this a manufacturable process. Adding process steps such as annealing of the initial foil could help to eliminate defects in the AAO, which may be part of the cause of pore etching. Similarly, Annealing of the AAO may also relieve some of the stress in the film and help to reduce how brittle it is and allow fabrication of long narrow structures such as those needed for the planar coils. Additional mechanical polishing of the Al foil using a method such as a parallel plate polisher to remove all traces of rolling would also aid in creating a better surface for lithography and fewer defects in the end product. Other processes such as ALD into the pores not being deposited, could also lead to better features. While the research shown advances the development of high aspect ratio structures using AAO, further development should be pursed if it is to become an industrial process.

5. FLOW SENSOR

5.1. Intro

Advances in sensor technology has increased the quality of life, health, and productivity of our world. In recent years, an increasing number of researchers have been looking to nature for inspiration. In biomimetics, researchers try to recreate biological structures typically for one of two reasons. The first is to better understand how the biological structure or device functions. The second is to mimic the biological function for use as a device. Often the research can pose a dual purpose in first elucidating the biological function and then translating it into a functional design. Recent examples of such include the Gecko robot [47] which mimics the gecko's foot structure and biomimetic cilia for

acoustic sensing which mimic stereocilia in the human ear [48].

5.1.1. Biomimetic Cilia

Cilia, in very general terms, are hair-like projections that extend from an organism's body to be used for a variety of functions. Often, as in the case of micro-organisms, cilia are used to create propulsion through liquids as the micro-organisms move about in search of nutrients [49]. Cilia and circa on the legs of crickets and other insects are examples of hair-like projections in nature being used to sense the flow of air. In another sensor role, cilia are used to sense vibrations as in the human inner ear where “stereocilia” sense the vibrations due to sound waves. These vibrations are then converted to an electrical signal which our brains perceive as sound. In this paper, two sensors are designed and fabricated to mimic the flow-sensing and vibration-sensing functions of cilia.

5.1.2. Flow Sensing

Cilia are ubiquitous in nature for sensing the flow of both liquids and gases. Given the large role of cilia in the microfluidics of nature, it is likely that cilia like structures may be able to play a substantial role within the relatively new field of medical microfluidics.

In order for microfluidics to become viable in a variety of industrial processes, chips are needed that can perform unique functions such as polymerase chain reaction (PCR), analyte detection, analyte separation, and a variety of other functions. However, the flow of the fluids within the device also needs to be controlled and monitored to ensure that the data obtained is reliable and accurate.

There are a variety of flow-sensing devices that have been documented in the literature and used industrially. These devices use different physical phenomena including heat transfer [50]–[52], optics [53], [54], impedance [55], cantilevers [56], [57] and Coriolis [58]. Of these methods, heat transfer and optics are the most prevalent. Although capable of sensing flow, each of these two methods suffers from limitations that are overcome in the sensors presented here. For the heat transfer (PCR) sensors, the readings can be easily affected by variations in temperature [59]. Thus, complex insulation of the

sensor is required to keep temperature constant. Eliminating temperature sensitivity will be especially important in developing nations where many envision microfluidics being useful. Lack of environmental controls may also affect the readings. Optical devices, on the other hand, often require costly optics or complex apparati that are impractical for compact, disposable systems [60]. Additionally, both types of systems can require significant power usage, which may limit their usefulness in portable, energy efficient devices.

The cilia-inspired flow sensor described here overcome many of these challenges in simple and robust packages that can take advantage of off-the-shelf parts. The device uses arrays of nanowires that are suspended in micro-channels, which are then placed on top of giant magnetoresistance (GMR) sensors. The design is robust to vibration and temperature using only micro-Watts of power. The device also does not need optics or to be optically clear.

5.1.3. Vibration Sensing

Vibration is also an area where biomimetic cilia can advance the ability to sense. Currently, there are few options for sensors in the 0.1–30 Hz range, especially if the application requires a very small, low-power sensor [61]. For example, during an earthquake, a nanoscale energy harvester could power-on a nanoscale vibration sensor. After recording the seismic data, the vibration sensor would switch on a structural sensor to monitor building health. The system would then be in sleep mode until next needed. The nanowires presented here could have many roles within the system described, but here we present preliminary data on their performance as vibration sensors.

5.2. Fabrication

5.2.1. Biomimetic Cilia Array

To mimic an array of cilia, an array of Co nanowires was fabricated using the process shown in Figure 5-1. For fabrication of nanowire arrays, templates of anodic aluminum oxide (AAO) were first made by anodizing Al foil (0.25 mm, Alpha Aesar 99.998%). The foil was first electropolished at 18 V for 5 min in a perchloric acid bath

(Figure 5-1 (a)). It was then anodized for 12 hrs at 40 V in an oxalic acid solution (Figure 5-1 (b)). The resulting oxide was then dissolved with phosphoric-chromic acid at 60°C for 45 min to expose the Al surface (Figure 5-1 (c)). At this point, the Al surface was nanostructured from the oxide formation. It is worth noting that nanoimprinting can also be used to create a similar nanostructure without the 12 hrs first anodization [62]. The nanostructured Al was then anodized for a second time, using the same anodization parameters as the first anodization in order to obtain an array of columnar nanopores with homogeneous diameters and interpore spacings (Figure 5-1 (d)).

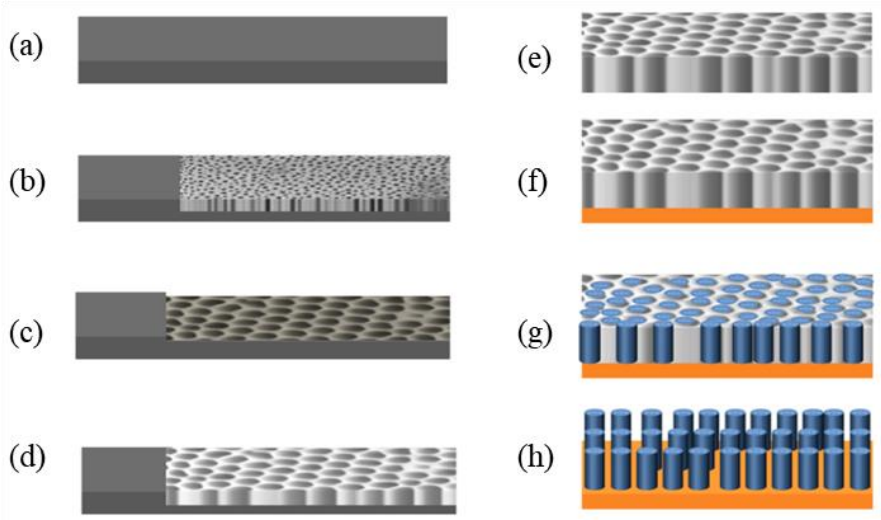

Figure 5-1. Fabrication of biomimetic cilia. (a) electropolished 99.998% aluminum foil. (b) Al foil with oxide after anodizing for 12 hr. (c) Removal of oxide to expose template surface. (d) Second, anodization to grow ordered pores from the template. (e) Oxide template is released by etching Al with HgCL2 or CuCl2. (f) Copper contacts are sputtered onto template. (g) Co wires are electrodeposited into template. (h) Oxide is etched away to expose nanowires that mimic cilia.

Following the second anodization, the pores were chemically removed from the remaining Al foil (Figure 5-1 (e)), and contacts sputtered (Figure 5-1 (f)). For this, the anodized foil was placed into mercuric chloride for 1.5 hrs. The AAO barrier layer (foil side) was then floated on top of 5% phosphoric acid for 3 hrs to remove the barrier layer. Next, the pore diameters were widened from 40 nm to 70 nm by submerging the sample in the same acid for 30 min. Finally, the AAO membrane was sputter-coated with 10 nm of Ti for adhesion and 300 nm Cu to make sure the pores were closed with a planar electrical contact that could later be used as a back contact for electrodeposition. With the contacts

made, the sample was ready for electrodeposition of the nanowires. The Cu contact side of the AAO was placed onto a piece of copper tape (3 M part number 1181 Tape) to act as a conductive interface between the power supply and the AAO back contact. Acrylic paint was applied to all areas of the copper tape and Cu contact where electrodeposition was undesirable. The AAO attached to copper tape was then used as the cathode. To complete the electrodeposition cell, a stainless steel mesh anode was used along with an Ag/AgCl reference electrode in a 1.0 M cobalt sulfate solution. A potential of 1.0 V was applied to the cell for 20 min to obtain 50 μm-long nanowires inside the 70 nm diameter nanopores.

Before the nanowire arrays could be placed into channels or onto GMR sensors, the large arrays were cut to size. For this, the array was mounted to a silicon wafer with crystal bond (Ted Pella Inc.). The wafer was then placed into a wafer saw where pieces could be cut to the desired dimension.

5.2.2. Flow Sensors

GMR sensors (DBS Proto2) and fluidics (Mold 2011-11) from Diagnostic Biosensors LLC. were used, shown in Fig. 2. The sensors were mounted to a flexible printed circuit board along with wire connectors for easy measurement of the sensor in a research setting. A custom microfluidic cover was designed using computer software to accept the nanowire array. The fluidics were stamped and machined to size by Diagnostic BioSensors LLC. The fluidic channels were left off of the GMR sensor so that the nanowire array could be added before assembly. For the sake of our experiment, we choose to use the microfluidic cover with tubes directly attached (Figure 5-2, bottom right insert), as opposed to the whole fluidic assembly (Fig. 2, top left insert) for ease of disassembly and reassembly required by the research nature of the task.

Prior to the assembly of the microfluidic cover onto the GMR sensor, a nanowire array (still in the oxide matrix) was glued into the channel of the microfluidic cover. The cover was then submerged in phosphoric chromic acid for 2 hrs to remove the oxide completely. After being lightly rinsed and dried, the cover was glued on top of the GMR sensor, and the fabrication was complete (Figure 5-2bottom).

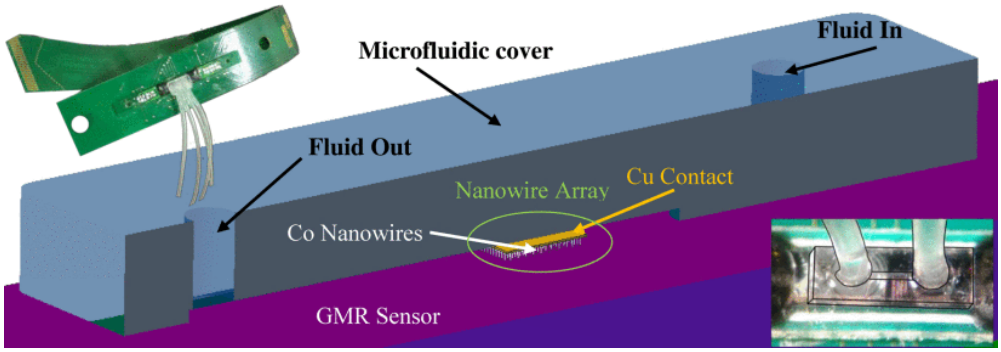

Figure 5-2. CAD model of the sensor. The top left insert shows complete sensor assembly from Diagnostic Biosensors. The bottom-right inset shows the reference sensor as tested.

5.2.3. Vibration Sensors

The vibration sensor was composed of two main components. The first was a GMR sensor (NVE AA-005) purchased from Nonvolatile Electronics (NVE) of Eden Praire, MN. The second was the nanowire array, which was fabricated as previously described. The GMR sensor was mounted to a circuit board, and leads were attached. A rectangle of nanowire array was then placed on top of the GMR sensor, and the ensemble was encapsulated in polyacrylamide with one edge uncoated. The whole assembly was then submerged in phosphoric-chromic acid for 3 hours, lightly rinsed and air-dried overnight. The final assembly of the sensor is shown in Figure 5-3.

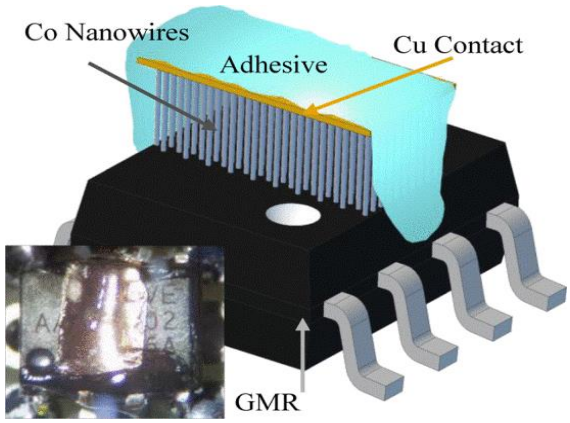

Figure 5-3. Vibration sensor assembly. The sensor is an NVE AA004-02. The copper is the backside of the nanowire array.

5.3. Sensor Actuation

The general mechanism of the sensors presented here can best be described as an array of magnetic cantilevers suspended above a GMR sensor that has in-plane sensitivity (Figure 5-4). The movement of the cantilevers relative to the GMR sensor was caused either by a flowing fluid or by momentum transfer from the vibrations.

A nanowire array compared with a single cantilever with the same volume will have significantly lower spring constant allowing deflection to occur. Additionally, the nanowire shape introduces a high level of magnetic shape anisotropy that would not be had in the single cantilever. The large aspect ratio (diameter=70 nm, length=50 μm) gives a natural resonant frequency near 1 kHz. This is well above the frequencies used here to enable linear frequency response.

The natural magnetic shape anisotropy of the nanowires enables a strong magnetic field to be detected. The magnetic field emerging from the end of a cylinder that is magnetized along its axis is given by

$$B(m, r, \theta) = \frac{\mu_0 m}{4\pi r^3}\sqrt{1 + 3\,sin^2\,\theta} \qquad (6\text{-}1)$$

where μ_0 is the permeability constant, m, the magnetic moment, r distance from the wire to the sensor, and θ is the angle between the nanowire and the surface of the GMR sensor (Figure 5-4(a)). When the nanowire array has no net force acting on it, the nanowires are perpendicular to the plane of the sensor, and the net magnetic field is then perpendicular to the plane of the GMR sensor. Since the sensor used in this design is polarized in-plane the effective field on the GMR element is near zero. The nanowires act as nano-cantilevers bending in response to an applied force. As the nanowires bend, the component of the magnetic field which was initially perpendicular to the plane of the GMR element starts to decrease. At the same time, the magnitude of the parallel component starts to increase. As the force on the nanowire array increases, the bending of the nanowires exposes the GMR element to an increased parallel field and decreased perpendicular field. This parallel field is then sensed as a change in the GMR sensor's resistance.

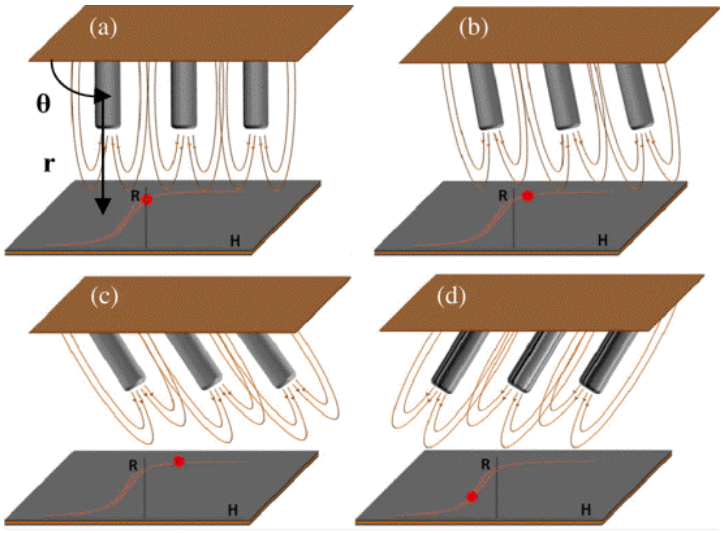

Figure 5-4. Actuation of flow and vibration sensor demonstrated using R versus H plot from the GMR sensor. (a) With no force, the nanowires are perpendicular to the GMR sensor. (b) As force is applied, the wires start to bend. (c) As the force is increased, the bending increases along with the component of field in-plane with the GMR sensor. (d) Force in the opposite direction.

5.3.1. Flow Sensors Testing

The flow sensors were tested by attaching them to a LabView data acquisition system, and a manual syringe pumped water through the microfluidic channel at rates varying approximately between 0.5 ml/min and 6 ml/min. The output of the GMR sensor was detected using a Wheatstone bridge circuit. The total resistance of the bridge was 140 Ω, and by using only 1 mA of current, the sensor was able to operate using only 140 μW of power.

First, a reference sensor was analyzed in which there was a microfluidic channel with no nanowire array. The results of the reference sensor are shown in Figure 5-5. The figure shows that the sensors had an output centered near 4.0 μV with a peak to peak amplitude of approximately 1.75 μV. The signal measured from this sensor is equivalent to the noise of the system under flowing fluid since no wires or other particles were in the fluid used.

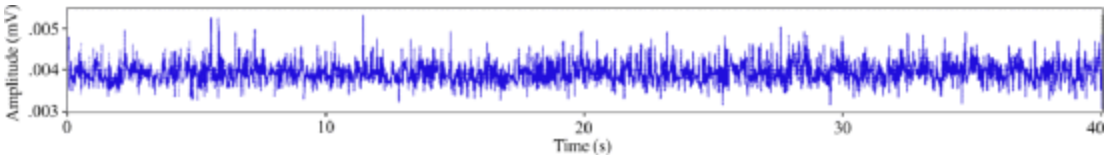

Figure 5-5. Output of reference sensor with pure water flowing. Data shows a signal which consists of 1.75 μV of noise since no magnetic particles are in the flow.

A sensor with a nanowire array was then tested using the same procedure as the reference. From Figure 5-6, it can be seen that a significant signal was produced. This signal contained only 400 nV of peak to peak noise obtained from measurements in Region I. This noise was less than that of the reference sensor because the field from the nanowires stabilized the GMR sensor. The maximum output achieved from the sensor under flowing water was 147 μV at 6 ml/min which was 22 μV greater than the base voltage in Figure 5-6. Therefore, sensitivity and SNR can be estimated as 3.67 μV per ml/min and 44, respectively.

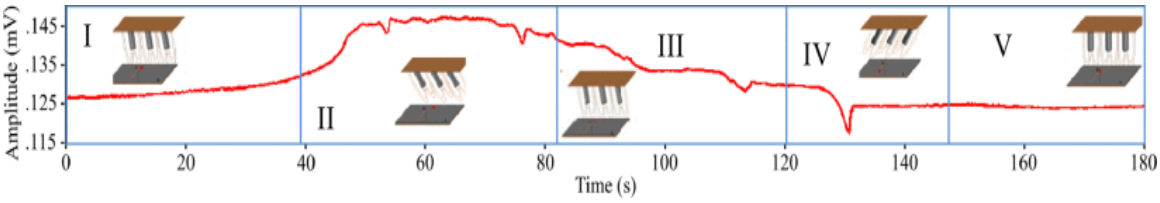

Figure 5-6. Output from flow sensor showing four regions. Region I shows an increase in voltage as the syringe pump pressure slowly increases. Region II shows the maximum voltage achieved using the syringe. III shows the output, and the pressure was slowly released. Region IV shows a backflow in the sensor. Region V shows the sensor going back to its base output as the flow is stopped.

The signal shown in Figure 5-6 shows four distinct regions related to four regions of the flow. In Region I, there was no pressure on the syringe, and 125 μV was measured as the background signal. Next, as the pressure was slowly increased, the signal also increased to 130 μV. In region II, the syringe was pressed to the maximum hydrostatic pressure possible for the pump, which produced a 6 ml/min flow rate. At this flow rate, a signal of 148 μV was measured. Oscillations in the signal were due to slight releases in pressure of the syringe pump. This showed that the sensor was also responsive to small changes at high flow rates. In Region III, the pressure on the syringe was slowly decreased.

The signal subsequently decayed back to 125 μV, the same value as measured in region I. At the very end of region III, a minima is observed that goes below the zero applied pressure point of region I. This appears to be due to a temporary reverse of flow which occurred as the experiment came to a sudden halt and all of the pressure was released. Finally, region IV shows the response when the applied pressure returned to zero for an extended period of time. The voltage of the sensor returned to and remained at 125 μV, identical to where it started in region I.

The sensor tested needs further optimization, but flow parameters can be estimated based on the use of a hand syringe pump and the electrical readout from LabView. The noise level of the sensor with no external signal conditioning was 400 nV peak to peak. By taking 500 nV to be the minimum detectable change, the minimum detectable flow rate is 136 μl/min, according to our sensitivity estimates (3.67 μV per ml/min). This minimum flow rate corresponds to an estimated flow acceleration of 16 $\mu l/s^2$ (1.6 m/s^2).

5.4. Vibration Sensor testing

The vibration sensors were tested initially by observing the output of the GMR sensor in response to various mechanical stimuli. The sensor from the manufacturer was encased in a SOIC 8 package (Figure 5-3), which was mounted on a stiff breadboard and a stability jig. The jig was then physically manipulated, and sources of noise were eliminated until the GMR sensor was only sensitive to sideways jerking motions that mimicked the vibrations to be detected.

This preliminary packaging was then mounted to a shake table. The sensor was attached to the data acquisition system with all wires well secured. Next, the sensor was subjected to earthquake-like frequencies in the range of 1–5 Hz at an amplitude of 1.75 inches, which yields an acceleration of 1.78 m/s^2–143 m/s^2. The data from a sensor can be seen in Figure 5-7(a). To see the frequency response more clearly, a section of the data is expanded in Figure 5-7(b). In all cases, the dominant frequency of the vibration sensor was twice that of the shake table, which was expected since the GMR sensor did not distinguish between nanowires passing underneath it from the left or the right.

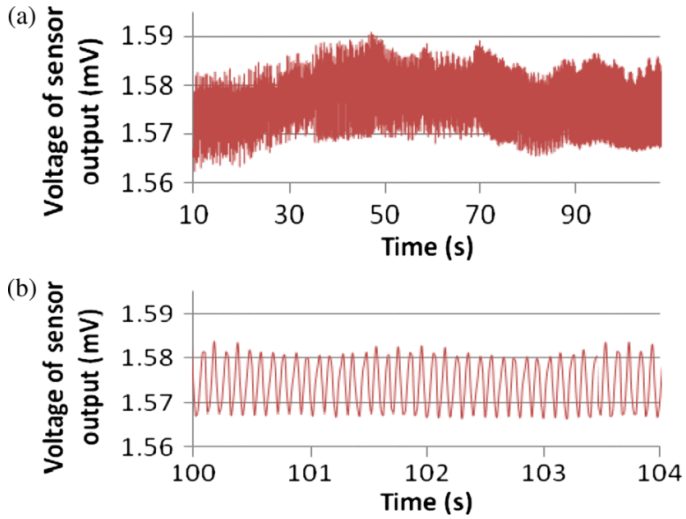

Figure 5-7. Output of vibration sensors on shake table (a) Output versus time for a series of different shake table frequencies (b) A section of data showing a 10 Hz signal from the table shaking at 5 Hz.

The spectral frequency was analyzed using Matlab. The dominance of the double frequency is apparent (the strong yellow line in Figure 5-8). The spectral frequency at 90 s is shown in the insert, which demonstrates the strong 2*f* response associated with the 4.5 Hz shake table vibration. Less powerful harmonics are also present in both plots. As the frequency was reduced below 2.5 Hz, the signal dissipated possibly due to the decrease in acceleration below 11 m/s^2, which can then be taken as the minimal detectable acceleration for this set of experiments. A reference sensor was also prepared here with a GMR sensor encapsulated in polyacrylamide, and packaged the same as the first, but without a nanowire array. This sensor only picked up a 1*f* frequency of the GMR sensor in response to the Earth's field. The double frequency measured by the sensor with nanowires vibrating back and forth with each excitation cycle is a specific response around which future sensors can be designed.

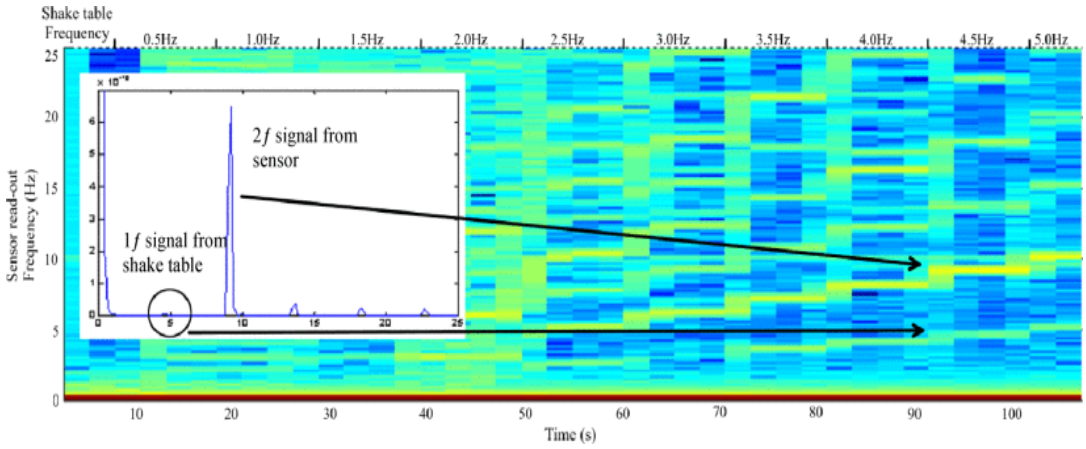

Figure 5-8. Spectral frequency analysis of a vibration sensor on a shake table at various frequency vibrations. The insert shows an FFT of data from the sensor when the shake table was at 4.5 Hz. Arrows from the FFT inset point to the corresponding spot in the spec

5.5. Conclusions

The biomimetic sensors presented here showed that magnetic nanowire arrays are capable of being used in various ways to sense environmental stimuli, much like biological cilia. The sensor designs are quite simple and can be integrated into larger systems for additional functionality. The flow sensors, using only microwatts of power, were able to sense fluid flow in the μl/min to ml/min range as a microvolt signal. The design had no external amplification or optimization, and continued design optimization can be used for flow measurements in other regimes. The vibration sensors prepared here indicated that cilia sensors produce a signature 2*f* signal at low frequencies (1–5 Hz).

6. Electroplated Galfenol For Contactless Torque Sensing

6.1. Intro

Rotary motion exists in nearly all machinery ranging from large scale windmills and diesel engines to drive shafts in cars and even to micro drills used within the vessels of human hearts. For better control of these devices, feedback is key; thus quality torque measurements are essential. Quality measurements are often achieved at the cost of large

size and poor efficiency, so engineering tradeoffs must be made in order to get products to market. The materials and measurements presented here are an effort to introduce new solutions that offer small sensors with high efficiency and reliability. $Fe_{1-x}Ga_x$ ($0.10<x<0.40$, a.k.a. Galfenol), is a sensing material that exhibits saturation magnetostriction of up to 400 ppm and has saturation magnetization values of ~1.7 T. Here we use inverse magnetostriction (the Villari effect) to demonstrate that electrodeposition of $Fe_{1-x}Ga_x$ directly onto shafts enables low-power, noncontact, directly-coupled torque/strain measurements. Specifically, direct deposition of Fe_{1-x}Gax films onto cylindrical shafts using rotating cylinder electrodes (RCE) is demonstrated for the first time, and a noncontact torque sensor is subsequently realized.

6.2. Background

6.2.1. Torque Sensors

Several commercial technologies currently exist for torque sensing, but the sensing material rarely has direct contact with the element being strained [63], [64]. Figure 6-1 shows three different styles of sensors, including a typical strain gauge (Figure 6-1, a) where the sensing material is grown on a specified substrate which is then adhered to the torque element [65]. The substrate, the adhesive, and alignment can all be sources of error in torque measurements. Additionally, these gauges require either direct contact via wires or slip rings, or indirect contact in which measurements are acquired via an inductive coupling resonant circuit on the shaft. Figure 6-1b shows a bulk sensing material adhered directly to the torque element [66]. Using this method, the properties of the adhesive will still impact the sensed torque. Figure 6-1c is an illustration of the proposed technological solution in this paper where the sensing material is deposited directly onto the element being measured. Similar solutions have been proposed in a number of patents and papers, but this is the first time the principle has been demonstrated with electrodeposited $Fe_{1-x}Ga_x$ [67]–[70]. Advantages such as facile manufacturability, good magneto-mechanical coupling, robust mechanical properties, and direct coupling make electroplated $Fe_{1-x}Ga_x$ a promising addition to the field of torque sensors.

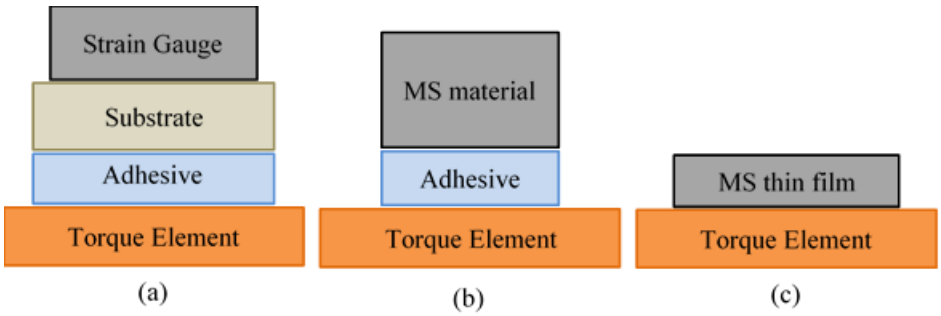

Figure 6-1. a) Typical layers in strain gauge-based torque sensor. b) Bulk MS materials adhered to a torque element. c) MS thin-film electroplated directly to torque element.

6.2.2. Magnetostrictive (MS) Materials

For direct coupling, there are a number of magnetostrictive (MS) materials that could be considered. Terfenol-D has a large MS constant (λ=1500 ppm), with a saturation magnetization value of B_s = ~1.0 T, but the material is brittle and would be difficult to electrodeposit due to the easy oxidation of soluble rare earths, such as terbium and dysprosium [71]. Co-Fe-O ferrites have been used by many researchers for MS sensors, and single crystals have been reported to have λ as large as 400 ppm with $M_s \approx 0.6$ T [72]–[74]. However, in film form, these oxides and various other MS ferrites are typically restricted to fabrication by planar vacuum-deposition techniques. To obtain ductile, conformal depositions on a cylindrical torque element, metals such as Ni, Co, or $Fe_{1-x}Ga_x$ could be electrodeposited. Ni and Co have low MS constants ($\lambda_{Ni} \approx$- 40 ppm, M_s= 0.6 T; $\lambda_{Co} \approx$ -18 ppm, M_s = 1.4 T), but single crystal $Fe_{1-x}Ga_x$ has λ up to 400 ppm with M_s = 1.7 T [4], [75]. Although electrodeposited $Fe_{1-x}Ga_x$ films only have λ = 100-200 ppm and M_s = 1.6 T, the truly unique capability of direct, conformal deposition onto torque elements makes them very promising as a new solution to the field of torque sensing, and a prototype device is demonstrated here [76].

6.2.3. Induced Anisotropy for Self Bias

A common design criterion in magnetic-based sensors is the need to align the primary magnetic axis of the sensor to take full advantage of the stimulus and sensing mechanisms. To do this, permanent magnets and/or electromagnets are often used, which add complexity, cost, and/or power losses [77]–[79]. Alternatively, magnetic bias can be induced by shape, coupling layers, and texture [66], [80], [81]. While these approaches can

be complex, the final device can be small with all components fully integrated. For example, Garshelis [68] coupled two rings with respect to each other after application of a field in order to maintain a bias direction. Raghunath [66] used patches of a textured rolled sheet with known magnetic easy axes orientations to achieve directionality. In this research, a simple substrate pretexturing process is introduced so that electrodeposited $Fe_{1-x}Ga_x$ films possess a well-defined magnetic anisotropy. While this pretexturing does not relieve the need for a bias magnet in the configuration used in this paper, the induced anisotropy adds directionality to the sensor which improves its response.

6.2.4. $Fe_{1-x}Ga_x$ Electrodeposition

Electrodeposition of $Fe_{1-x}Ga_x$ was first demonstrated by McGary and then later refined and characterized by Reddy and Estrine [76], [81]–[83]. In these works, uniform, high-quality films were deposited onto rotating disk electrodes (RDE), and the importance of boundary layer control was shown. To date, the electrodeposition parameters of $Fe_{1-x}Ga_x$ have only been defined for planar surfaces. In this work, rotating cylinder electrodes (RCE) are made to elucidate the mechanisms of boundary layer control on cylinders, which represent standard torque elements, such as shafts.

While RDE and RCE are very similar in principle, their fluid dynamics can be very different. The seminal work describing mass transfer to/from the RCE is credited to Eisenberg in 1954 where a custom RCE setup with varying electrode sizes and rotation rates were used to measure the dissolution of ferrocyanide under different hydrodynamic conditions [84]. As cited by Eisenberg, many authors had investigated mass transport at cylindrical electrodes, including some fundamental work by G.I. Taylor which describes how turbulence develops at a rotating cylinder and is now known as Taylor vortices [85]. While other work with the RCE continued, the next most prominent and well-cited comes from seminal work of D.R. Gabe in 1972 [86], [87]. In addition to this work, D.R. Gabe and many others have continued to study the RCE. The most recent reviews include one from Gabe[88], where new electrode shapes and current uses are discussed by Low[89], where they talk about developments including RCE Hull cell design along with its use in metal deposition. Finally, the most recent review by Walsh[90] covers the RCE's

application to corrosion.

While numerous RCE designs can be found Figure 6-2 shows a general diagram of the typical components found in most systems. The primary system component which sets it apart from most other cell types is a motor to power the rotation along with a controller to set rotation rates. The shaft used is typically insulated except for the working electrode (WE) area which is either colinear with the rest of the shaft, inset to minimize edge effects. The shaft is ordinarily circular in cross-section, though other shapes have been used [89]. The Counter electrode can take on any number of shapes ranging from a fully cylindrical shape, to flat plates, or other baffle type designs. As is typical of most electrochemical experiments, there is a reference electrode which is connected to a potentiostat along with the WE and CE. Since the RCE is not as popular as the RDE, few commercial systems exist that are designed specifically for use as an RCE, so custom systems are often developed. To this author's knowledge, Gamry instruments/Pine Research is the only company that markets commercial off the shelf products directly to the RCE market.

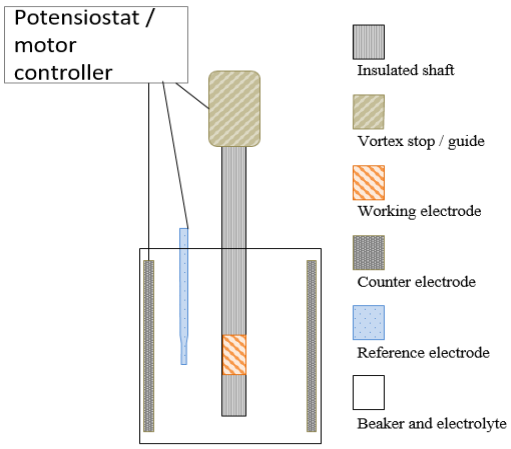

Figure 6-2. Components of general RCE.

The hydrodynamics of the RCE can be particularly interesting, especially in comparison to the relatively simple hydrodynamics of the RDE. The RDE hydrodynamics were solved mathematically due to its relative simplicity, as demonstrated by Levich [2]. The RCE, on the other hand, has yet to be solved mathematically due to the turbulent nature of the flow. As such, the equations that define it have come through experimentation. For

example, within an RCE experiment, if a 25.4mm dia cylinder is used, such as in the work described below, as rotation rates change the flow could quickly go from a laminar flow to full turbulent before reaching even 10RPM. This change from laminar to turbulent makes the RCE hydrodynamically very interesting. Several researchers, Taylor most notably, have looked into this transition and the various flow regimes that occur during this transition [85], including Andreck [91] who's plot showing the various flow regime, is given in Figure 6-3. The plot shows how the development of turbulence vs rotation rate of the inner and outer cylinders. For the RCE, the outer cylinder is stationary, and the turbulence development path would follow the orange line on $R_0 = 0$. The plot shows how the fluid starts off in a Couette flow and then gradually develops into turbulent Taylor vortices. Figure1-4 shows an impressive image of Taylor vortices from [92].

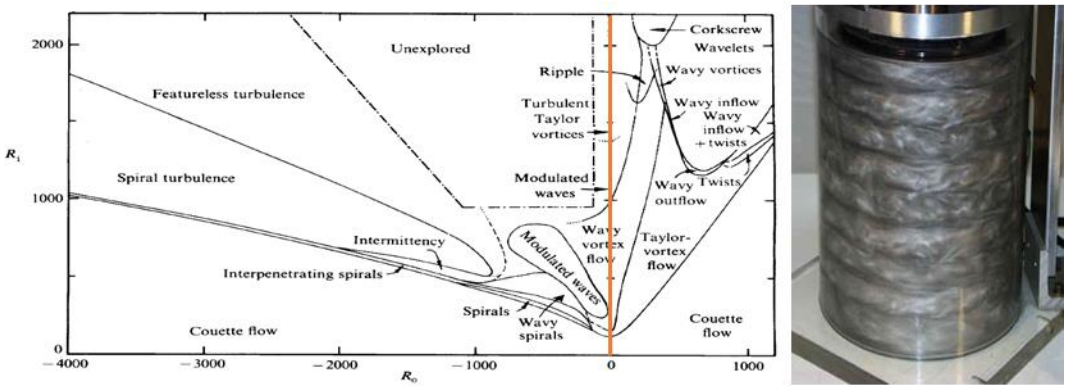

Figure 6-3. Left, Flow regimes from [91] with orange added to show the condition of the outer cylinder fixed such as used in this research. Right, Image of Taylor flow from [92]

While the hydrodynamics are extremely important for RCE deposition experimental data such as that of Eisenberg, Gabe, and others has led to the equations most often used to describe the system. In Gabe's first paper from 1972 [86], he describes the conditions of mass transfer during laminar flow conditions. Gabe describes the correct way to define Re as given in Eqn. 6-1 where U is the peripheral velocity, υ the kinematic viscosity and d the diameter of the cylinder. The work also noted that Re_{crit} of the RCE can be in the range of 50-200 depending on the roughness of the cylinder surface. Putting this into perspective, a 25.4mm diameter electrode spinning at 6RPM would have a $Re \approx 200$, thus laminar flow is uncommon in most circumstances. Gabe's second paper of 1972 and most other work thus discusses RCE properties in turbulent flow conditions.

$$Re_{RCE} = \frac{Ud}{\upsilon} = \frac{\pi\, d_{cyl} F \rho}{60\mu} \qquad (6\text{-}1)$$
$$Re_{RDE} = \frac{Ud}{\upsilon} = \frac{\pi\, r_{rde} F \rho}{60\mu}$$

Possibly the most general description of mass transport to the RCE is given by dimensionless numbers in Eqn. 6-2 [93]. The Sherwood number, Sh, is a number that describes convective mass transport vs. diffusive mass transport. Sc is the dimensionless number describing viscous vs. diffusive transport, Le is a ratio of the electrode roughness to the diameter and Re the Reynolds number. The coefficients K, a, b, and c depend on the set up being used and conditions during deposition including temperature, electrolyte properties, surface roughness, and more. Gabe [93] noted that the values of K and a depend significantly on the surface, and values have been empirically calculated ranging from K : a of 0.0062 and 1 for a wrapped wire electrode all the way to 1 and 1 for a knurled electrode. Those two conditions are extreme cases, whereas the more common approximation is for the smooth electrode with K and a of 0.079 and 0.70. In practical cases, the equation is often simplified to relate it directly to the limiting current, I_{lim} (Eqn. 6-3) which comes directly from the mass transport, Eqn. 6-4 [94].

$$Sh = K\, Re^{a} Sc^{b} Le^{c} \qquad (6\text{-}2)$$

$$I_{lim,RCE} = 0.0487 nFAC d^{0.4} D^{0.644} \nu^{-0.344} \omega^{0.7} \qquad (6\text{-}3)$$

$$k_{m,RCE} = 0.0487 d^{0.4} D^{0.644} \nu^{-0.344} \omega^{0.7} \qquad (6\text{-}4)$$

Because the RDE is the more common of the two electrodes and is used as the starting point for this research, it is worth looking at how the two electrodes compare, starting with the Re. For comparison, it is useful to assume that both electrodes are smooth. Gabe, [95], has a table that gives a comparison of the two electrodes, though it is useful to look at this from a graphical point of view and vs. RPM since that is what the experimentalist typically has to work with. Figure 6-4 shows the Re of both electrodes as a function of RPM, Eqn. 6-1. The RCE with a 2.54cm Dia. goes into turbulent flow at Re_{crit} =200, whereas the RDE with a 2.54cm Dia. Goes to Re_{crit} = 20,000 before turbulence

begins, which correlates to an RPM of 7 and 270,000, respectively. Looking at Eqn. 6-1 *d* and *F* are the only two RCE variables that can be easily adjusted. To achieve laminar flow in an RCE experiment, rotation rate, and electrode diameter are very limited. The RDE is hard-pressed to achieve turbulent conditions, which demonstrates why the RDE and RCE tend to see such different applications. Pine Research sells a 12mm RCE which would allow rotation to about 140RPM before the onset of turbulence. For the industrial case, though, the size of the rotor can easily be 10x or more times the size of the plotted graph below [88].

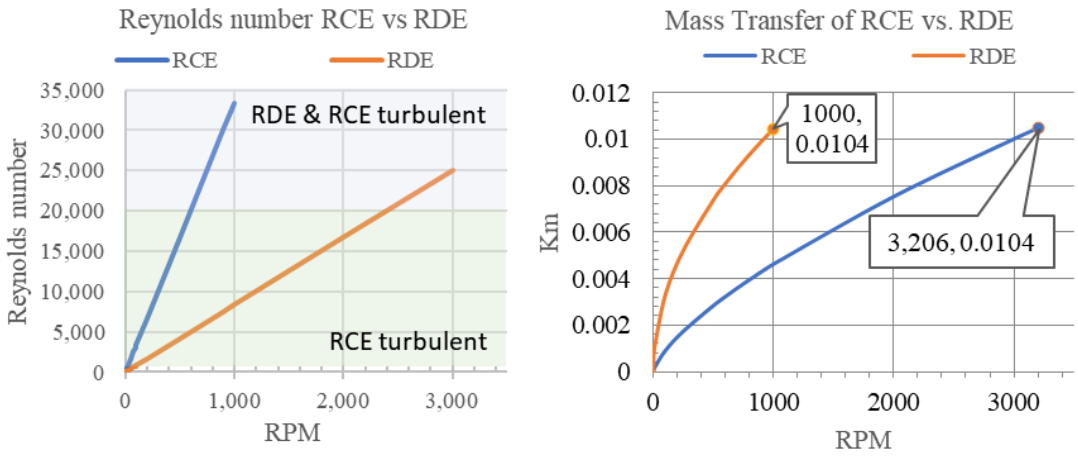

Figure 6-4. RCE vs. RDE Reynolds number and mass transfer.

Figure 6-4 shows k_m using Eqns. 2-17 and 6-4, where the diameter of the RCE and RDE are the same. The RDE has significantly higher mass transfer than that of the RCE at a given RPM. To take an experiment from the RDE to the RCE, the RPM must be significantly increased to match the same mass transport properties. While the RDE does have a higher mass transfer rate, the area of mass transfer for the RCE may be significantly larger. The RCE can have an infinitely long surface, which would allow more surface area for deposition. When the height of the RCE electrode is about half its radius, the RCE and RDE have the same area, i.e., a 2.54cm dia. RCE electrode with 0.625cm height has the equivalent area of a 2.54cm dia. RDE. With the RCE, if the conditions allow, the bottom of the cylinder could be used, adding the disk portion of the RCE to the electrode surface as well. This can be advantageous for industrial processes where the long cylindrical shape

is a convenient form factor for large scale reactors.

6.3. Experimental section

6.3.1. Custom RCE design

For depositions, the Gamry RDE was replaced with a custom RCE in order to deposit onto 381 mm (15”) shafts. Figure 6-5 shows a diagram of the RCE with the two-piece shaft. The electrolytic cell consisted of a plastic 1 L graduated cylinder with two plugs machined to fit inside the cell and minimize electrolyte volume. An Ag/AgCl reference electrode (BASF) was inserted through the top plug such that it was in close proximity to the working electrode. The top plug also served to minimize the vortexing of the fluid during depositions. A Stainless-Steel mesh was used for the counter electrode. For the Cu tube samples, a custom fixture that mimicked a shaft was fabricated from a 25.4 mm dia. x 342.9 mm long (13.5”) 7071 Al shaft that was split in two and then screwed together to hold the Cu tubes and make contact. The Al shafts were then masked to prevent deposition or corrosion. The Cu shaft samples, Figure 6-5c, were simply treated as shafts that screwed directly into the RCE motor. After deposition, the Cu shafts could be directly inserted into the torque measurement setup. During deposition, both the tubes and the shafts were masked to expose a 6.35 mm (0.25”) long ring of Cu to the electrolyte.

6.3.2. Shaft preparation details

In this work, two types of substrates were used: Cu tubes and Cu Shafts. To develop the electrodeposition parameters, 25.4 mm (1”) diameter x 38.1 mm (1.5”) long Cu tubes were cut from 152.4 mm (6’) long Copper 101 tube (McMaster-Carr). After cutting, each tube was sanded with 80 grit sandpaper (3M) in a circumferential direction to remove surface defects. Next, the tubes were sanded with progressively higher grits up to 400, 600, or 3000 grit. After polishing, two texture directions were created using 400 grit: circumferential and longitudinal. The Cu shafts (25.4 mm diameter by 381.0 mm (15”) long) were cut from a 0.91 m (3’) Copper 101 solid shaft (McMaster-Carr). A key slot was then cut on both ends to mate with the test fixture used in the prototype torque sensor. A threaded and tapped hole was also added to each end for mounting directly to the RCE

motor. The shafts then followed the same surface preparation procedure as the tubes.

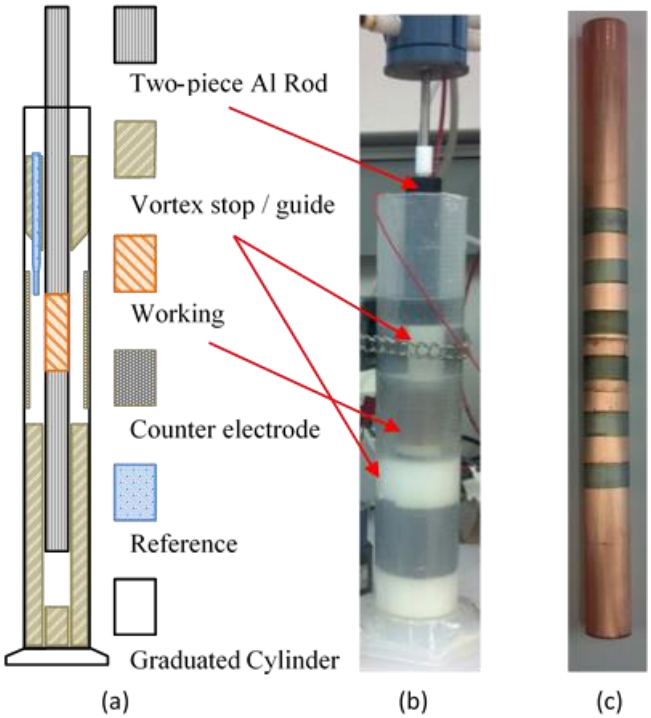

Figure 6-5. a) Schematic of rotating cylinder electrode(RCE) electrodeposition cell. b) Image of RCE used in depositions, shown with the two-piece shaft. c) Example of shaft with Fe1-xGax films used for torque sensor device.

6.3.3. Shaft preparation details

In this work, two types of substrates were used: Cu tubes and Cu Shafts. To develop the electrodeposition parameters, 25.4 mm (1") diameter x 38.1 mm (1.5") long Cu tubes were cut from 152.4 mm (6') long Copper 101 tube (McMaster-Carr). After cutting, each tube was sanded with 80 grit sandpaper (3M) in a circumferential direction to remove surface defects. Next, the tubes were sanded with progressively higher grits up to 400, 600, or 3000 grit. After polishing, two texture directions were created using 400 grit: circumferential and longitudinal. The Cu shafts (25.4 mm diameter by 381.0 mm (15") long) were cut from a 0.91 m (3') Copper 101 solid shaft (McMaster-Carr). A key slot was then cut on both ends to mate with the test fixture used in the prototype torque sensor. A threaded and tapped hole was also added to each end for mounting directly to the RCE motor. The shafts then followed the same surface preparation procedure as the tubes.

6.3.4. Deposition Details

In order to optimize the electrodeposition of Fe1-xGax on cylindrical surfaces, two solutions, compositions, and a variety of potentials and rotation rates were studied. The solutions were based on [96] and consisted of 500 mM sodium sulfate (Alpha Aesar), 31 mM sodium citrate (Alpha Aesar), either 61.9 mM or 82.5 mM Gallium sulfate hydrate (Alpha Aesar), and 15 mM Iron Sulfate (Alpha Aesar). The solution PH was then adjusted to a value of 3.75 with NaOH using a calibrated PH meter (Oakton pH 6+). The potential was varied between 1.05 V and 1.25 V, using a Gamry PCI4/300. The rotation rate was controlled using a Gamry 710 RDE with rates ranging from 500 RPM up to 3200 RPM in order to mimic the RDE mass transfer rates from [96].

6.3.5. Measurement Details

The films were characterized by three different methods: energy dispersive spectroscopy (EDS) for composition, and vibrating sample magnetometry (VSM) for magnetic properties, and custom torque measurements for magnetostrictive response [74]. Specifically, a Jeol JSM-6610LV SEM with an Oxford Instruments Inca X-Act EDS was used to determine the %Ga, %Fe, and %O in each film, after removing peaks from Cu and trace elements. For VSM (Lakeshore 7410)), 6.35 mm x 6.35 mm samples with thickness of 250 nm (estimated) were cut from the Cu tubes and mounted to a quartz rod for measurement with the magnetic field parallel to the plane of the film with the polished/textured direction both parallel to the magnetic field and rotated 90°. The magnetization was measured while the applied field was swept ±0.2 T to saturate the samples. Due to sample texture, the thickness was estimated based on the film's moment. A saturation magnetization of 1520 kA/m was used as previously reported for electrodeposited samples [97].

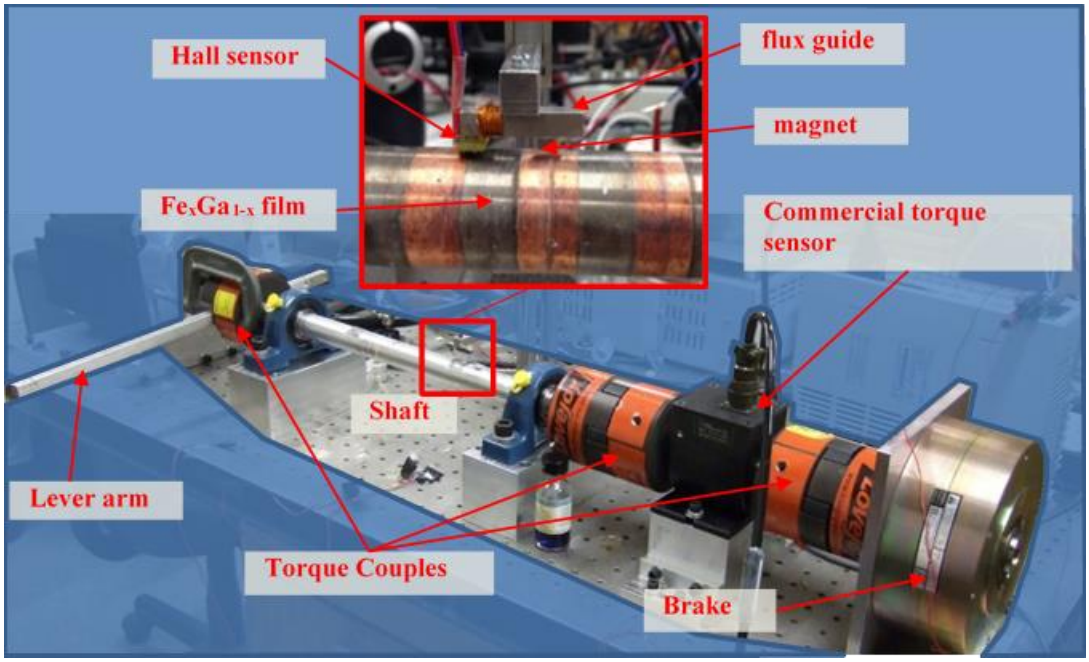

Figure 6-6. Illustration of torque measurement technique.

A prototype torque sensor verified the functionality of directly coupled $Fe_{1-x}Ga_x$, Figure 6-6. Films with nominal thicknesses up to 250 nm (estimated from VSM) were deposited on solid Cu shafts that had surfaces with either a polished, longitudinal or circumferential texture. The films were deposited for 10 min at 1.2 V and 1500 RPM to achieve a composition of $Fe_{85}Ga_{15}$. The end of each Cu shaft was fixed using a particle brake (Placid Industries, Inc.). A lever arm was attached to the other end, and known weights (2.27 kg (5 lb), 4.53 kg (10 lb), 6.80 kg (15 lb)) were used to apply static torque to the shaft. The weights were hung 254 mm (10") away from the shaft to create 5.65 Nm (50 in-lb), 11.30 Nm (100 in-lb), or 16.95 Nm (150 in-lb) of torque. A calibrated commercial slip ring torque sensor (Sensor Developments Inc. model 01324-022-G00A0) was used to provide a standard readout of the torques for calibration. The sensor had a sensitivity of 10 mV/in-lb and a range of 0.35 Nm (3.125 in-lb) to 2300 Nm (20,000 in-lb), which covers the 5.65 Nm to 16.95 Nm range used in the experiments. Torque couples (Lovejoy inc.) were used in between each connection to ensure a reliable torque linkage. A magnetic circuit, composed of a Hall Effect sensor (AKM EQ-730L) and a biasing magnet (0.4 T) on high-permeability steel, was suspended ~1 mm above the deposited Fe1-xGax strip on the shaft, with the air gap providing non-contact measurement. The Hall

Effect sensor was oriented to sense magnetic field strength in the vertical orientation such that the sensor operated within its linear range. This circuit created a flux path through the magnet, the steel, the sensor, and the Fe1-xGax as shown in Figure 6-7. For each of the $Fe_{1-x}Ga_x$ films, four torque states (0, 5.65, 11.30, and 16.96 Nm) were applied to the shaft, and output was recorded simultaneously from both the Hall Effect sensor and the standard torque sensor. Sensitivity was calculated using the Hall Effect signal at each applied torque after filtering and averaging to remove noise. A least-squares regression was applied to the output to determine the response characteristics of the sensor in μT/Nm.

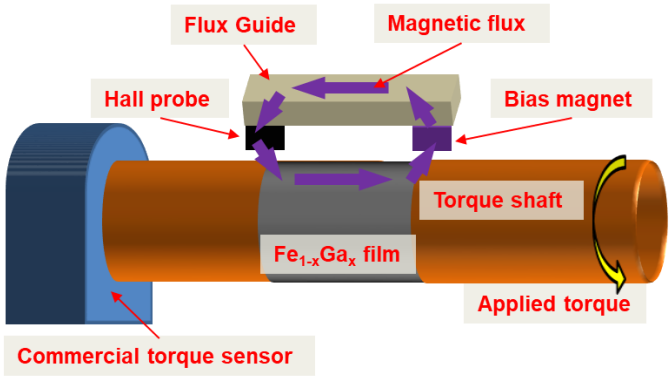

Figure 6-7. Illustration of the torque measurement technique.

When torque is applied to the shaft, torsional strain and shear stress on the surface of the shaft produce maximum tensile and compressive stresses in the $Fe_{1-x}Ga_x$ film at ±45° from the longitudinal axis of the shaft [98], [99]. The inverse magnetostrictive response of the film causes the magnetic anisotropy to align with the direction of maximum tensile stress, i.e., at an orientation of ±45° from the longitudinal axis of the shaft, so as to minimize magneto-mechanical anisotropy energy in the $Fe_{1-x}Ga_x$ film. This produces a measurable change in the magnitude of the flux passing through the magnetic circuit. The Hall effect tracks this change in the magnitude of vertical magnetic flux.

6.4. Results

6.4.1. Initial film development on custom RCE

The first step in achieving $Fe_{1-x}Ga_x$ deposition on cylinders was to modify the

parameters from the RDE work of Reddy and Estrine for the RCE. Ga is typically deposited using a citrate (Cit) complexing agent. Since Fe is more electronegative than the GaCit complex, it deposits faster than Ga. To compensate, an excess of Ga is used in the electrolyte, along with controlled mixing to hone in the Ga:Fe ratio. The mass transfer (k_m) characteristics of RCE and RDE were shown in Eqn. 6-14 and 2-17 and shown in Figure 6-4. From the equation and plot, it can be seen that faster rotation rates are needed in the RCE as compared to RDE to achieve similar k_m values. For example, to match the k_m values of the RDE at 1000 RPM [96], 3200 RPM would be needed in the RCE. However, this rotation rate is extremely fast for RCE applications. From Eqn. 6-1, 3200 RPM yields a Reynolds number of 106,880 which indicates high turbulence.

Early attempts to match the k_m of RDE led to excessive vortex formation at the RCE's surface. Figure 6-8 demonstrates the formation of vortexing in a solution with a rotating cylinder. At low rotation rates, Figure 6-8a, no visible vortexing can be seen at the electrodes surface. At 10,00 RPM, a noticeable vortex has formed, Figure 6-8b, though still only around 1cm deep. As the rotation increased so did the depth of the vortexing, such that at 3000RPM the vortex can be seen almost to the bottom of the container. To minimize vortexing, the "Vortex Stop," Figure 6-8d, was used in the RCE cell design which helps to minimize vortexing up to 2500RPM.

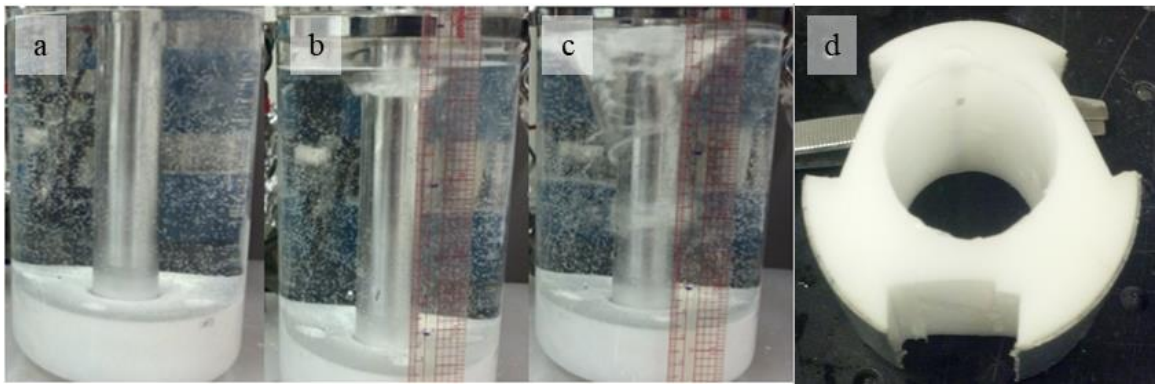

Figure 6-8. A,B and C, development of turbulence with increasing rotation. D, Vortex stop created to mimimize vortexing.

6.4.2. Deposition parameter development

Using the RCE cell of Figure 6-5 deposition in the cell was tested. Cyclic voltammetry (CV) at 0 RPM was first used to determine the range of potential at which deposition onto the Cu tube would occur. Figure 6-9 shows an example of CV of FeGa. From the plot, deposition voltages in the 0.8V to 1.25V range were chosen for initial deposition test. Similarly, rotation rates in the range of 1500RPM to 3500 RPM were used to try and match the range of mass transfer from [96].

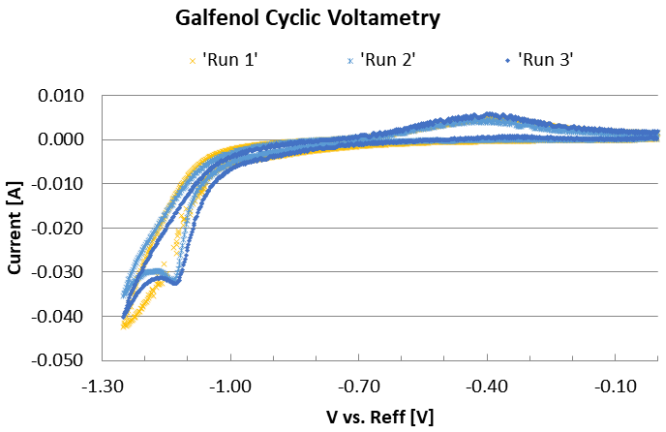

Figure 6-9. Cyclic voltammetry example. GaFe on Cu tube sample.

A sample of the films resulting from the deposition can be seen in Figure 6-10 along with the deposition conditions and EDS results. A range of films with different %Ga were obtained though overall, the films came out brown and chalky which is typical of oxidized $Fe_{1-x}Ga_x$ (Figure 6-10). Initially this effect was thought to be due to vortexing, which was occurring at the higher RPM range since the vortex stop only minimized vortexing in the deposition area up to about 2500RPM.

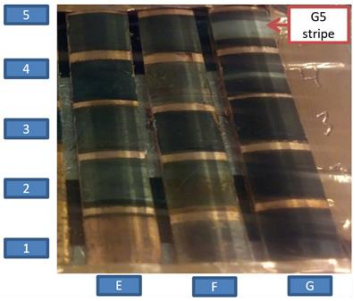

EDS#	Pot [V]	RPM	Time (min)	%O	%Ga
E2	1.00	2000	5	15.8	5.1
E3	1.10	2000	5	16.0	2.3
E4	1.20	2000	5	31.0	16.7
E5	0.90	2000	5	21.2	3.7
F1	0.70	2500	5	35.3	57.1
F2	0.80	2500	5	21.6	0.0
F3	0.90	2500	5	17.4	2.4
F4	0.70	3000	5	13.4	0.0
F5	0.80	3000	5	23.9	0.0
G1	1.25	1500	5	36.9	21.5
G2	1.25	2000	5	31.2	21.2
G3	1.25	2500	5	27.4	22.6
G4 stripe	1.25	3000	5	13.5	25.4
G5 stripe	1.25	3500	5	26.2	26.3

Figure 6-10. Left, Test deposition of FeGa films. Right, associated deposition conditions and %O and %Ga

To confirm that the oxidized deposition was due to the setup and not the solution or substrate, test depositions were performed on the RDE. Cu tubes samples that were used on the RDE were cut, flattened, and textured in the same manner as on the RCE samples. The solution that had been used on the RCE which resulted in oxidized films was then used to perform RDE deposition on the now flat samples. Figure 6-11 shows the results of the test deposition. The samples came out metallic looking in appearance similar to what had been seen in the previous work [96]. Subsequent EDS confirmed that the films were oxygen-free as well.

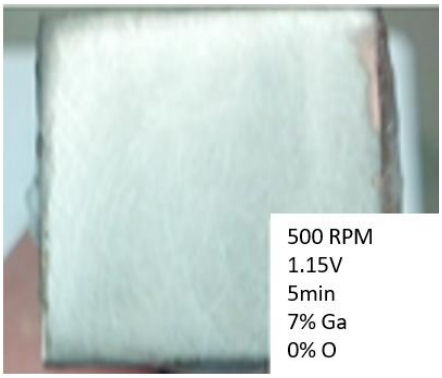

Figure 6-11. FeGa deposited using RDE with flattened Cu tube.

Using a light to help illuminate the solution during deposition revealed that a large number of bubbles were getting trapped in the deposition area of the cell. The gasses getting trapped were likely H_2 and O_2 gas from the anode/cathode reactions along with atmosphere that was getting vortexed into the solution. In a "standard" RCE setup, the fluid and gasses move downward along the shaft and radially out. As gases get formed or vortexed into the solution they should be pulled away from the electrode surface due to convection and rise out of the solution due to buoyant forces. The vortexing along the shaft's circumference, along with the vortex stop effectively blocked the gasses' path to the atmosphere. The gasses were then getting trapped in the turbulent fluid. The simple addition of relief channels (Figure 6-12) to the outer circumference of the vortex stop prevents bubble entrapment from occurring.

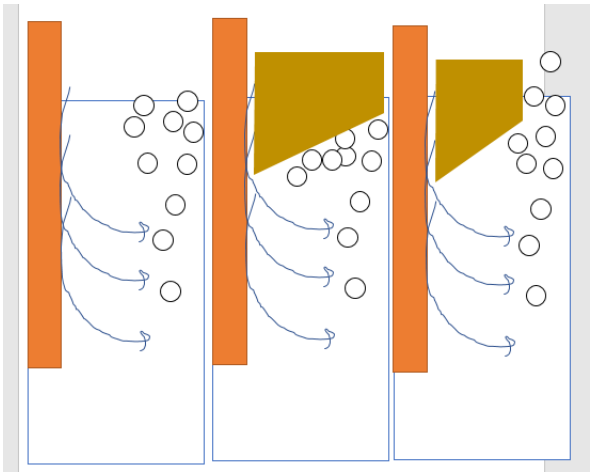

Figure 6-12. Bubble trapping in RCE.

With the addition relief channels to the vortex stop, depositions were tested again. Using the light, significantly fewer bubbles could be seen in the solution during deposition. Following deposition using 1.15 V and various rotation rates, metallic films similar to the RDE films were obtained. The sample composition was measured with EDS and revealed the films to be Oxygen-free FeGa films.

6.4.3. Film Composition

With the fixture development complete, the development of the film stoichiometry was pursued. Cu tubes and solutions, as described in section 6.3.3 “Deposition details,” were used to deposit films through a range of RPM and potential.

EDS analysis of the films showed that the Ga concentrations were indirectly proportional to the mass transfer, Figure 6-13a (right axis), as expected. Figure 6-13b summarizes the dependence of Ga concentration on rotation rate, deposition potential, and electrolyte concentration. This bar chart shows that the composition can be controlled over the 15%Ga to 35%Ga range that has been shown to have useful magnetostriction constants [76]. It is also important to note that the $Fe_{1-x}Ga_x$ films made within the parameters studied here did not contain oxygen impurities within the limit of detection.

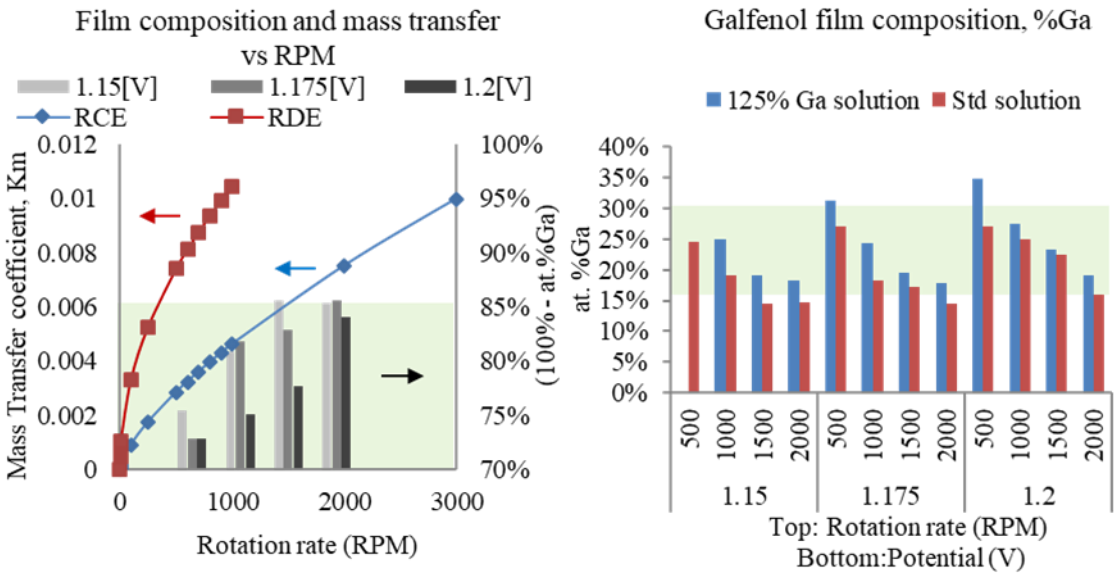

Figure 6-13. a) Variation of film composition with mass transfer rate and RPM. b) %Ga content of films with various rotation rates and applied potential for the standard plating solution and the +25%Ga plating solution. The highlighted area is the range of desired composition (GaxFe1-x, 0.15<x<0.35).

6.4.4. Magnetic Characterization

The impact of substrate texture was studied using 62.5 mm^2 samples of $Fe_{1-x}Ga_x$ films on polished Cu tubes (3000 grit) and textured (400grit) Cu tubes, Figure 6-14a,b. The polished tube, Figure 6-14a, yielded VSM loops that were almost identical in both the transverse and longitudinal measurements because the polycrystalline film was isotropic. In contrast, Figure 6-14b shows that the surface of the 400 grit substrate is highly textured. The deep grooves induced a shape anisotropy in the film, which made it magnetically softer along the direction of texture. The susceptibility is 260% higher, and the remanent magnetization of the textured film 2.5x greater in the direction of texturing.

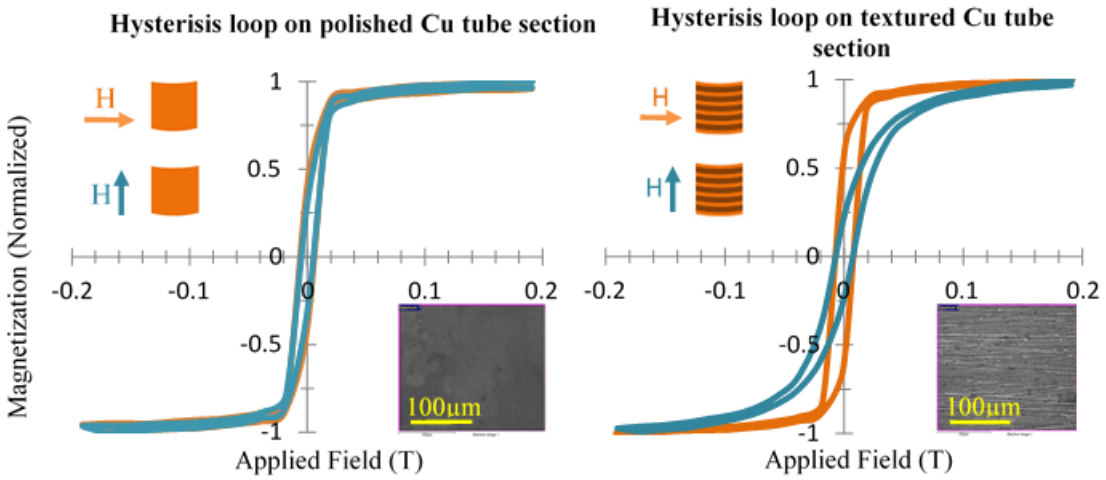

Figure 6-14. a) Hysteresis loop of $Fe_{1-x}Ga_x$ film on a polished surface. b) Hysteresis loop of Fe_{1-x}Gax film on a textured surface. Insets: SEM images of Fe_{1-x}Gax films on polished and textured surfaces.

6.4.5. Realization of Electroplated Torque Sensors

Prototype torque sensors were made from shafts with the three textures, and torques of between 0 and 16.95 Nm were applied for measurements. The plots show the applied static torque, as recorded by a calibration torque meter, and the resulting change in magnetic flux through the magnetic circuit, as recorded by the Hall Effect sensor. As torque was applied in steps of 5.65 Nm, the calibrated torque sensor responded with a stepwise increase in the output following a small transient due to the addition of weights to the lever arm. Other transients in the calibrated torque sensors are due to noise in the environment. Similarly, the Hall sensor output increased (the applied negatively signed B-field (~12 mT,~1.0 V) increased towards zero) with the applied torque. This increase was due to the rotation of magnetization state of the $Fe_{1-x}Ga_x$ film away from its no-load state, which was longitudinal due to biasing, towards 45° to the shaft axis.

The polished shafts showed a response of 0.71 µT/Nm. The longitudinally textured shafts showed a greater response with a sensitivity of 2.30 µT/Nm, and the circumferentially textured shafts showed the best response with a sensitivity of 4.07 µT/Nm.

The effect of texturing can be explained as a balance of stress anisotropy and shape anisotropy. The no-load magnetic anisotropy was determined by the combined effects of the shaft surface texture, the strength of the permanent magnet, and flux through the torque-

sensing magnetic circuit. Smooth shafts exhibited the smallest response to torque-induced stress because they had isotropic magnetization characteristics, i.e. no dominant easy axes (VSM data and Figure 6-15, left). Shafts with longitudinal texture had longitudinal shape anisotropy, which is in the same direction as the no-load magnetization. In this case, Figure 6-15, middle) stress-induced anisotropy produced a modest rotation of magnetic anisotropy of the $Fe_{1-x}Ga_x$ film away from its no-load direction with a change of 2.30 µT/Nm in flux through the magnetic circuit. Integration of the VSM curves from Figure 6-15 shows the longitudinal remanent energy of the polished rod is only $8.11M_s$ J/m^3, vs. the longitudinally textured rod at $12.14M_s$ J/m^3, which may account for the higher sensitivity of the longitudinally textured shaft. For circumferentially-textured shafts, the $Fe_{1-x}Ga_x$ magnetic texture-induced anisotropy lies 90° to magnetic flux path which is along the shaft. This extra circumferential anisotropy lowered the stress-anisotropy energy required to rotate the moment away from the no-load magnetically biased state. For this case (Figure 6-15, right), stress-induced anisotropy produced an increase of ~70% in rotation of magnetic anisotropy of the $Fe_{1-x}Ga_x$ film away from its no-load direction, leading to a change of 4.07 µT/Nm in flux through the magnetic circuit. Hence, this prototype sensor was more sensitive to torque within the measured range. Future sensors could control the sensitivity to different ranges of torque by varying the texture of the shaft and the strength of the permanent magnet (recall that 0.04 T permanent magnets were used here). These variables could expand the dynamic range of torques that can be detected.

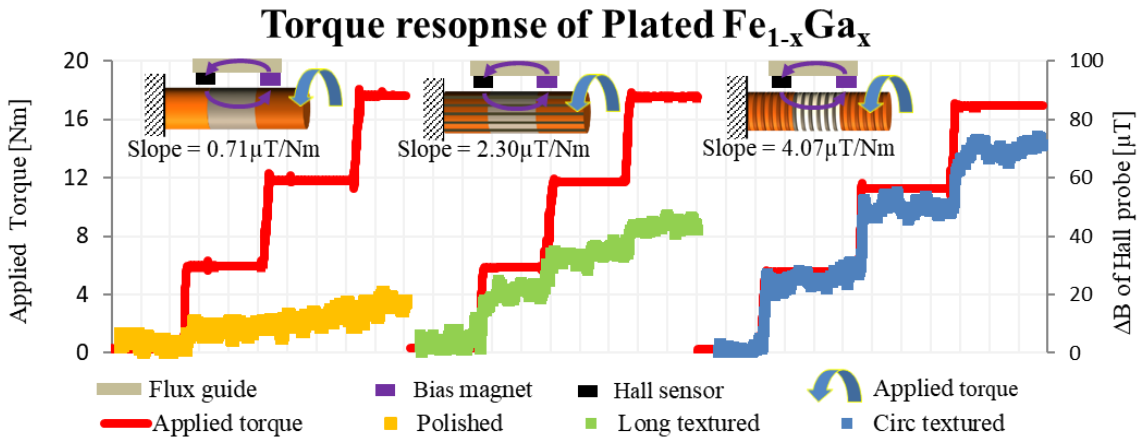

Figure 6-15. Torque measurement set up and response of electroplate $Fe_{1-x}Ga_x$ films. Red, applied toque as measured by commercial torque meter. Yellow, polished shaft. Green, longitudinally textured shaft. Blue, circularly textured shaft. Insets show the magnetic circuit with the purple arrow representing the first circuits flux path

For comparison to current devices, the sensitivity of the 250 nm (estimated from VSM) electrodeposited $Fe_{1-x}Ga_x$ is about ten-fold lower than the sensitivity of discrete 635 μm thick $Fe_{1-x}Ga_x$ patches, which are attached to the shafts via adhesives [100]. Further studies with thicker films are needed to determine the extent to which electrodeposited films can compete with adhesively bonded patches. Electrodeposited $Fe_{1-x}Ga_x$ films may be the only option when nano- or micro-scale torque sensors are needed, and this work verifies that they will be viable options.

6.5. Conclusion

Direct deposition of magnetostrictive $Fe_{1-x}Ga_x$ has been demonstrated onto torque elements using a rotating cylinder electrode (RCE) for use in torque sensors. By varying the RCE rotation rate (500-2000 RPM), deposition potential (1.0-1.2 V), and electrolyte, the film composition was controlled from 15%Ga to 35%Ga, which is the optimal range for magnetostriction in the Fe1-xGax alloy system. Additionally, it was shown that texturing the surface onto which the film was deposited affected the film's response by inducing a magnetic anisotropy. The advantages of these torque sensors are that they are easy to fabricate, allow for direct coupling, and are noncontact. With sensitivities in the range of 0.70 to 4.07 μT/Nm, these sensors are promising new directly-integrated alternatives for future applications.

7. CONCLUSIONS

Throughout the work presented above, it should be apparent to the reader how electrochemistry, magnetics, and sensor technology played a significant role in this research. Three different sensing technologies were presented utilizing different magnetic materials, deposition methods, and various processing techniques to achieve five different sensors.

In chapter 4, magnetic sensors for medical devices, and more specifically, catheters were presented. In addition to the patented work [43], [42], [101], two different inductive sensors based on research into electromagnetic tracking sensors were pursued. For both sensors, the concepts utilized the potential of high aspect ratio structures that are possible using etched AAO. A method to etch AAO was developed and structures with aspect ratios up to 80:1 were fabricated. While the method shows promise as a fabrication method for high aspect ratio structure, further refinement would be required to fabricate the structures required. Refinement of the etch parameters and further investigation of reducing the capillary forces while drying may aid in further development.

In chapter 5, a flow sensor and a vibration sensor were presented that utilized nanowires like biomimetic cilia fixed above a GMR sensor. The flow sensor showed the ability to measure flows in the μl/min to ml/min range as a microvolt signal. Further optimization of the design may include making the nanowires more mechanically robust, corrosion-resistant, and improvement of the flow geometry to aid in fabrication. For the vibration sensor, it was shown that it could sense vibrations in the low frequency (1-5 Hz) range. The design of the sensor has significant room for improvement through optimization of the nanowire array and, more importantly, the proximity of the nanowires to the sensing element. Both sensors may be able to take advantage of the continued development in the field of MR through the use of MR sensors explicitly designed for this application or through use of TMR to help reduce their power.

In the final chapter, the electrodeposition of FeGa onto cylindrical substrates for torque sensing applications was demonstrated. A custom RCE fixture was designed and troubleshot to help fabricate $Fe_{1-x}Ga_x$ films. The deposition parameters needed to achieve 15% to 35% Ga films, the optimal range for magnetostriction, were determined and then used in torques sensor fabrication. The addition of shape anisotropy and its effect on a prototype sensor design was also explored. Further development of this design may include optimization of the magnetic circuit design and the texturing. Similarly, other applications such as micro torque sensors or strain sensors could be had through a slight modification of the design.

The sensors presented here are just a few of the many possibilities out there. While electrochemistry and magnetism were the two primary fields of study utilized in this research, many other aspects such as microfabrication, circuit design, materials science, and more played a role. Further development of any of the design presented is possible, and consideration of the research presented will hopefully help whoever comes next to take their design further.

8. REFERENCES

[1] C. M. A. Brett and A. M. O. Brett, *Electrochemistry: principles, methods, and applications*. Oxford ; New York: Oxford University Press, 1993.

[2] V. G. Levich, *Physiochemical hydrodynamics*. Englewood Cliffs, N.J.: Prentice-Hall, 1962.

[3] D. B. Montgomery and J. Terrell, "SOME USEFUL INFORMATION FOR THE DESIGN OF AIRCORE SOLENOIDS, PART I. RELATIONSHIPS BETWEEN MAGNETIC FIELD, POWER, AMPERE-TURNS AND CURRENT DENSITY. PART II. HOMOGENEOUS MAGNETIC FIELDS:," Defense Technical Information Center, Fort Belvoir, VA, Nov. 1961.

[4] B. D. Cullity and C. D. Graham, *Introduction to magnetic materials*, 2nd ed. Hoboken, N.J: IEEE/Wiley, 2009.

[5] "Magnetic Units." [Online]. Available: http://www.ieeemagnetics.org/index.php?option=com_content&view=article&id=118&Itemid=107. [Accessed: 15-Sep-2019].

[6] P. Quarterman *et al.*, "Demonstration of Ru as the 4th ferromagnetic element at room temperature," *Nat. Commun.*, vol. 9, no. 1, pp. 1–6, May 2018.

[7] S. Tumański, *Handbook of magnetic measurements*. Boca Raton: Taylor & Fracis, 2011.

[8] M. J. Dapino, Z. Deng, F. T. Calkins, and A. B. Flatau, "Magnetostrictive Devices," in *Wiley Encyclopedia of Electrical and Electronics Engineering*, American Cancer Society, 2016, pp. 1–35.

[9] B. Garneyer, R. Hösl, U. Viola, and R. Heuckelbach, "Magnetostrictive elongation sensor," US8035372B2, 11-Oct-2011.

[10] F. T. Calkins, A. B. Flatau, and M. J. Dapino, "Overview of Magnetostrictive Sensor Technology," *J. Intell. Mater. Syst. Struct.*, vol. 18, no. 10, pp. 1057–1066, Oct. 2007.

[11] Z. Deng and M. J. Dapino, "Review of magnetostrictive vibration energy harvesters," *Smart Mater. Struct.*, vol. 26, no. 10, p. 103001, Sep. 2017.

[12] G. Engdahl, Ed., *Handbook of giant magnetostrictive materials*. San Diego, CA: Academic Press, 2000.

[13] "TdVib, LLC Terfenol-D - ETREMA Products, Inc." [Online]. Available: http://tdvib.com/terfenol-d/. [Accessed: 16-Sep-2019].

[14] B. M. Kreutz, "Mediterranean Contributions to the Medieval Mariner's Compass," *Technol. Cult.*, vol. 14, no. 3, pp. 367–383, 1973.

[15] S. Ben-Haim, D. Osadchy, U. Peless, and I. Greenberg, "System for determining the location and orientation of an invasive medical instrument," US6690963B2, 10-Feb-2004.

[16] E. Ramsden, *Hall-effect sensors: theory and applications*, 2nd ed. Amsterdam ; Boston: Elsevier/Newnes, 2006.

[17] E. H. Hall, “On a New Action of the Magnet on Electric Currents,” *Am. J. Math.*, vol. 2, no. 3, p. 287, Sep. 1879.
[18] R. F. Pierret, *Advanced semiconductor fundamentals*, 2nd ed. Upper Saddle River, N.J: Prentice Hall, 2003.
[19] C. J. B. Ford, S. Washburn, M. Büttiker, C. M. Knoedler, and J. M. Hong, “Influence of geometry on the Hall effect in ballistic wires,” *Phys. Rev. Lett.*, vol. 62, no. 23, p. 2724, 1989.
[20] S. Liu, H. Guillou, A. D. Kent, G. W. Stupian, and M. S. Leung, “Effect of probe geometry on the Hall response in an inhomogeneous magnetic field: A numerical study,” *J. Appl. Phys.*, vol. 83, no. 11, pp. 6161–6165, Jun. 1998.
[21] R. S. Popovic, J. A. Flanagan, and P. A. Besse, “The future of magnetic sensors,” *Sens. Actuators Phys.*, vol. 56, no. 1, pp. 39–55, Aug. 1996.
[22] R. S. Popovic, “The vertical hall-effect device,” *IEEE Electron Device Lett.*, vol. 5, no. 9, pp. 357–358, Sep. 1984.
[23] M. J. Caruso, T. Bratland, D. C. H. Smith, and R. Schneider, “A New Perspective on Magnetic Field Sensing,” p. 19.
[24] M. N. Baibich *et al.*, “Giant Magnetoresistance of (001)Fe/(001)Cr Magnetic Superlattices,” *Phys. Rev. Lett.*, vol. 61, no. 21, pp. 2472–2475, Nov. 1988.
[25] R. C. O’Handley, *Modern magnetic materials: principles and applications*. New York: Wiley, 2000.
[26] “Disk read-and-write head,” *Wikipedia*. 18-Sep-2019.
[27] S. Ikeda *et al.*, “Tunnel magnetoresistance of 604% at 300K by suppression of Ta diffusion in CoFeB/MgO/CoFeB pseudo-spin-valves annealed at high temperature,” *Appl. Phys. Lett.*, vol. 93, no. 8, p. 082508, Aug. 2008.
[28] W. F. Egelhoff *et al.*, “Critical challenges for picoTesla magnetic-tunnel-junction sensors,” *Sens. Actuators Phys.*, vol. 155, no. 2, pp. 217–225, Oct. 2009.
[29] A. Guedes, S. B. Patil, S. Cardoso, V. Chu, J. P. Conde, and P. P. Freitas, “Hybrid magnetoresistive/microelectromechanical devices for static field modulation and sensor 1/f noise cancellation,” *J. Appl. Phys.*, vol. 103, no. 7, p. 07E924, Mar. 2008.
[30] “Spotlight - Technology - MultiDimension Technology, The Leading Supplier of TMR Magnetic Sensors - MultiDimension Technology Co., Ltd.” [Online]. Available: http://www.dowaytech.com/en/download-center/spotlight.html. [Accessed: 23-Sep-2019].
[31] C. Reig and M.-D. Cubells-Beltrán, “Giant Magnetoresistance (GMR) Magnetometers,” in *High Sensitivity Magnetometers*, A. Grosz, M. J. Haji-Sheikh, and S. C. Mukhopadhyay, Eds. Cham: Springer International Publishing, 2017, pp. 225–252.
[32] G. Chatzipirpiridis, P. Erne, O. Ergeneman, S. Pané, and B. J. Nelson, “A magnetic force sensor on a catheter tip for minimally invasive surgery,” in *2015 37th Annual International Conference of the IEEE Engineering in Medicine and Biology Society (EMBC)*, 2015, pp. 7970–7973.
[33] F. Bourier *et al.*, “Electromagnetic Contact-Force Sensing Electrophysiological Catheters: How Accurate Is the Technology?,” *J. Cardiovasc. Electrophysiol.*, vol. 27, no. 3, pp. 347–350, 2016.
[34] A. M. Franz, T. Haidegger, W. Birkfellner, K. Cleary, T. M. Peters, and L. Maier-Hein, “Electromagnetic Tracking in Medicine—A Review of Technology, Validation,

and Applications," *IEEE Trans. Med. Imaging*, vol. 33, no. 8, pp. 1702–1725, Aug. 2014.
[35] X. Zeng, S. Song, J. Wang, H. Dai, and S. Su, "An analytic algorithm based position and orientation detection using a tri-axial magnetoresistive sensor," in *2017 IEEE SENSORS*, 2017, pp. 1–3.
[36] S. R. Kirsch, C. Schilling, and G. Brunner, "New form factors for sensors and field generators of a magnetic tracking system," in *Medical Imaging 2005: Visualization, Image-Guided Procedures, and Display*, 2005, vol. 5744, pp. 216–224.
[37] "Benatav micro coils white-paper.pdf." .
[38] K. R. Minard and R. A. Wind, "Solenoidal microcoil design—Part II: Optimizing winding parameters for maximum signal-to-noise performance," *Concepts Magn. Reson.*, vol. 13, no. 3, pp. 190–210, 2001.
[39] B. Greenburg, O. Zur, and R. Meloul, "Integrated Multi-Functional Endoscopic Tool," US20100016757A1, 21-Jan-2010.
[40] M. Olson, T. Nantsupawat, N. Sathnur, and H. Roukoz, "Chapter 4 - Cardiac Ablation Technologies," in *Engineering in Medicine*, P. A. Iaizzo, Ed. Academic Press, 2019, pp. 83–118.
[41] H. A. Jaeger *et al.*, "Anser EMT: the first open-source electromagnetic tracking platform for image-guided interventions," *Int. J. Comput. Assist. Radiol. Surg.*, vol. 12, no. 6, pp. 1059–1067, Jun. 2017.
[42] D. R. Wulfman, D. J. Foster, M. Hein, K. R. Poppe, and B. H. Stadler, "Modular disc array for minimally invasive medical device," US20170189107A1, 06-Jul-2017.
[43] M. Hein, D. J. Foster, D. R. Wulfman, and B. J. H. Stadler, "Transducer with magnetic nanowire array," US20170188881A1, 06-Jul-2017.
[44] "Fulltext PDF." .
[45] "Fulltext PDF." .
[46] S. E. Jee, P. S. Lee, B.-J. Yoon, S.-H. Jeong, and K.-H. Lee, "Fabrication of Microstructures by Wet Etching of Anodic Aluminum Oxide Substrates," *Chem. Mater.*, vol. 17, no. 16, pp. 4049–4052, Aug. 2005.
[47] J. Krahn, Y. Liu, A. Sadeghi, and C. Menon, "A tailless timing belt climbing platform utilizing dry adhesives with mushroom caps," *Smart Mater. Struct.*, vol. 20, no. 11, p. 115021, Oct. 2011.
[48] P. D. McGary, L. Tan, J. Zou, B. J. H. Stadler, P. R. Downey, and A. B. Flatau, "Magnetic nanowires for acoustic sensors (invited)," *J. Appl. Phys.*, vol. 99, no. 8, p. 08B310, Apr. 2006.
[49] B. Alberts, Ed., *Molecular biology of the cell*, 4th ed. New York: Garland Science, 2002.
[50] A. S. Cubukcu, E. Zernickel, U. Buerklin, and G. A. Urban, "A 2D thermal flow sensor with sub-mW power consumption," *Sens. Actuators Phys.*, vol. 163, no. 2, pp. 449–456, Oct. 2010.
[51] S. Ćerimović, M. Forstner, F. Kohl, A. Talić, and F. Keplinger, "A computer mouse based on highly sensitive micromachined flow sensors," *Procedia Eng.*, vol. 5, pp. 240–243, Jan. 2010.
[52] E. Engelien, O. Ecin, R. Viga, B. J. Hosticka, and A. Grabmaier, "Calibration-Free Volume Flow Measurement Principle Based on Thermal Time-of-Flight (TToF)," *Procedia Eng.*, vol. 25, pp. 765–768, Jan. 2011.

[53] K.-R. Sohn, “Fiber Bragg grating-tuned feedback laser flow sensor system,” *Sens. Actuators Phys.*, vol. 179, pp. 1–4, Jun. 2012.
[54] “A Simple Fiber-Optic Flowmeter Based on Bending Loss - IEEE Journals & Magazine.” [Online]. Available: https://ieeexplore-ieee-org.ezp2.lib.umn.edu/abstract/document/5306468/. [Accessed: 05-Oct-2019].
[55] D. Silvera-Tawil, D. Rye, M. Soleimani, and M. Velonaki, “Electrical Impedance Tomography for Artificial Sensitive Robotic Skin: A Review,” *IEEE Sens. J.*, vol. 15, no. 4, pp. 2001–2016, Apr. 2015.
[56] G. J. M. Krijnen *et al.*, “MEMS based hair flow-sensors as model systems for acoustic perception studies,” *Nanotechnology*, vol. 17, no. 4, pp. S84–S89, Jan. 2006.
[57] N. Svedin, E. Kälvesten, E. Stemme, and G. Stemme, “A lift-force flow sensor designed for acceleration insensitivity,” *Sens. Actuators Phys.*, vol. 68, no. 1, pp. 263–268, Jun. 1998.
[58] R. Smith, D. R. Sparks, D. Riley, and N. Najafi, “A MEMS-Based Coriolis Mass Flow Sensor for Industrial Applications,” *IEEE Trans. Ind. Electron.*, vol. 56, no. 4, pp. 1066–1071, Apr. 2009.
[59] M. Dijkstra, M. J. de Boer, J. W. Berenschot, T. S. J. Lammerink, R. J. Wiegerink, and M. Elwenspoek, “Miniaturized thermal flow sensor with planar-integrated sensor structures on semicircular surface channels,” *Sens. Actuators Phys.*, vol. 143, no. 1, pp. 1–6, May 2008.
[60] F. B. Myers and L. P. Lee, “Innovations in optical microfluidic technologies for point-of-care diagnostics,” *Lab. Chip*, vol. 8, no. 12, pp. 2015–2031, Dec. 2008.
[61] E. S. Cochran, J. F. Lawrence, C. Christensen, and R. S. Jakka, “The Quake-Catcher Network: Citizen Science Expanding Seismic Horizons,” *Seismol. Res. Lett.*, vol. 80, no. 1, pp. 26–30, Jan. 2009.
[62] M. M. Maqableh *et al.*, “CPP GMR Through Nanowires,” *IEEE Trans. Magn.*, vol. 48, no. 5, pp. 1744–1750, May 2012.
[63] R. Schicker and G. Wegener, “Measuring Torque Correctly,” p. 261.
[64] A. S. Morris and R. Langari, *Measurement and instrumentation: theory and application*, Second edition. Amsterdam ; Boston: Elsevier, AP, 2016.
[65] “tn505.pdf.” .
[66] G. Raghunath, A. B. Flatau, A. Purekar, and J.-H. Yoo, “Non-Contact Torque Measurement Using Magnetostrictive Galfenol,” no. 56031, p. V001T04A013, 2013.
[67] J. Yang and I. Suzuki, “both of Saitama-ken; Kazutoshi Inoue,” p. 30.
[68] I. J. Garshelis, “Collarless circularly magnetized torque transducer and method for measuring torque using the same,” US6553847B2, 29-Apr-2003.
[69] I. J. Garshelis and C. R. Conto, “A magnetoelastic torque transducer utilizing a ring divided into two oppositely polarized circumferential regions,” *J. Appl. Phys.*, vol. 79, no. 8, p. 4756, 1996.
[70] G. S. N. Rao, O. F. Caltun, K. H. Rao, P. S. V. Subba Rao, and B. Parvatheeswara Rao, “Improved magnetostrictive properties of Co–Mn ferrites for automobile torque sensor applications,” *J. Magn. Magn. Mater.*, vol. 341, pp. 60–64, Sep. 2013.
[71] G. P. McKnight and G. P. Carman, “Large magnetostriction in Terfenol-D particulate composites with preferred [112] orientation,” in *Smart Structures and Materials 2001: Active Materials: Behavior and Mechanics*, 2001, vol. 4333, pp. 178–183.

[72] P. N. Anantharamaiah and P. A. Joy, “High magnetostriction parameters of sintered and magnetic field annealed Ga-substituted CoFe2O4,” *Mater. Lett.*, vol. 192, pp. 169–172, Apr. 2017.
[73] S. Liang, B. G. Ravi, S. Sampath, and R. J. Gambino, “Atmospheric Plasma Sprayed Cobalt Ferrite Coatings for Magnetostrictive Sensor Applications,” *IEEE Trans. Magn.*, vol. 43, no. 6, pp. 2391–2393, Jun. 2007.
[74] Y. Chen, J. E. Snyder, C. R. Schwichtenberg, K. W. Dennis, R. W. McCallum, and D. C. Jiles, “Metal-bonded Co-ferrite composites for magnetostrictive torque sensor applications,” *IEEE Trans. Magn.*, vol. 35, no. 5, pp. 3652–3654, 1999.
[75] A. E. Clark, M. Wun-Fogle, J. B. Restorff, K. W. Dennis, T. A. Lograsso, and R. W. McCallum, “Temperature dependence of the magnetic anisotropy and magnetostriction of Fe100−xGax (x=8.6, 16.6, 28.5),” *J. Appl. Phys.*, vol. 97, no. 10, p. 10M316, May 2005.
[76] E. C. Estrine, M. Hein, W. P. Robbins, and B. J. H. Stadler, “Composition and crystallinity in electrochemically deposited magnetostrictive galfenol (FeGa),” *J. Appl. Phys.*, vol. 115, no. 17, p. 17A918, May 2014.
[77] Z. Yang, Z. He, D. Li, and C. Rong, “Bias Magnetic Field of Stack Giant Magnetostrictive Actuator: Design, Analysis, and Optimization,” *Advances in Materials Science and Engineering*, 2016. [Online]. Available: https://www.hindawi.com/journals/amse/2016/1704594/. [Accessed: 11-Feb-2018].
[78] G. Raghunath and A. B. Flatau, “Wireless Magneto-Elastic Torque Sensor System,” in *52nd Aerospace Sciences Meeting*, 2014.
[79] Z. Deng and M. J. Dapino, “Magnetic flux biasing of magnetostrictive sensors,” *Smart Mater. Struct.*, vol. 26, no. 5, p. 055027, May 2017.
[80] T. P. Nolan, R. Sinclair, R. Ranjan, and T. Yamashita, “Microstructure and crystallography of textured CoCrTa/Cr recording media,” *Ultramicroscopy*, vol. 47, no. 4, pp. 437–446, Dec. 1992.
[81] P. D. McGary and B. J. H. Stadler, “Electrochemical deposition of Fe1−xGax nanowire arrays,” *J. Appl. Phys.*, vol. 97, no. 10, p. 10R503, May 2005.
[82] K. S. M. Reddy, *Controlled Electrochemical Synthesis Of Giant Magnetostrictive Iron-Gallium Alloy Thin Films And Nanowires*. University of Minnesota, 2012.
[83] N. Lupu, H. Chiriac, and P. Pascariu, “Electrochemical deposition of FeGa/NiFe magnetic multilayered films and nanowire arrays,” *J. Appl. Phys.*, vol. 103, no. 7, p. 07B511, Apr. 2008.
[84] M. Eisenberg, C. W. Tobias, and C. R. Wilke, “Ionic mass transfer and concentration polarization at rotating electrodes,” *J. Electrochem. Soc.*, vol. 101, no. 6, pp. 306–320, 1954.
[85] G. I. Taylor, “Stability of a viscous liquid contained between two rotating cylinders,” *Philos. Trans. R. Soc. Lond. Ser. Contain. Pap. Math. Phys. Character*, vol. 223, pp. 289–343, 1923.
[86] D. R. Gabe and D. J. Robinson, “Mass transfer in a rotating cylinder cell—I. Laminar flow,” *Electrochimica Acta*, vol. 17, no. 6, pp. 1121–1127, 1972.
[87] D. R. Gabe and D. J. Robinson, “Mass transfer in a rotating cylinder cell—II. turbulent flow,” *Electrochimica Acta*, vol. 17, no. 6, pp. 1129–1137, Jun. 1972.
[88] D. R. Gabe, G. D. Wilcox, J. Gonzalez-Garcia, and F. C. Walsh, “The rotating cylinder electrode: its continued development and application,” *J. Appl. Electrochem.*,

vol. 28, no. 8, pp. 759–780, 1998.
[89] C. T. J. Low, C. P. de Leon, and F. C. Walsh, “The Rotating Cylinder Electrode (RCE) and Its Application to the Electrodeposition of Metals,” *ChemInform*, vol. 36, no. 28, Jul. 2005.
[90] F. C. Walsh, G. Kear, A. H. Nahlé, J. A. Wharton, and L. F. Arenas, “The rotating cylinder electrode for studies of corrosion engineering and protection of metals—An illustrated review,” *Corros. Sci.*, vol. 123, pp. 1–20, Jul. 2017.
[91] C. D. Andereck, S. S. Liu, and H. L. Swinney, “Flow regimes in a circular Couette system with independently rotating cylinders,” *J. Fluid Mech.*, vol. 164, no. 1, p. 155, Mar. 1986.
[92] “TAYLOR.” [Online]. Available: http://storm.colorado.edu/TeachingandLearning/Demonstrations/TaylorCouette/Taylorcouette.htm. [Accessed: 10-Oct-2019].
[93] D. R. Gabe, “The rotating cylinder electrode,” *J. Appl. Electrochem.*, vol. 4, no. 2, pp. 91–108, 1974.
[94] “Rotating Electrode Theory,” *Pine Research Instrumentation Store*, 04-Jan-2016. .
[95] D. R. Gabe and F. C. Walsh, “The rotating cylinder electrode: a review of development,” *J. Appl. Electrochem.*, vol. 13, no. 1, pp. 3–21, 1983.
[96] Reddy Sai Madhukar, Park Jung Jin, Na Suok-Min, Maqableh Mazin M., Flatau Alison B., and Stadler Bethanie J. H., “Electrochemical Synthesis of Magnetostrictive Fe–Ga/Cu Multilayered Nanowire Arrays with Tailored Magnetic Response,” *Adv. Funct. Mater.*, vol. 21, no. 24, pp. 4677–4683, Oct. 2011.
[97] E. C. Estrine, W. P. Robbins, M. M. Maqableh, and B. J. H. Stadler, “Electrodeposition and characterization of magnetostrictive galfenol (FeGa) thin films for use in microelectromechanical systems,” *J. Appl. Phys.*, vol. 113, no. 17, p. 17A937, May 2013.
[98] J. M. Gere and B. J. Goodno, *Mechanics of materials*, 7th ed. Toronto, ON ; [Clifton Park, NY]: Cengage Learning, 2009.
[99] “Mohr’s circle - Wikiversity.” [Online]. Available: https://en.wikiversity.org/wiki/Mohr%27s_circle. [Accessed: 10-Nov-2018].
[100] B. Muller, “Characterizing the Quasi-Static and Dynamic Response of a Non-Contact Magneto-Elastic Torque Sensor,” M.S., University of Maryland, College Park, United States -- Maryland, 2017.
[101] D. J. Foster, D. R. Wulfman, M. Hein, and K. R. Poppe, “Coils and coil assemblies that are radio-translucent,” US20170188882A1, 06-Jul-2017.